ARCHIVES OF ACOUSTICS
5, 4, 275-288 (1980)

LOCATION OF THE SOURCES OF VIBROACOUSTIC DISTURBANCES IN CONTINUOUS MECHANICAL OBJECTS IN THE CASE OF A BOTTLING LINE

M. ANDRZEJEWSKI, C. CEMPEL

Institute of Technical Mechanics, Poznań Technical University
(60-965 Poznań, ul. Piotrowo 3)

This paper presents methods of locating sources of vibroacoustic disturbances in continuous mechanical objects. This problem is discussed in the case of the bottling line in a food industry enterprise. As a result of the investigations, the methods of investigation presented were found to be valuable. Their application in minimizing the acoustic activity of individual partial sources is also indicated.

1. Introduction

Location of the noise sources in industrial interiors where individual machines can be regarded as point sources, is not very difficult methodologically, e.g. using the method whereby successive sources are eliminated, or that of coherence analysis [1, 3]. An advantage of the latter method is that it permits assessment of the energy contribution of the individual partial sources to the total noise in the interior, without eliminating them from the technological process. One should also mention a new method of directional location using a detector of noise sources which is based on the directional properties of appropriate microphone transducers.

Location of noise sources becomes more complex when the object under investigation does not satisfy the basic requirements of a point source of sound. Thus the question arises as to when and under what conditions a noise source can be considered to be a point source.

A machine radiating sound into space is recognized as a point source when the following assumptions are met: that the distance r of the observation point is several times longer than the greatest linear dimension, a, of the source ($r \gg a$) and that the radiated wave length λ is also short compared to the obser-

vation distance ($r \gg \lambda$). When for any reason these two conditions are not satisfied, the noise source will be called continuous and the machine a continuous mechano-acoustical object.

There is a whole group of technological units, e.g. production lines in rolling mills, bottling lines in the food industry etc., whose linear dimensions are comparable to the dimensions of the industrial interior. Under such conditions of sound radiation it is difficult to find in the interior such a position for the observation point r that the requirements of a point source of sound can be met. In these cases the noise source should be recognized as continuous. It can be assumed in advance that the methods of location and identification of noise sources in industrial interiors applied to those machines that can be regarded as point sources (lathes, milling machines, compressors and fans etc.) require suitable modification for application to the case of the analysis of a continuous source. This results, among other things, from the fact that elimination of one component element of a discrete source (e.g. in a production line in a rolling mill or a bottling line) automatically causes the others to be eliminated. This makes it impossible to eliminate successive units of such a plant. This is the basic difficulty in the vibroacoustic analysis of continuous mechanical objects.

This paper is devoted to the location of the basic noise sources in continuous mechanical systems in the case of a Pepsi-Cola bottling line [2].

2. Formulation of the problem

Fig. 1 shows a block diagram of the bottling line discussed. It can be seen from Fig. 1 that the basic units of the line are interconnected, forming production line of a number of container conveyors of different design. The question arises as to which elements of the line radiate noise into the environment and what their share is in the total noise. The second aspect of this paper is the definition of the contribution to the total noise in the interior of the conveyors, whether empty or carrying bottles. This is a result of the fact that the admissible noise level is exceeded by 3 to 5 dB(A) along the production line. It should be noted that the noise radiated by the bottling line presented has a random character. It is a combination of continuous and pulsed noise of different origins (mechanical and aerodynamic).

3. Method of investigation and measuring apparatus

In order to carry out the task set the following investigations were performed:

— the development of a simplified acoustic map of the noise hazard zones in the interior housing the line in order to locate the most dangerous

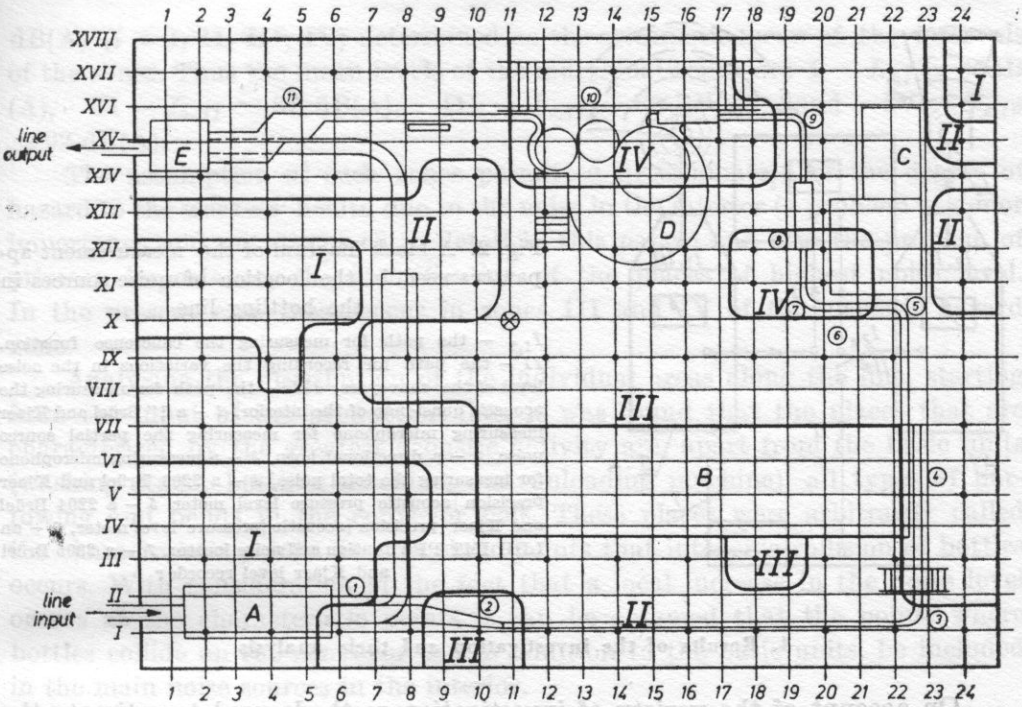

Fig. 1. The block diagram of the position in the interior of the Pepsi-Cola bottling line with the noise hazard zones and the spacing of the points for measuring the partial sources plotted

(I-IV hazard zones)

A **– unloading machine,** ***B*** **– washing stand,** ***C*** **– viewer,** ***D*** **– bottling machine,** ***E*** **– unloading machine for empty bottles; ● – a grid measurement point, ○ – a point for measuring the partial source noise, ⊗ – a point for measuring the total noise L_w = 88 dB (A) ⟨II; III⟩**

points acoustically, and the determination of the mean noise level L_w weighted with respect to the area. This is particularly significant for the selection of the position (zone) for measuring the total noise in the interior as is necessary in the coherence method for the location of noise sources;

– the use of the coherence method for the location of partial noise source in order to determine their energy share in the total noise in the interior;

– the investigation of the acoustic pressure distribution along the conveyor belts only in order to detect those points in the conveyors which are characterized by an increased acoustic activity. This is another way of locating partial noise sources along the conveyor belts.

The whole of the investigations in the present paper were performed using the set of devices shown in Fig. 2. With exception of the vibration and noise locator (a device of the authors' design, which makes it possible to determine the normalised correlation function of two vibroacoustic processes on the basis of sign correlation – a polar correlator), it satisfies the requirements of the Polish Standard PN-64/T-06460.

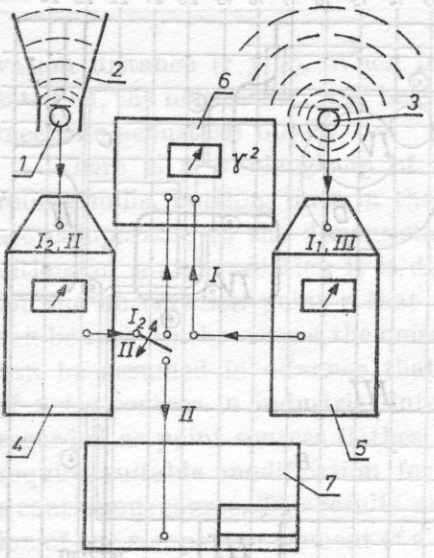

Fig. 2. A block diagram of the measurement apparatus used in the location of noise sources in the bottling line

$I_{1,2}$ – the path for measuring the coherence function, *II* – the path for recording the variations in the noise level of the conveyors, *III* – the path for measuring the acoustic quasi-map of the interior, *1* – a 1" Brüel and Kjaer measuring microphone for measuring the partial source noise, *2* – a directional horn, *3* – a measuring microphone for measuring the total noise, *4* – a 2203 Brüel and Kjaer precision acoustic pressure level meter, *5* – a 2204 Brüel and Kjaer precision acoustic pressure level meter, *6* – an LDH IMT PP vibration and noise locator, *7* – a 2305 Brüel and Kjaer level recorder

4. Results of the investigation and their analysis

On account of the variety of investigation methods used to estimate the vibroacoustical activity of the bottling line the successive stages of the investigation are discussed individually, with an indication of their agreement as to the correct location of the partial sources in the bottling line.

In order to develop a simplified acoustical map (noise hazard zones) of the interior, a 1 m × 1 m grid was superposed on the whole surface area of the interior. The measured quantities were in this case the noise levels measured with respect to the characteristics of the device: the correction characteristic (*A*) and the linear characteristic (Lin). In these measurements the measuring microphone (path III, Fig. 2), was placed at a height of about 1.5m above the floor of the interior. On the basis of the results obtained the following intervals of noise levels in dB (A) were assumed as the limits of the hazard zones:

$$\text{I} - L_I \in \langle 84;\ 86\rangle,$$
$$\text{II} - L_{II} \in \langle 86.5;\ 88\rangle,$$
$$\text{III} - L_{III} \in \langle 88.5;\ 90\rangle,$$
$$\text{IV} - L_{IV} \in \langle 90.5;\ 93\rangle.$$

On the basis of these intervals, the hazard areas corresponding to the individual zones were plotted and the limits of the areas were set using algebraic interpolation (the arithmetic mean) between the noise levels of the neighbouring measurement points. The boundaries of the individual areas and their size are shown in Fig. 1. On account of the large number of measurement points it was assumed that each zone could be represented by the mean level L_{mi} in

dB(A) (i = I, II, III, IV) determined as the arithmetic mean of the intervals of the zones. Thus the mean levels of the individual zones are I – $L_{mI} \cong 85$dB (A), II – $L_{mII} \simeq 87$ dB(A), III – L_{mIII} 89 dB(A) and IV – $L_{mIV} \simeq 92$ dB(A).

The assumption of such zones permitted determination of the degree of hazard to the workers' health due to the noise in the interior (a problem of minor importance and not discussed in detail in this paper) and also the problem of primary importance, the identification of the places of highest noise level. In the present case these occur in zones III and IV of the acoustic hazard zone.

Analyzing the distribution of the individual areas along the line, starting from the input of the production line, it was found that the places that are characterized by the greatest acoustic activity are, apart from the basic units (washing stand, bottling machine, and unloading machine), all types of narrowing and bends in the conveyor belt. These places were arbitrarily called the characteristic points. It is at these points that intensive collision of bottles occurs. With consideration of the fact that a local increase in the noise level occurs at the characteristic points it can be assumed that the points where bottles collide on the conveyor can in addition to the basic units, be included in the main noise sources in the interior.

Although the simplified acoustic map (Fig. 1) permitted separation of the basic noise sources in the bottling line, it gave no information on the energy share of the individual partial sources (the units and characteristic points of the conveyor line) in the total noise in the interior. This is significant, since apart from the significance in terms of the energy of the individual sources, it also gives the ranking of potential measures for minimizing the noise.

The latter end is served by the coherence method of location, which consists in the measurement of the band function of the normal coherence. It is a measure of the similarity of two vibroacoustical processes: the first being the total noise in the interior – path I in Fig. 2, the second being the noise radiated by an elementary source – path II in Fig. 2. It can be used to determine the maximum statistical similarity between the total noise in the interior and the sound disturbances of the individual partial sources in the spectral domain. The present investigation used for this purpose octave bands of the following central frequencies: 100, 250, 500, 1000, 2000, 4000 and 8000 Hz.

Knowing the coherence function of the processes investigated, x and y, in the ith frequency band, similarity or identity can be determined, since:

$\gamma^2_{xy}(f_i) = 1$ if the processes are statistically identical in the band Δf_i;

$0 < \gamma^2_{xy}(f_i) < 1$ if the processes are statistically similar in the band Δf_i;

$\gamma^2_{xy}(f_i) = 0$ if the processes are statistically different in the band Δf_i.

In order to determine the share of the elementary source in the total noise, it is necessary to set a limit, from which the partial source will to a greater or lesser extent affect the overall noise level (total level) in the interior.

From acoustics it is known that when the difference in the noise levels of two sources exceeds 10 dB [2], then the influence on the total noise of the source with a lower sound level can be neglected. Taking this into account, a boundary value (in terms of the sound pressure) can be established, below which the noise from an elementary source will not affect the total noise level 10 dB $\Rightarrow$ 0.316.

Thus the power radiated by a partial source can be neglected if

$$|\gamma_{xy}(f_i)| \leqslant 0.316 \Leftrightarrow \gamma^2_{xy}(f_i) \leqslant 0.1,$$

i.e. 0.1 is the boundary value of the coherence function.

It can be seen from the above remarks that the coherence method for the location of noise sources requires a measurement of the total noise (measurement in a diffuse acoustic field) and a measurement of the sound disturbances from the source itself. The set of necessary apparatus for the task to be carried out is shown in Fig. 2.

The position of the microphone for measuring the total noise level (path I_1 in Fig. 2) was chosen on the basis of the noise hazard zones established. The mean noise level L_w dB(A), weighted with respect to area, was determined for the whole of the interior using the relation

$$L_w = 10 \log \frac{\sum_{i=I}^{IV} S_i I_{mi}}{S_c} \quad [\mathrm{dB(A)}],$$

where S_i is the area corresponding to the ith zone [m^2], I_{mi} is the sound intensity [W/m^2] corresponding to L_{mi} (the mean level of the ith zone),

$$L_{mi} = 10 \log \frac{I_{mi}}{I_0} \quad [\mathrm{dB(A)}],$$

S_c is the total area of the interior [m^2], I_0 is the intensity of reference sound, $I_0 = 10^{-12}\ \mathrm{W \cdot m^{-2}}$.

In the case under investigation, the L_w level was 80 dB(A). Considering further the intervals of noise level for the individual hazard zones, it was found that $L_w \in \langle \mathrm{II\text{-}III} \rangle$ zones.

Accordingly, the microphone for measuring the total noise in the coherence method, was placed at the boundary of zones II and III (Fig. 1). The partial sources in the present method were the basic units of the line and the so called characteristic points (points of narrowing and bends in the conveyor belts etc). Their situation is also shown in Fig. 1.

The values of the function $\gamma^2_{xy}(f_i)$ as a function of the central frequencies of the octave bands are listed in Table 1 and also shown graphically in Fig. 3.

Curves *4* (washing stand) and *10* (bottling machine) show the share of the noise from these units in the total noise. The boundary value assumed for

Table 1. The values of the coherence function $\gamma^2_{xy}(f_i)$ for noise processes in an interior housing the Pepsi-Cola bottling line

Measurement point (Fig. 1)	f_i [Hz]							
	100	250	500	1000	2000	4000	8000	$\gamma^2_{xy}(f)$*
1	0.06	0.04	0.12	0.31	0.18	0.16	0.08	0.14
2	0.08	0.00	0.15	0.42	0.18	0.16	0.07	0.15
3	0.05	0.02	0.15	0.45	0.22	0.11	0.1	0.15
4	0.06	0.03	0.12	0.38	0.20	0.12	0.09	0.14
5	0.08	0.02	0.26	0.45	0.12	0.10	0.04	0.14
6	0.07	0.02	0.15	0.42	0.18	0.09	0.05	0.14
7	0.06	0.01	0.12	0.43	0.16	0.1	0.09	0.14
8	0.05	0.0	0.13	0.35	0.15	0.09	0.1	0.12
9	0.07	0.02	0.12	0.41	0.17	0.11	0.09	0.14
10	0.08	0.0	0.13	0.36	0.15	0.09	0.1	0.13
11	0.06	0.0	0.11	0.29	0.11	0.1	0.08	0.11
$\sum_{i=1}^{11} \gamma^2_{xy}(f_i)$**	0.7	0.16	1.46	4.39	1.82	1.23	0.89	–

* – the mean coherence value of the individual measurement points,
** – the sum of the coherence values in an octave.

$\gamma^2_{xy}(f_i) = 0.1$ is in these cases exceeded in the bands from 500 to 8000 Hz. A comparison of the values of the function $\gamma^2_{xy}(f_i)$ for the two units showed that the share of the bottling machine was slightly lower than that of the washing stand. This means that the noise from the washing stand affects the total noise level to a greater extent than the noise from, for example, the bottling machine. The other plots in Fig. 3 show the share of noise from the individual characteristic points of the conveyors in the total noise in the interior. It can be seen from these plots that those points of the conveyors where intensive collision of bottles occurs (measurement points *2*, *5*, *6*, *7*) contribute most energy to the total noise. The sources described by measurement points *8*, *10* and *11* come next in terms of their energy contribution.

An analysis of the behaviour of the coherence spectra showed that at all the measurement points, a maximum of the function occurs in the octave at 1000 Hz and oscillates around a value of $\gamma^2 = 0.4$. This suggests that all the partial sources established in the simplified acoustic map exert almost equal influence on the total noise level, i.e. they are energetically equivalent. The plot in Fig. 4 confirms the above observations. It can be seen from this figure that the mean value of the coherence of the individual partial sources falls in the interval $0.11 \leqslant \gamma_{xy}(f_i) \leqslant 0.15$, i.e. the values are very close.

In order to gain additional information on the share of the individual octaves in the total noise, it is necessary to analyze the behaviour of the values of $\sum_{i=1}^{11} \gamma^2_{xy}(f_i)$ shown in Table 1. They were obtained by summing the values

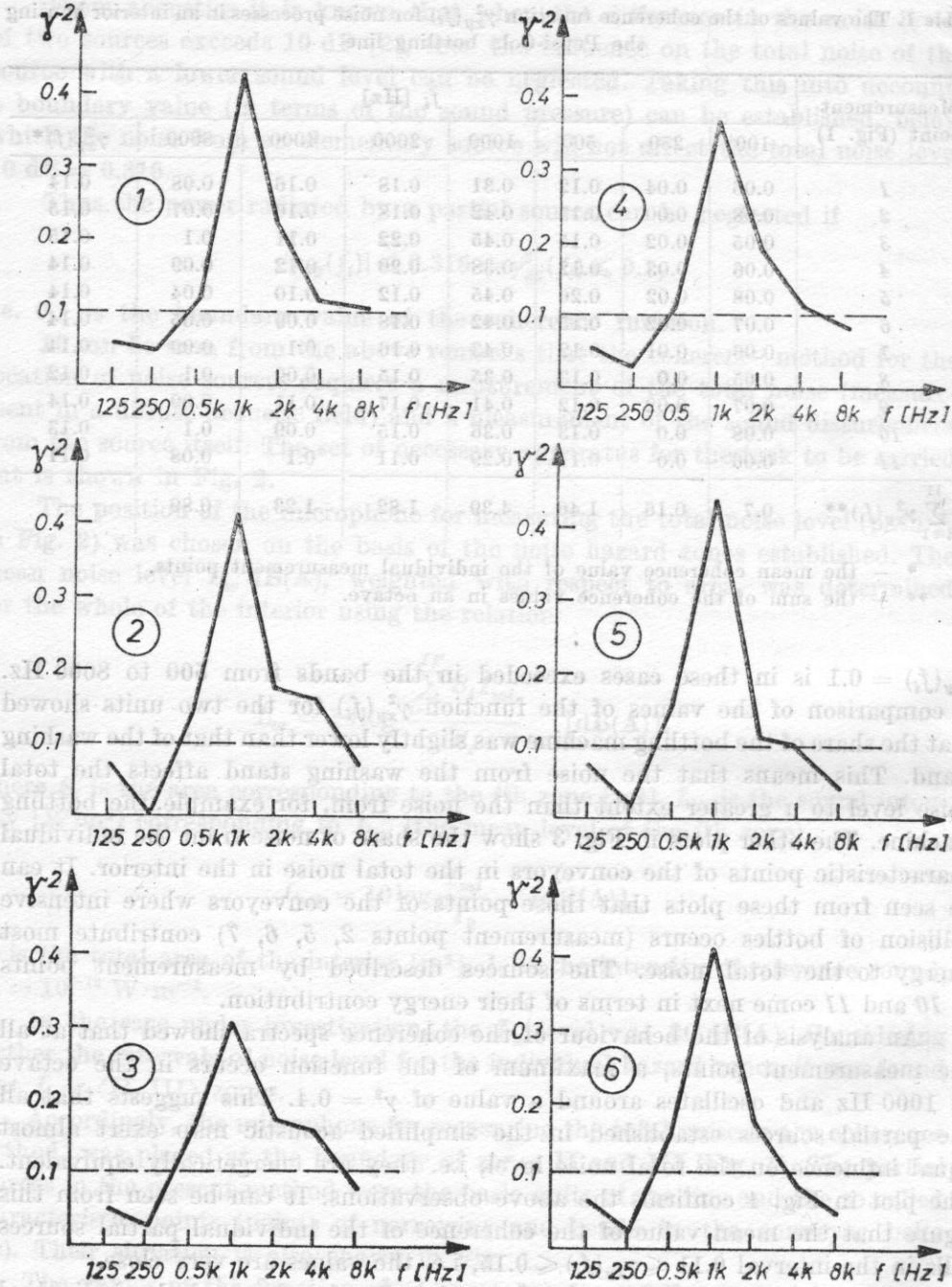
γ²
0.4
0.3
0.2
0.1
1
125 250 0.5k 1k 2k 4k 8k f [Hz]
γ²
0.4
0.3
0.2
0.1
4
125 250 0.5 1k 2k 4k 8k f [Hz]
γ²
0.4
0.3
0.2
0.1
2
125 250 0.5k 1k 2k 4k 8k f [Hz]
γ²
0.4
0.3
0.2
0.1
5
125 250 0.5k 1k 2k 4k 8k f [Hz]
γ²
0.4
0.3
0.2
0.1
3
125 250 0.5k 1k 2k 4k 8k f [Hz]
γ²
0.4
0.3
0.2
0.1
6
125 250 0.5k 1k 2k 4k 8k f [Hz]

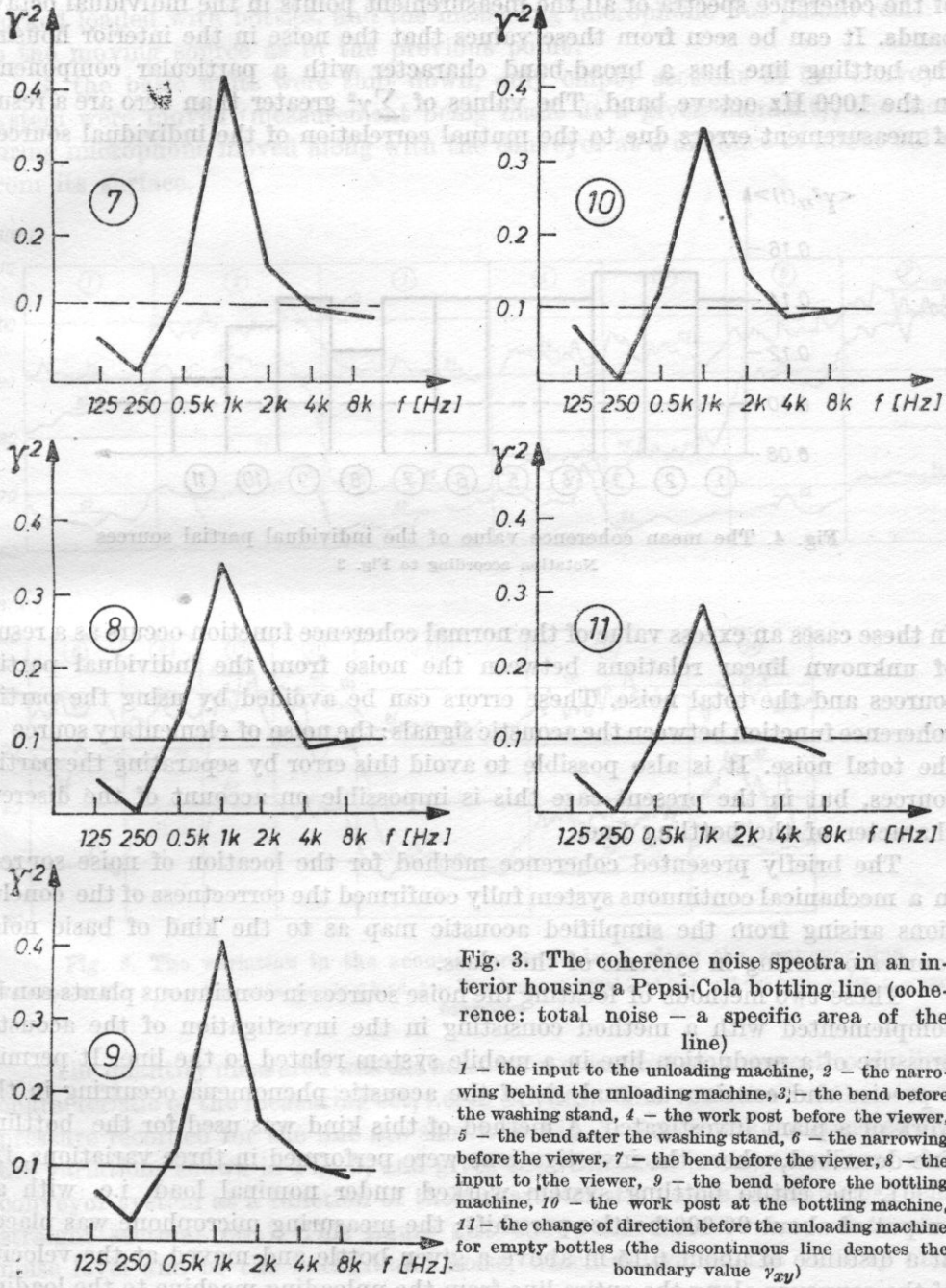

Fig. 3. The coherence noise spectra in an interior housing a Pepsi-Cola bottling line (coherence: total noise – a specific area of the line)

1 – the input to the unloading machine, *2* – the narrowing behind the unloading machine, *3* – the bend before the washing stand, *4* – the work post before the viewer, *5* – the bend after the washing stand, *6* – the narrowing before the viewer, *7* – the bend before the viewer, *8* – the input to the viewer, *9* – the bend before the bottling machine, *10* – the work post at the bottling machine, *11* – the change of direction before the unloading machine for empty bottles (the discontinuous line denotes the boundary value γ_{xy})

of the coherence spectra of all the measurement points in the individual octave bands. It can be seen from these values that the noise in the interior housing the bottling line has a broad-band character with a particular components in the 1000 Hz octave band. The values of $\sum\gamma^2$ greater than zero are a result of measurement errors due to the mutual correlation of the individual sources.

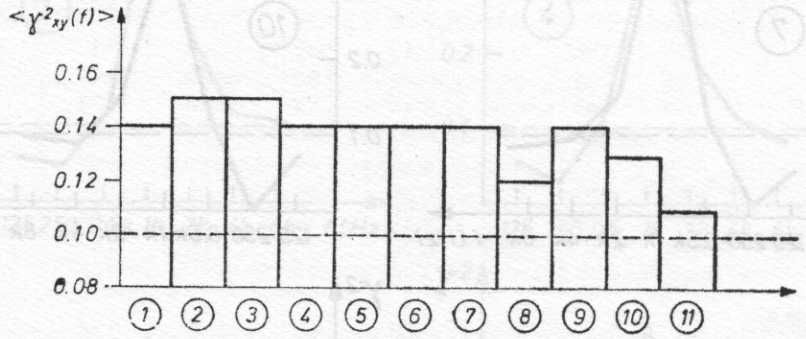

Fig. 4. The mean coherence value of the individual partial sources
Notation according to Fig. 3

In these cases an excess value of the normal coherence function occurs as a result of unknown linear relations between the noise from the individual partial sources and the total noise. These errors can be avoided by using the partial coherence function between the acoustic signals: the noise of elementary source — the total noise. It is also possible to avoid this error by separating the partial sources, but in the present case this is impossible on account of the discrete character of the bottling line.

The briefly presented coherence method for the location of noise sources in a mechanical continuous system fully confirmed the correctness of the conclusions arising from the simplified acoustic map as to the kind of basic noise sources occurring in systems of this class.

These two methods of locating the noise sources in continuous plants can be complemented with a method consisting in the investigation of the acoustic pressure of a production line in a mobile system related to the line. It permits a precise and continuous analysis of the acoustic phenomena occurring in the work of a plant investigated. A method of this kind was used for the bottling line described, where the investigations were performed in three variations, i.e.

1. the entire bottling system worked under nominal load, i.e. with an output of about 90 000 bottles per shift; the measuring microphone was placed at a distance of about 0.15 m above a given bottle and moved at the velocity of the conveyor along the entire line from the unloading machine to the loading machine;

2. the basic units of the line (the unloading machine, the washing stand etc.) were shut down, only individual sections of the conveyor system being

worked loaded with bottles, and the measuring microphone was placed relative to the moving source as in the previous point;

3. the basic units were shut down, only empty sections of the conveyor system were moved (measurement being made at a given moment); the measuring microphone moved along with the conveyor at a distance of about 0.2 m from its surface.

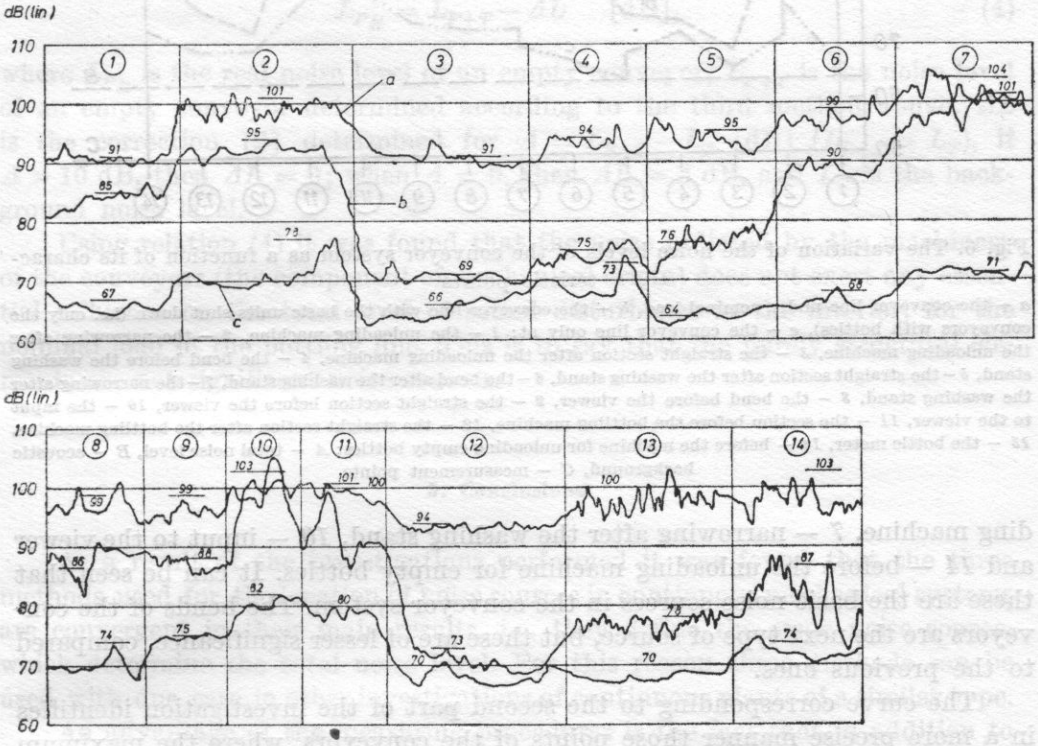

Fig. 5. The variation in the acoustic pressure level along the conveyor line
Notation as Fig. 3; *a* – line under nominal load, *b* – line under nominal load but without basic units, *c* – empty conveyors

The quantity measured was the noise level measured with respect to the linear characteristic of the measuring set, i.e. in dB(Lin). The variations of the acoustic pressure recorded for the line are shown in Fig. 5. Fig. 6 was constructed from the variations shown in Fig. 5, and gives the variations in the noise level of the conveyor system as a function of their characteristic points (narrowings, bends, straight sections etc.). This figure also shows the linear values of the total noise level and of the background noise, which determine the validity of the results obtained.

It can be seen from the behaviour of the curve corresponding to the nominal line load that the highest noise levels occur where intensive collision of bottles takes place. These are the points designated as *2* – narrowing after the unloa-

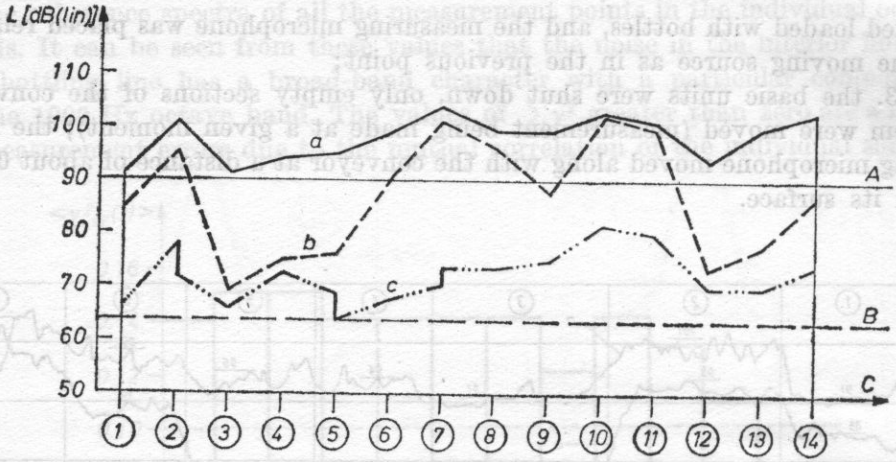

Fig. 6. The variation of the noise levels of the conveyor system as a function of its characteristic points

a – the conveyor line under nominal load, *b* – the conveyor line with the basic units shut down (i.e. only the conveyors with bottles), *c* – the conveyor line only at: *1* – the unloading machine, *2* – the narrowing after the unloading machine, *3* – the straight section after the unloading machine, *4* – the bend before the washing stand, *5* – the straight section after the washing stand, *6* – the bend after the washing stand, *7* – the narrowing after the washing stand, *8* – the bend before the viewer, *9* – the straight section before the viewer, *10* – the input to the viewer, *11* – the section before the bottling machine, *12* – the straight section after the bottling machine, *13* – the bottle meter, *14* – before the machine for unloading empty bottles; *A* – total noise level, *B* – acoustic background, *C* – measurement points

ding machine, *7* – narrowing after the washing stand, *10* – input to the viewer and *14* – before the unloading machine for empty bottles. It can be seen that these are the basic noise sources in the conveyor system. The bends of the conveyors are the next type of source, but these are of lesser significance, compared to the previous ones.

The curve corresponding to the second part of the investigation identifies in a more precise manner those points of the conveyors, where the maximum noise levels occur. These are narrowings (points *2* and *7*), the points where the containers enter the viewer (point *10*), and the section of the curved line together with the bend before the bottling machine. Slight differences in the noise levels at these points were determined for the first and second working variations and they suggest that these points of the conveyors are among the basic noise sources in the interior. The values of these differences show, however, the magnitude of the influence of the basic units on the noise levels at the points of the conveyors under discussion.

The last curve, plotted from the third part of the investigation, shows the variation of the acoustic pressure level along the conveyors when they run idle. An analysis of the behaviour of this curve as a function of the position of the characteristic point of the conveyors, showed that on straight sections the noise level corresponds approximately to the noise level of the acoustic background. An increase in the level of sound disturbances was observed only at

those points of the conveyors where the straining and driving elements are situated. The questions arise as to whether the mechanical noise from an empty conveyor affects the total noise level in the interior and whether an empty conveyor can be regarded as a partial source. In order to answer these questions it is above all necessary to determine the real noise of the empty conveyor. This can be done using relation [2]

$$L_{P_R} = L_{P+T} - \Delta L \quad [\text{dB}], \tag{4}$$

where L_{P_R} is the real noise level of an empty conveyor, L_{P+T} is the noise level of an empty conveyor determined according to the third method above, ΔL is the correction [2] determined for $\Delta = L_{P+T} - L_T$ [dB] ($L_{P+T} > L_T$), if $\Delta > 10$ dB, then $\Delta L = 0$; when $\Delta = 0$, then $\Delta L = 3$ dB, and L_T is the background noise level.

Using relation (4) it was found that the noise radiated by the machinery of the conveyors (the component of mechanical origin) does not exert any essential influence on the total level of sound disturbance in the interior, for the nominal load of the bottling line. This is to say that the purely structural elements are not significant noise sources.

5. Conclusions

As a result of the investigations performed it was found that the three methods used for the location of noise sources in continuous mechanical systems are convergent in their main results, i.e. they define the same noise source, which determine the total noise level. For this reason these methods can be used with due care in other investigations of continuous plants of a similar type.

An advantage of the measuring procedures is the fact that in addition to source location they make it possible to estimate the noise hazard (in terms of a simplified acoustic map of the interior) to the health of the employees, and to determine the energy share (using the coherence method) of the individual partial sources in the total noise. The latter method also makes it possible to choose the optimum way of reducing excess noise.

This investigation also happened to show that the coherence method sometimes gives erroneous results in the energetic quantification of partial noise sources for continuous sources (see Table 1). Despite this, it permits some tentative qualitative and quantitative conclusions to be drawn. Its modification must, however, be proposed or otherwise another method must be developed, which is designed to be applied to a continuous noise source. The acoustic map used in the investigation once more showed its usefulness for noise hazard estimation. Moreover, the investigation of the noise level in a moving line system, which has been used here for the first time, is worth recommending as a method of

locating the areas of high noise level within the continuous source itself. The reliability of this method and also its possible mutations will doubtless be investigated in the future.

References

[1] M. MAJEWSKI, M. ANDRZEJEWSKI, E. WIELOPOLSKA, *The use of the coherence analysis in the investigation of noise sources in industrial interiors*, Wibroakustyka — Odlewnictwo, Nauka, Przemysł, Zeszyt 4, Wyd. Ins. Odlew. Min. Przem. Ciężkiego, IMiWAGH-STOP, Kraków 1976 (in Polish).

[2] C. CEMPEL, *Methods of investigating and minimizing noise and vibrations*, Wyd. Uczel. PP, Zeszyt 502, Poznań 1974 (in Polish).

[3] C. CEMPEL, U. KOSIEL, *Location and identification of noise sources in machines and devices*, Arch. Akust., **11**, 1 (1976) (in Polish).

Received on March 15, 1979; revised version on May 21, 1980.

ARCHIVES OF ACOUSTICS
5, 4, 289-304 (1980)

MECHANICAL-AERODYNAMIC FEEDBACK IN THE PROCESS OF SOUND GENERATION

STEFAN CZARNECKI, MIECZYSŁAW CZECHOWICZ,
TERESA SOBOL

Institute of Fundamental Technological Research, Polish Academy of Sciences
(00-049 Warszawa, ul. Świętokrzyska 21)

For many years phenomena of aerodynamic sound production have been known in the physical aspect, while a mathematical description of it is still insufficient. Therefore, investigations which have the increase of theoretical knowledge of this problem in view, have been performed. These investigations are concerned mainly with the interactions between aerodynamic and acoustic phenomena. However, in some cases of aerodynamic sound production, mechanical vibrations are of importance.

The aim of this work is investigation of the set-up in which mechanical vibrations play an important part in aerodynamic sound production. An attempt is made to explain the mutual aero-vibroacoustic interactions by means of feedback systems. Laboratory tests were carried out in order to perform the preliminary verification.

1. Introduction

Development of aircraft industry caused the main interest in aeroacoustics to be directed recently to the noise generated by supersonic flows. On the other hand, the noise of subsonic flow has been treated as a well-known phenomenon which belongs to the classic science. However, the conditions of sound generation by subsonic flows are known in terms of quality for simple arrangements only. In reality, more complicated systems occur. Therefore, the above problem is again an object of interest as can be seen in works [4] and [5].

Aerodynamic sounds containing the discrete frequencies frequently occur [1, 6, 7]. The systems producing the discrete frequency sounds depend on a good many parameters. The generation of such sounds is often found in fluid flow machines or installations, and it is still an insufficiently examined question.

The aim of this work is investigation of one example of the discrete frequency sound generated aerodynamically, and an analysis of influence of several factors on the generation conditions. It is a continuation of works [2,3].

2. Generation conditions of definite frequency signals

The generation conditions of definite frequency signals may occur in feedback systems. An influence of the output signal with adequate amplitude and phase on the input of the system is characteristic for this kind of systems. A selection of adequate values of amplitude and phase, thus making the generation possible, leads to two basic conditions: phase condition and amplitude condition [8]. Acording to [8]: "phase condition for the oscillator lies in this that a sum of phase shifts in a system is a multiple of the round angle. Since the oscillation frequency is established when the phase condition is satisfied, phase condition can be called the frequency condition. The amplitude condition for the oscillator is a state, in which a loss of energy is less than the energy delivered to the system or equals the delivered energy. The equality occurs when a steady state of oscillations exists".

The edge tone production, described among others by POWELL, is an example of aerodynamically generated sound. Powell explains this phenomenon by means of aeroacoustic feedback as follows: disturbances (vortices) arise, when an air jet ($Re < 3000$) is issuing from a nozzle in the shape of long slit. When an air jet is issuing from a nozzle in the shape of the long slit, disturbances at the nozzle lip are arising and traveling downstream. As a result of the jet hitting the sharp edge downstream from the slit, a sound wave is emitted and propagates also upstream to the nozzle lip. The sound wave, reaching the slit, initiates a new disturbance propagating downstream. Thus, the influence of the acoustic field initiated by the flow again on the flow, makes a feedback loope

This phenomenon may be also explained on the basis of the hydrodynamit theory, where it is assumed that the vortices occurring around the wedge affec. the changes of flow field at the nozzle lip. In more complicated cases, mechanical vibrations of the system accompany the generation of the aerodynamic sound. Thus, the above mentioned amplitude and phase conditions involve additionally the impact of the mechanical system on the aeroacoustic field. It has an effect on the enlargement of the system of feedback loops.

3. Block diagram of the test arrangement

The set-up presented in Fig. 1 was taken into consideration. An air jet issuing from a circular orifice hits a flat bar, whose lower part is inside the acoustic resonator. The discrete frequency sound generated in this set-up has some similar features to the edge tone, but there is also a difference in the range

of velocity ($Re > 30\,000$), as well as in the shape of the nozzle. Moreover, the process of generation is more complicated due to mechanical vibrations of the bar. In order to draw a distinction between the two types of generation, the sound produced in the test arrangement was called the quasi-edge tone. Let us take into consideration the arrangement shown in Fig. 1, but without the acoustic resonator. Since the conditions required for the classical edge tone generation are not satisfied, a broad-band noise without the discrete frequencies is obtained. The amplitude condition is not satisfied due to the weak feedback between acoustic and aerodynamic fields. If the acoustic resonator (in the shape of the cylinder) is present, as shown in Fig. 1, an acoustic wave occurs at the edge of the bar and is reflected by the walls of the resonator. It results in reinforcement of some frequencies corresponding to the resonant frequencies of the resonator. If the walls of the acoustic resonator are rigid, it is a half-wave resonator, which for the basic tone is characterized by an antinode of acoustic velocity. Therefore, the bar is set in motion (transverse vibrations) corresponding to the resonant frequency of the resonator. The vibrations of the bar reinforce the acoustic wave, which then reinforces the intensity of vortices if the phase condition is fulfilled.

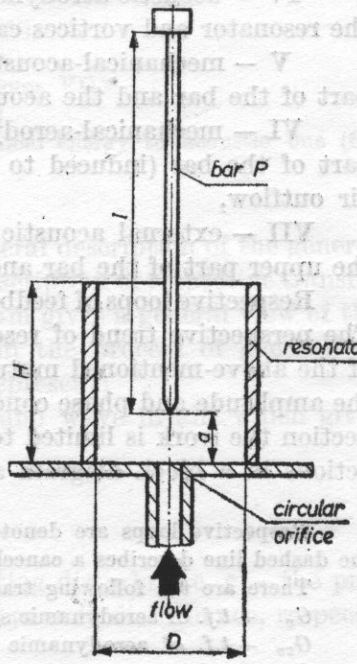

Fig. 1. Diagram of the test arrangement

Futhermore, the resonant phenomena of the vibrations of the bar can play a part in this process. Additional reinforcement of the vibrations of the system appears when the length of the bar is well chosen viz. one of the resonant frequencies of the bar corresponds to the frequency of the signal produced. This

physical process may be described by means of a block diagram, whose elements correspond to the respective physical phenomena. The mutual interactions of aero-vibroacoustic phenomena lead to the feedback system.

There are two following types of feedback loops in the investigated arrangement:

1. Resonant loops, in which the output and input signals are of the same type. The transfer functions of these elements are characterized by a dominant frequency.

2. Non-resonant loops, in which the output and input signals are not of the same type.

The following feedback loops can occur:

resonant loops

I — aerodynamic feedback connected with disturbances of the jet at the outflow from the circular orifice,

II — acoustic feedbackcon nected with proper vibrations of the half-wave acoustic resonator,

III — mechanical feedback connected with transverse vibrations of the bar;

non-resonant loops

IV — acoustic-aerodynamic feedback between the acoustic wave inside the resonator and vortices cast off from the edge of the bar,

V — mechanical-acoustic feedback between the vibrations of the lower part of the bar and the acoustic wave in the resonator,

VI — mechanical-aerodynamic feedback between the vibrations of the lower part of the bar (induced to resonant vibrations) and the disturbances of the air outflow,

VII — external acoustic feedback between the acoustic wave emitted by the upper part of the bar and the acoustic wave inside the resonator.

Respective loops of feedback consist of blocks of adequate transfer functions. The perspective trend of research in this domain is a quantitative description of the above-mentioned mutual interactions, in order to determine analytically the amplitude and phase conditions. At this stage it is too difficult. In this connection the work is limited to the proposal of the formulation of mutual interactions in a block diagram as presented in Fig. 2.

Respective loops are denoted in Fig. 2 by Roman numerals (I-VII). Additionally, the dashed line describes a cancellation loop which is discussed further on.

There are the following transfer functions (*t.f.*) in Fig. 2:

G_v — *t.f.* of aerodynamic system,

G_{vv} — *t.f.* of aerodynamic feedback (loop I),

G_{va} — *t.f.* of system converting from aerodynamic energy to acoustic one,

G_a — *t.f.* of acoustic system (resonator),

G_{aa} — *t.f.* of acoustic feedback (loop II),

G_{md} — *t.f.* of mechanical system (lower part of the bar),

G_{mg} — *t.f.* of mechanical system (upper part of the bar),

G_{mm} — *t.f.* of mechanical feedback (loop III),

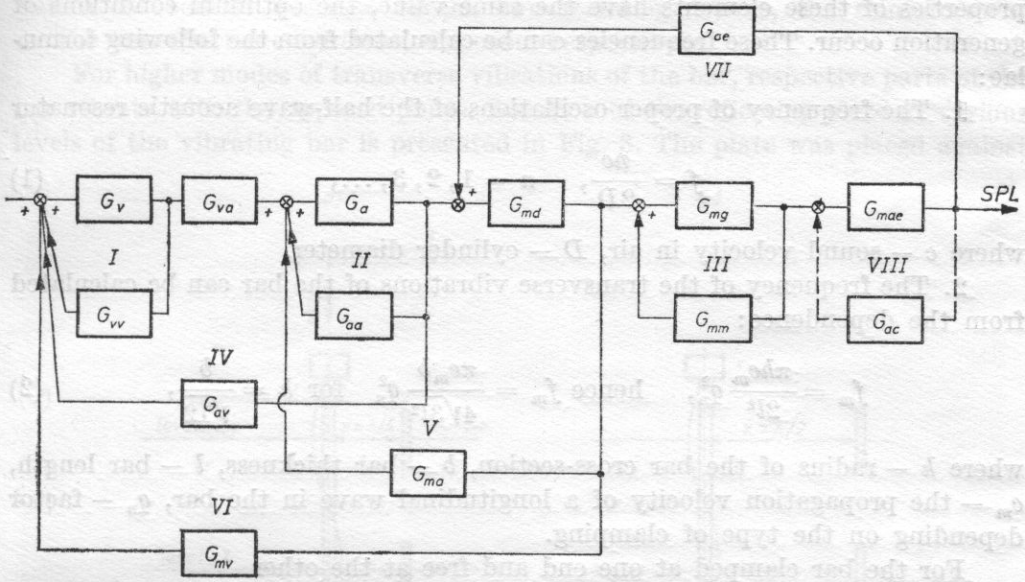

Fig. 2. Block diagram of the arrangement

G_{av} – *t.f.* of acoustic-aerodynamic feedback (loop IV),
G_{ma} – *t.f.* of mechanical-acoustical feedback (loop V),
G_{mv} – *t.f.* of mechanical-aerodynamic feedback (loop VI),
G_{ae} – *t.f.* of external acoustic feedback (loop VII),
G_{mae} – *t.f.* of system converting from the mechanical energy to acoustic one (for upper part of the bar),
G_{ac} – *t.f.* of cancellation system (loop VIII).

This block diagram is a first attempt at a general description of the generation phenomena. At the next stage of research a description of respective transfer functions is provided. Nevertheless, a block diagram gives a general view of the nature of phenomena which may be involved in the process of generation.

The transfer functions shown in Fig. 2 can represent:

1) a delay resulting from propagation of sound wave in air, which gives a phase shift

$$\varphi = \frac{\omega x}{c},$$

where x – the length of the path of the propagating disturbance, c – the propagation velocity of acoustic, mechanical or aerodynamic disturbance, respectively (it is connected with the phase condition);

2) resonant properties of oscillatory elements, which is connected with the amplitude condition.

There are three resonant elements in the test arrangement: the acoustic resonator, the bar and the flow of gas. If the frequencies describing the resonant

properties of these elements have the same value, the optimum conditions of generation occur. These frequencies can be calculated from the following formulae:

1. The frequency of proper oscillations of the half-wave acoustic resonator

$$f = \frac{nc}{2D}, \quad n = 1, 2, 3, \ldots, \tag{1}$$

where c – sound velocity in air, D – cylinder diameter.

2. The frequency of the transverse vibrations of the bar can be calculated from the dependence:

$$f_m = \frac{\pi h c_m}{2l^2} q_n^2, \quad \text{hence } f_m = \frac{\pi c_m b}{4\sqrt{3}l^2} q_n^2 \quad \text{for } h = \frac{b}{\sqrt{12}}, \tag{2}$$

where h – radius of the bar cross-section, b – bar thickness, l – bar length, c_m – the propagation velocity of a longitudinal wave in the bar, q_n – factor depending on the type of clamping.

For the bar clamped at one end and free at the other

$$q_n = \frac{2n-1}{2}, \quad \text{for } n = 1, 2, 3, \ldots$$

3. STROUHAL frequency f_{sh}, which describes the maximum value of noise spectrum arising during a subsonic outflow at the velocity u of an air jet from a circular nozzle of diameter d.

It can be calculated using the formula

$$f_{sh} = \frac{Sh\, u}{d}, \tag{3}$$

where Sh – Strouhal's number.

Influence of the external acoustic field on the generation conditions. It is evident from the analysis of the performance of the test arrangement that the acoustic resonator is of importance in the generation of the quasi-edge tone. We call it a basic resonator and the acoustic field produced by this resonator is called the internal field. As a result of multiple reflections between the walls of the resonator and a vibrating bar, a standing wave occurs. The standing wave causes the reinforcement of vibrations for resonant frequencies of the resonator. In consideration of the strong influence of the acoustic resonator on the generation conditions, the question arises: to what degree the external acoustic field can affect the condition of the resonator performance, i.e. on the process of generation. The external acoustic field can be obtained, if we create a resonator at the upper part of the vibrating bar as a reflecting plate against the bar. The additional standing wave can be created on the various levels of the bar (Fig. 3). According to the phase agreement or disagreement of the instantaneous

values of acoustic pressure of the two standing waves, the reinforcement or the cancellation conditions, can occur respectively.

For higher modes of transverse vibrations of the bar, respective parts of the bar vibrate with the opposed phase. Location of the reflecting plate at various levels of the vibrating bar is presented in Fig. 3. The plate was placed against

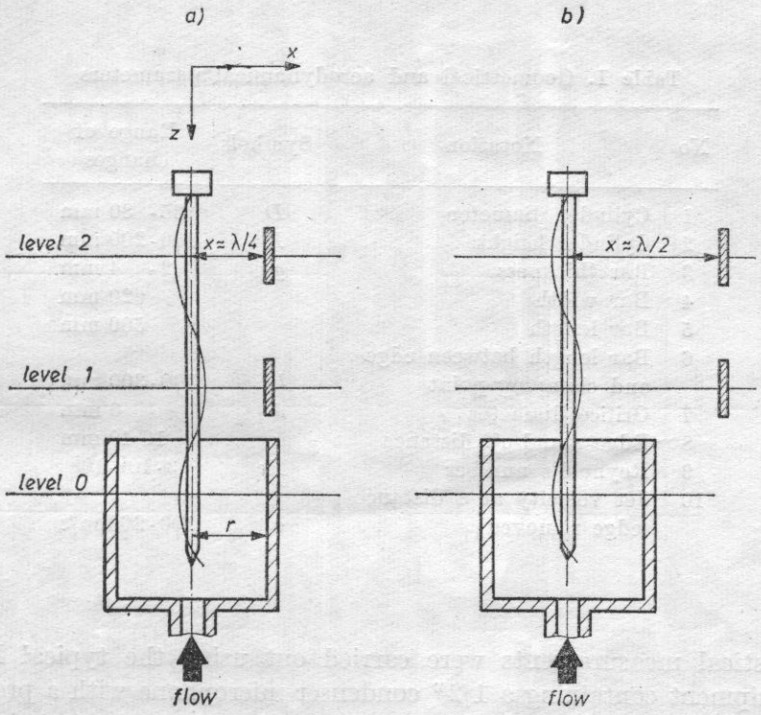

Fig. 3. Arrangement with an external acoustic field

a) cancellation on level 1 and reinforcement on level 2 (for $x = \lambda/4$); b) cancellation on level 1 and reinforcement on level 2 (for $x = \lambda/2$)

both parts of the vibrating bar. Levels 1 and 2 shown in Fig. 3 correspond to two parts of the bar with opposed phases.

On the basis of the theory of image sources [10] it can be proved that the conditions of reinforcement or cancellation for levels 1 and 2 are reversed if the reflecting plate is moved additionally by $\lambda/4$, Fig. 3b. These conditions are presented in the block diagram in Fig. 2 as the eighth feedback loop (VIII).

4. Experiments

The experimental arrangement is shown in Fig. 4. An air jet issuing from the circular orifice hits the sharp edge of the flat aluminium bar placed in the axis of the flow. The distance between the edge and the orifice can be changed stepfree. A cylindrical reflecting surface, resting upon the plate with the outflow

orifice, surrounds the lower part of the bar. The range of dimensions and parameter changes being investigated is presented in Table 1.

The following magnitudes were measured: the sound pressure level, and the spectrum of the generated signal, the mechanical vibrations of the bar, and the stagnation pressure of the flow.

Table 1. Geometrical and aerodynamical parameters

No	Notation	Symbols	Range of changes
1	Cylinder diameter	D	35- 80 mm
2	Cylinder height	H	100-200 mm
3	Bar thickness	g	2- 4 mm
4	Bar width		20 mm
5	Bar length		500 mm
6	Bar length between edge and clamping point	l	100-300 mm
7	Orifice diameter	d	6 mm
8	Edge stand-off distance	a	10-40 mm
9	Reynold's number	Re	$3 \cdot 10^4$-10^5
10	Jet velocity at a distance (edge removed)	u	100-260 m/s

Acoustical measurements were carried out using the typical Brüel and Kjaer equipment containing a 1/2" condenser microphone with a preamplifier, the 2107 analyser and the 2304 level recorder. The set-up was tested in a semi-anechoic room. Acoustic pressure was picked-up by a microphone placed in the free progressive wave in order to avoid interference with a reverberant field.

Mechanical measurements were carried out using a 8307 type Brüel and Kjaer miniature accelerometer. The distributions of acceleration along the bar were measured for different fixing points of the bar. Aerodynamic measurements were carried out using a Pitot tube and a manometer. The stagnation pressure was measured at the jet axis in a jet core and at the distance $a = 30$ mm from the orifice. From these results, the velocity of air jet was calculated.

The following tests were carried out:

a) Dependence of frequency and amplitude of a discrete tone on the parameters of the test system.

b) The distribution of accelerations along the bar and the level of the generated discrete tone for different lengths of the bar.

c) Possibility and conditions of discrete tone cancellation by the acoustic feedback.

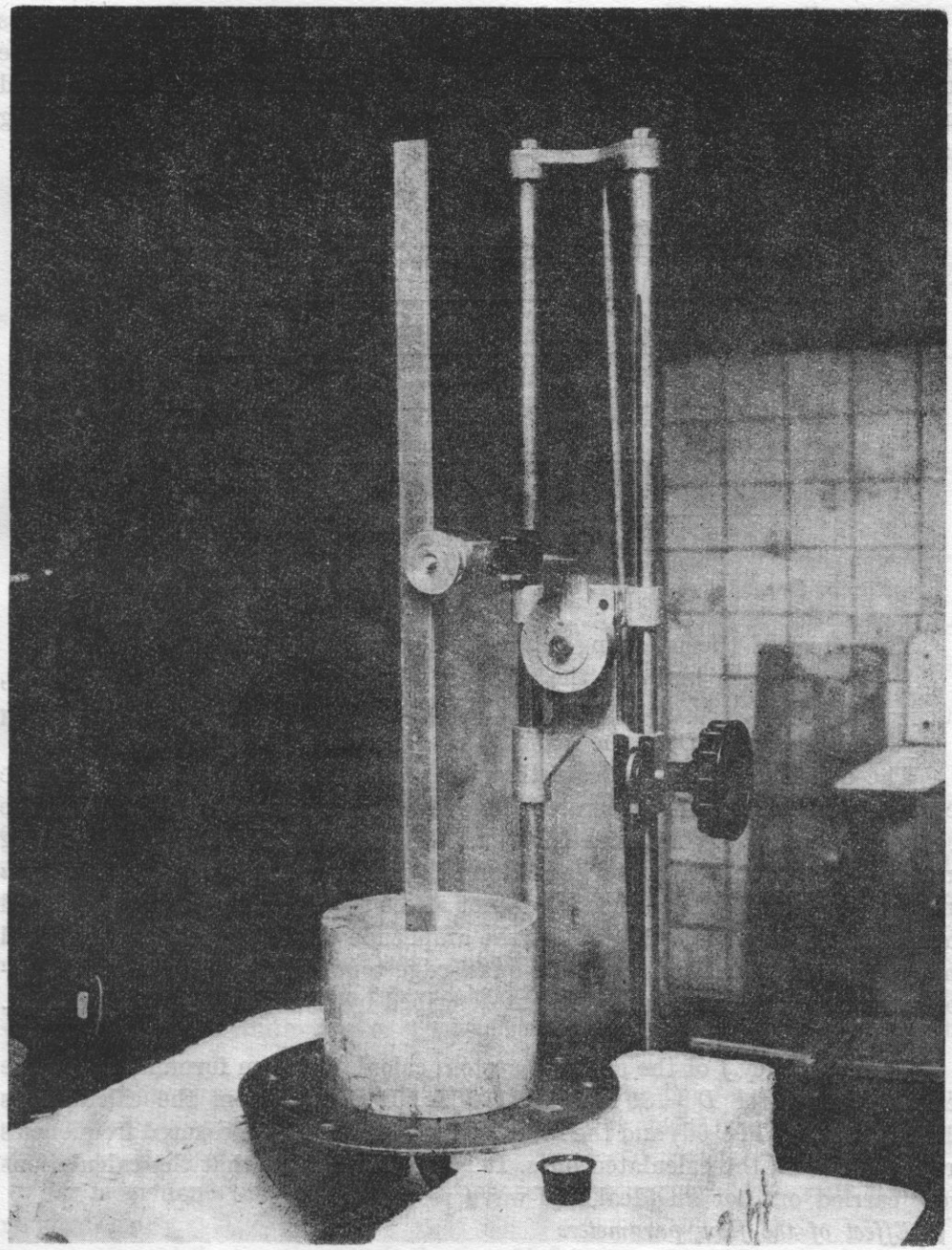

Fig. 4. Test arrangement

5. Results of measurements and calculations

a) Amplitude and frequency of a discrete tone. The results of measurements are presented in Fig. 5 and 6. The spectrum of the investigated quasi-edge tone is shown in Fig. 5 for the jet velocity $u = 220$ m/s. It is evident that a sound pressure level for $f_d = 2500$ Hz (SPL_{2500}) is about 120 dB, and the remaining part of the spectrum is lower by (20-30) dB.

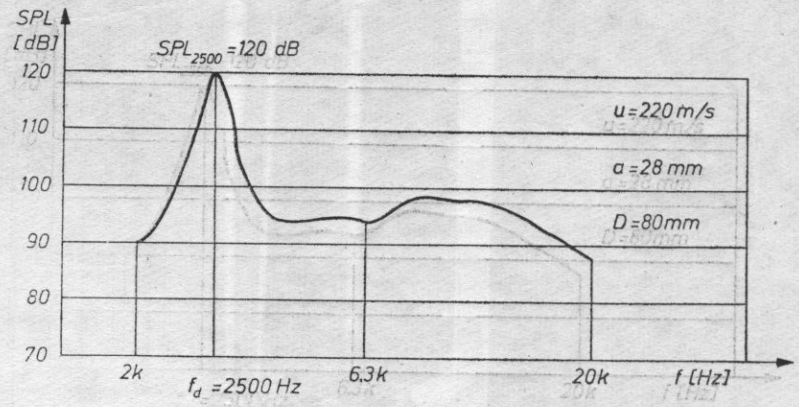

Fig. 5. Dependence of SPL on frequency for quasi-edge tone generation

The effect of the following parameters was tested:

— the distance between the orifice and the edge of the bar (Fig. 6a),

— the velocity u of the air jet (Fig. 6b),

— the diameter D of the acoustic resonator (Fig. 6c, 6d).

The obtained results indicate that the resonant frequency of the acoustic resonator determines the generated dominant frequency. It suggests that the feedback described by transfer functions G_{aa} and G_{ma} (Fig. 2) is very strong and determines the generation conditions. It was found that the jet velocity u and the edge stand-off distance (a) do not affect the frequency of the generated tone (Fig. 6a, 6b), while they affect the amplitude of the signal. It is expected that the greatest amplitudes of the quasi-edge tone should occur when the resonant frequencies of the arrangement described by relations (1)-(3) are similar.

Effect of the cylinder diameter

The frequency f of the acoustic system calculated from formula (1) for the resonator diameter $D = 80$ mm is 2150 Hz. It results from the calculations (dashed curve in Fig. 6d) and the measured results that the measured frequencies are greater than the calculated ones. It is due to the fact that the calculations were carried out for an ideal half-wave resonator.

Effect of the flow parameters

On the basis of analysis of the results shown in Fig. 6 it is evident that for the orifice diameter of 6 mm the best generation conditions occur when the jet velocity u at the edge is 220 m/s.

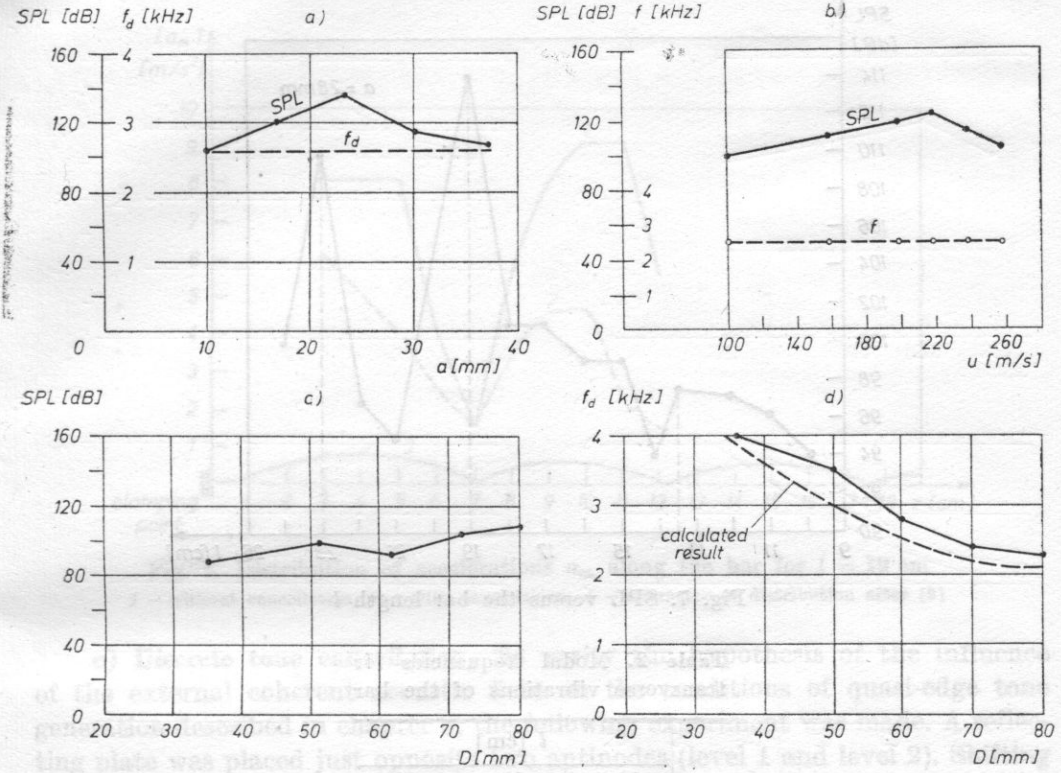

Fig. 6. Variations of SPL and dominant frequency f_d with changes of parameters (a, p_0, D)

b) Distribution of transverse accelerations along the bar. In order to find the influence of vibrations of the bar on the generation conditions, the measurements of SPI_{2500} depending on the length of the bar were carried out. The length of the bar l is the distance between the free end of the bar and the clamping point. The measurement results shown in Fig. 7 prove that the optimum generation conditions arise when l is 19 cm (the best conditions), 23 and 13.5 cm.

In order to calculate the frequency of transvere vibrations of the bar, the velocity of the longitudinal wave c_m was measured. It was found that the velocity $c_m = 5180$ m/s.

Inserting that result into formula (3) for the bar lengths of maximum generation, one can obtain the following values of modal frequencies for transverse vibrations of the bar (Table 2).

It is evident that the value of measured frequency ($f_d = 2500$ Hz) corresponds to:

- the third vibration mode for $l = 13.5$ cm,
- the fourth vibration mode for $l = 19$ cm,
- the fifth vibrations mode for $l = 23$ cm,

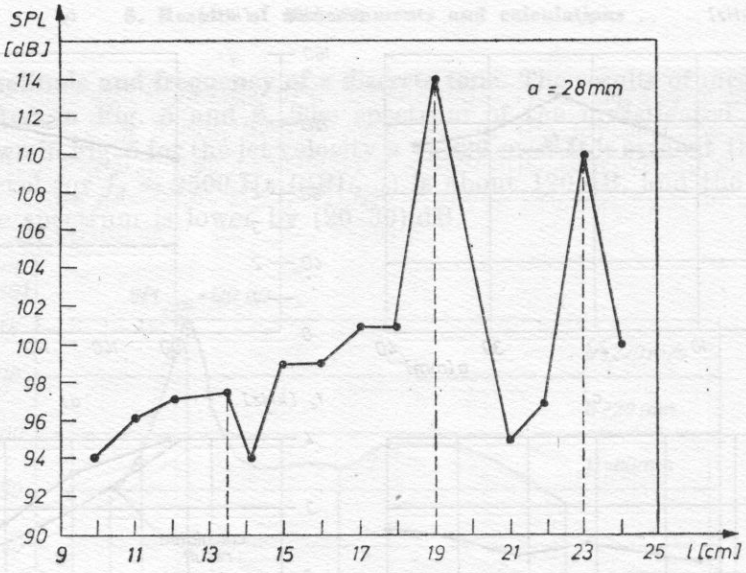

Fig. 7. SPL versus the bar length l

Table 2. Modal frequencies for transverse vibrations of the bar

n	l [cm]		
	13.5 [Hz]	19 [Hz]	23 [Hz]
1	384	194	133
2	865	437	289
3	2403	1213	828
4	4710	2378	1623
5	7791	3934	2684

n — mode number, l — length of the bar

Acceleration was measured for the bar length $l = 19$ cm in order to check agreement with the calculated results. The results shown in Fig. 8 — curve *1*, indicate that the nodes of the standing wave in the bar correspond to distances of 7 and 12 cm from the fixing point, i.e. $0.368l$ and $0.631l$, respectively.

A chart of the vibration distribution for the clamped bars (9) indicates that the nodes of the standing wave for the fourth vibration mode correspond to distances of $0.355l$; $0.644l$; $0.906l$ (Fig. 8 — curve *3*). Thus, these values coincide well with the ones obtained in checking measurements.

The analysis performed proves that the maximum of SPL_{2500} corresponds to the resonant frequencies of the bar, which confirms the assumption that the vibrations of the bar are of substantial importance in the process of quasi-edge tone generation.

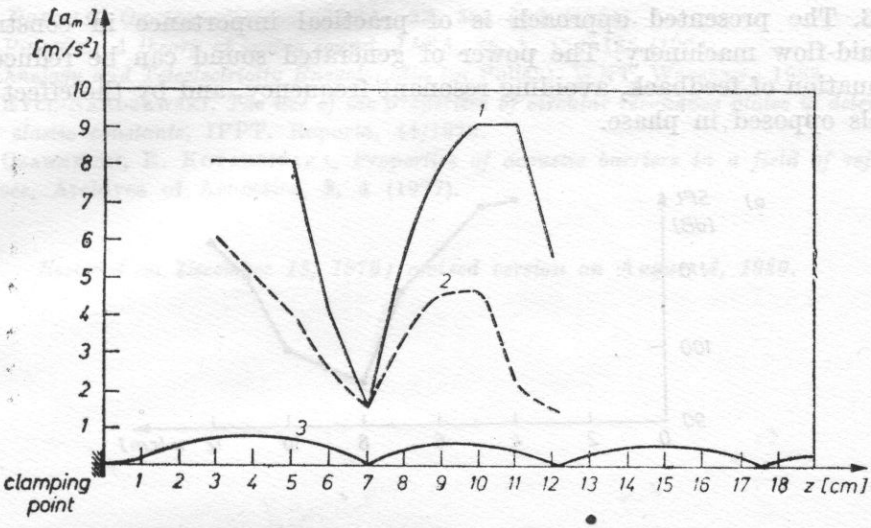

Fig. 8. Distribution of accelerations a_m along the bar for $l = 19$ cm
1 – without cancellation, *2* – with cancellation, *3* – character of distribution after [9]

c) Discrete tone cancellation. To verify the hypothesis of the influence of the external coherent acoustic field on the conditions of quasi-edge tone generation described in chapter 3, the following experiment was made. A reflecting plate was placed just opposite two antinodes (level 1 and level 2). Shifting the plate from and towards the bar caused the change of feedback and therefore the conditions of discrete tone generation.

Measured results of SPL versus the distance x between the reflecting plate and the bar, for levels 1 and 2, are shown in Fig. 9. By approaching the distance $x = (2n-1)\lambda/4$ (at level 1) or $x = n\lambda/2$ (at level 2) the discrete tone was ceasing and the overall SPL was sliding down to its minimum value SPL = 95 dB. Moreover, the increase of SPL is obtained when the plate approaches $x = n\lambda/2$ at level 1, or $x = (2n-1)\lambda/4$ at level 2. This corresponds to the considerations presented in chapter 3. The external coherent acoustic field has much the same influence on the vibration of the bar. The comparison of the vibration distribution without and with feedback due to the plate is shown in Fig. 8. One can see that for a negative feedback (the cancellation) vibration is much smaller (Fig. 8 – curve *2*).

Conclusions concerning discrete tone cancellation

1. A general hypothesis of the feedback between acoustic waves and bar vibration is proper.

2. Insertion of the reflecting plate against the bar enables the cancellation of the quasi-edge tone.

3. The presented approach is of practical importance in construction of fluid-flow machinery. The power of generated sound can be reduced by: attenuation of feedback, avoiding resonant frequency, and by the effect of the signals opposed in phase.

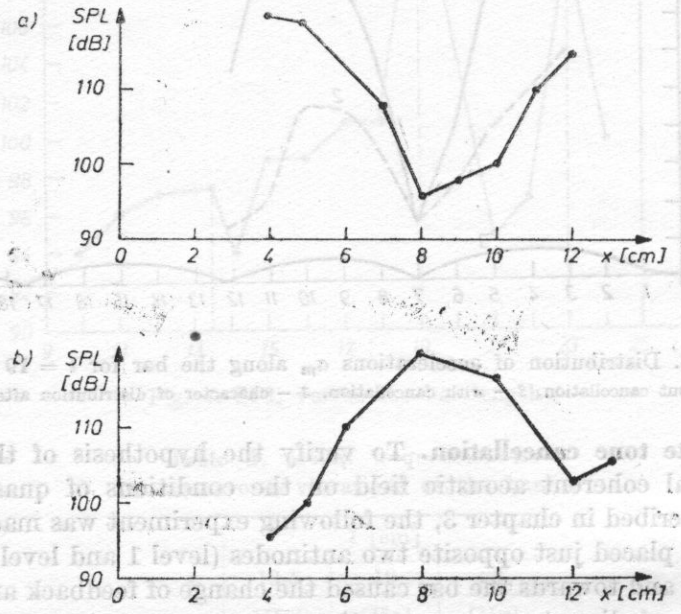

Fig. 9. SPL versus distance x between the plate and the bar
a) plate shifted on level 2, b) plate shifted on level 1

It is assumed that these phenomena are more complicated in reality. This work is only a preliminary attempt at a total description of the feedback between aerodynamic, acoustic and mechanical systems.

The authors wish to thank Professor Wiktor JUNGOWSKI for the valuable discussion and remarks.

References

[1] P. BAADE, *Combustion oscillations in gas-fired appliances*, Conference on Natural-Gas Research and Technology, Atlanta, June 5, 1972.

[2] S. CZARNECKI, M. CZECHOWICZ, T. SOBOL, *Aerovibroacoustic feedback for the edgetone production*, Proc. Inter-Noise 79, Warszawa 1979.

[3] M. CZECHOWICZ, T. SOBOL, S. CZARNECKI, *Acoustic feedback in the process of edgetone generation*, Proc. XXV Open Seminar on Acoustics, Poznań 1978 (in Polish).

[4] M. E. GOLDSTEIN, *Aeroacoustics*, McGraw Hill Inc. USA, 1976.

[5] D. K. HOLGER et al., *Fluid mechanics of the edgetone*, JASA, **62**, 5, 1116-1128 (1977).

[6] A. POWELL, *On the edgetone*, JASA, **33**, 395-409 (1961).
[7] A. POWELL, *A theory of vortex sound*, JASA, **36**, 1, 177-195 (1964).
[8] *Technology and Teleelectricity Encyclopedia* (in Polish), WNT, Warszawa 1968.
[9] J. RYLL-NARDZEWSKI, *The use of the properties of circular resonance plates to determine the elastic constants*, IPPT, Reports, 44/1973.
[10] S. CZARNECKI, E. KOTARBIŃSKA, *Properties of acoustic barriers in a field of reflected waves*, Archives of Acoustics, **2**, 4 (1977).

Received on December 18, 1979; revised version on August 4, 1980.

ARCHIVES OF ACOUSTICS
5, 4, 305-314 (1980)

AN IMPULSIVE SOURCE OF STRONG UNDERWATER ACOUSTIC DISTURBANCES

EUGENIUSZ KOZACZKA

Naval College (81-919 Gdynia)

The present paper discusses the problems connected with the construction of an impulsive high-power electroacoustic transducer. The operating principle of the transducer is the discharge of a capacitors by a thin wire.

The paper also shows the electrical system of the transducer and gives the values of the basic electrical components (parameters) of the circuit.

The transducer generates acoustic disturbances of very short duration, which permits this type of source to be used in studies of sea physics.

The paper presents the results of the investigation of the source itself, performed in an anechoic basin. The maximum level of the acoustic pressure obtained at a voltage $U = 3.8$ kV and a capacitance $C = 450$ μF was 230 dB relative to a pressure of 1 μPa, at a distance of 1 m from the source.

Introduction

Experimental investigations in underwater acoustics require strong sources of acoustic waves. They are particularly necessary in the investigation of sound scattering and absorption, in the measurement of the velocity of sound, and in the investigation of the structure of the sea bottom. They are also used to investigate reverberation and scattering from the rough sea surface.

The classic high — power transducers are severely limited in their use. The maximum efficiency (the maximum level of the acoustic pressure) is limited by overheating, possible electrical breakdown, or by the cavitation threshold. A disadvantage of the magnetostrictive and piezoelectric transducers is that their maximum efficiency can only be obtained at a frequency equal to the frequency of the mechanical resonance, which causes the disturbances radiated by these sources to have almost the character of harmonic waves (in the case of a sharp resonance). These transducers are not very useful for investigations at low frequencies.

Workers very often use strong sources of underwater acoustic disturbances, i.e. underwater detonations of explosives [3, 4, 5, 12]. A disadvantage of these sources is that the repeatability of the sound effects accompanying them is low, for a given mass of detonating explosive, which makes statistical processing of the results difficult. Moreover, this method of investigation is dangerous.

The recent years have seen an increasing use of impulsive sources, driven by a discharge of capacitors [5, 8, 11, 12, 14]. Electrical energy is transformed to acoustical energy, using different physical phenomena. Magnetic short – circuit transducers [8], breakdown (spark) discharges [12] and the so-called exploding wires (discharge by a thin wire) [5, 11] are most often used.

This paper will present the results of investigations performed in an anechoic basin which permitted the acoustic characteristics of an exploding wire to be investigated over a wide range.

2. The short characteristic of the discharge of capacitors by a thin wire placed underwater

The discharge of capacitors by a wire underwater is different in its essential mechanism from the breakdown discharge (sparker). The wire strung between the electrodes prevents the breakdown stage from occurring, and the distance between the electrodes can be longer at the same electrodes voltage.

The use of a bridge between the electrodes essentially decreases the duration of the pulse, which in turn causes an increase in the energy density at discharge, thus making this process more violent, compared to that of a breakdown discharge. The effectiveness of converting electrostatic energy to acoustical energy is several percent higher.

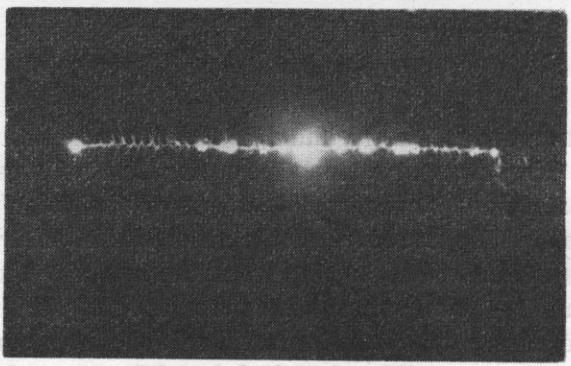

Fig. 1. The process of the discharge of the capacitor by a thin wire underwater

In the case when the circuit of the wire sparker was short circuited a rapid heating of the wire strung between the electrodes initially occurs as a result of the Joule heat. At this stage of the discharge there is still no influence on the magnetic field of the wire through which the electric current is flowing. In the

next stage, the wire melts and turns into a region of ionised gas called the plasma filament. In connection with the plasma filaments, the pinch effect causes narrowing of the discharge channels. Most probably droplets of plasma are formed in these which are the sources of the pressure waves.

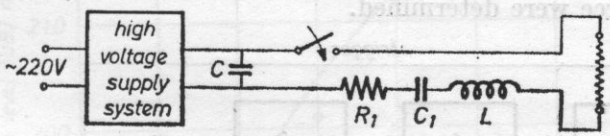

Fig. 2. The electrical system of the transducer and supply circuit

The process of the discharge of capacitors by a thin copper wire is shown in Fig. 1.

3. Design and performance principle of the transducer

The magneto system consists of a battery of capacitors adapted for pulse performance, a connector, supply cables, supply source and transducer. The sparker has two electrodes, between which a thin copper wire is strung. The electrical system of the wire sparker together with the supply circuit are shown in Fig. 2.

The parameters of the supply system and the remaining data are the following: the supply voltage $U = 0\text{-}4$ kV, the capacitance of the capacitors $C = 450$ μF, the capacitance of the circuit $C_1 = 7.3$ μF, the resistance of the circuit $R_1 = 0.09$ Ω, the resistance of the copper wire $R \approx 0.056$ Ω, the inductance of the circuit $L = 10$ μH, the diameter of the copper wire $d = 2 \cdot 10^{-4}$ m.

Fig. 3 shows a block diagram of the measuring system, which consists of the following elements of the measuring chain (all manufactured by Brüel and Kjaer): a 8103 type measuring hydrophone with a transmission band ±2 dB of 0.1 Hz-140 kHz; a 2626 type conditioning amplifier with a transmission band ±2 dB of 0.3 Hz-100 kHz; a 2606 measuring amplifier with a transmission band ±0.5 dB of 2 Hz-200 kHz.

An oscilloscope OG-2-31 RFT with memory with a transmission band of 0-10 MHz was also used. The analogue – digital system used had a transmission band of 0-50 kHz (the sampling rate was 10^5 kp/s).

The signal from the hydrophone (which had a receiving characteristic that was flat to 100 kHz) was, after amplification, supplied to an oscilloscope with a memory. It was also transformed to a digital form and fed to the computer. The power spectrum and the autocorrelation function, were determined using an FFT algorithm.

4. The results of the experimental investigations

Using the system shown in Fig. 2 for the generation of strong transient acoustic disturbances and the system shown in Fig. 3 for recording the waveform and the spectral – correlation analysis, a number of characteristics of the pulse source were determined.

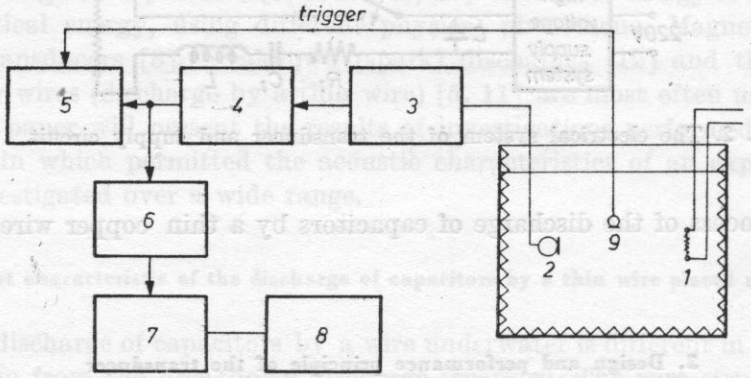

Fig. 3. The diagram of the measuring system

1 – transducer, *2* – a 8103 type Brüel and Kjaer measuring hydrophone, *3* – a 2626 type Brüel and Kjaer conditioning amplifier, *4* – a 2606 type Brüel and Kjaer measuring amplifier, *5* – an oscilloscope OG 2-31 type RFT with memory, *6* – the analogue-digital convertor, *7* – an ODRA-1305 type computer, *8* – an *X/Y*, *9* – a receiving hydrophone

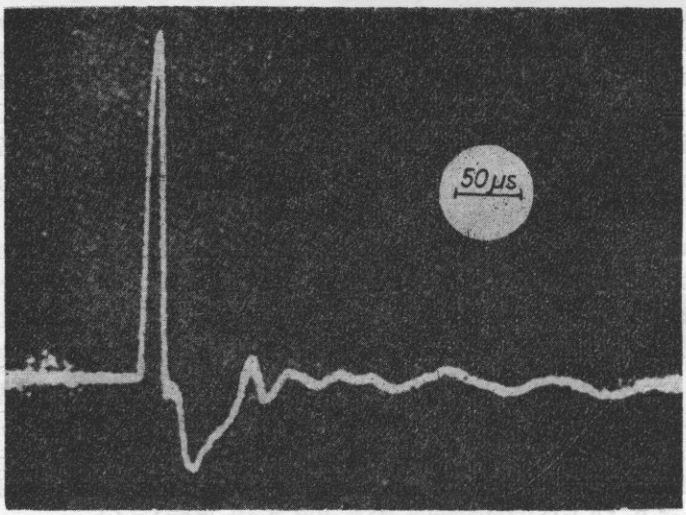

Fig. 4. The pulse shape generated by the exploding wire

The first basic characteristic measured for the source is the pulse shape generated, which is shown in Fig. 4. Fig. 5 shows the dependence of the peak level of the acoustic pressure on the charge voltage of the capacitors.

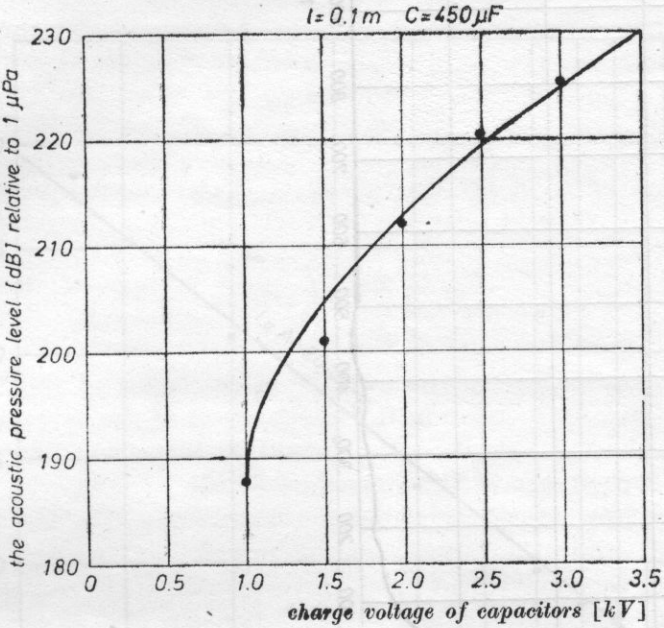

Fig. 5. The dependence of the peak level of the acoustic pressure on voltage

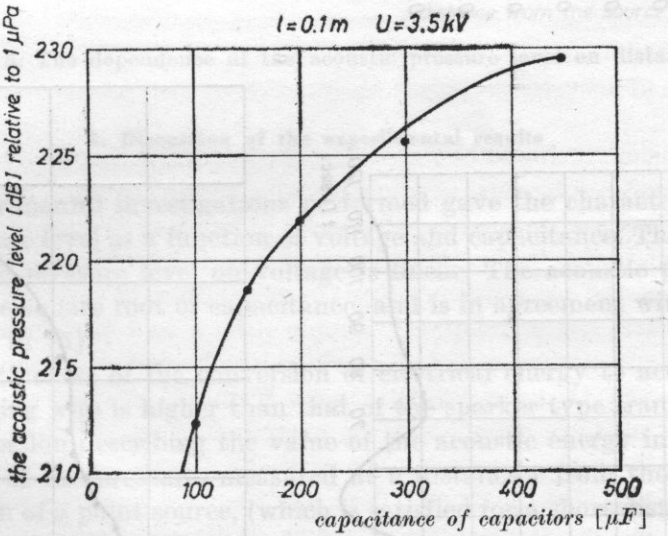

Fig. 6. The dependence of the peak level of the acoustic pressure on capacitance

Fig. 6. shows the dependence of the peak level of the acoustic pressure on the capacitance of the capacitors. Fig. 7 shows the time history of the pulse, the autocorrelation function and the power density spectrum, while Fig. 8 shows the dependence of the acoustic pressure level generated by the wire sparker as a function of the distance from the source.

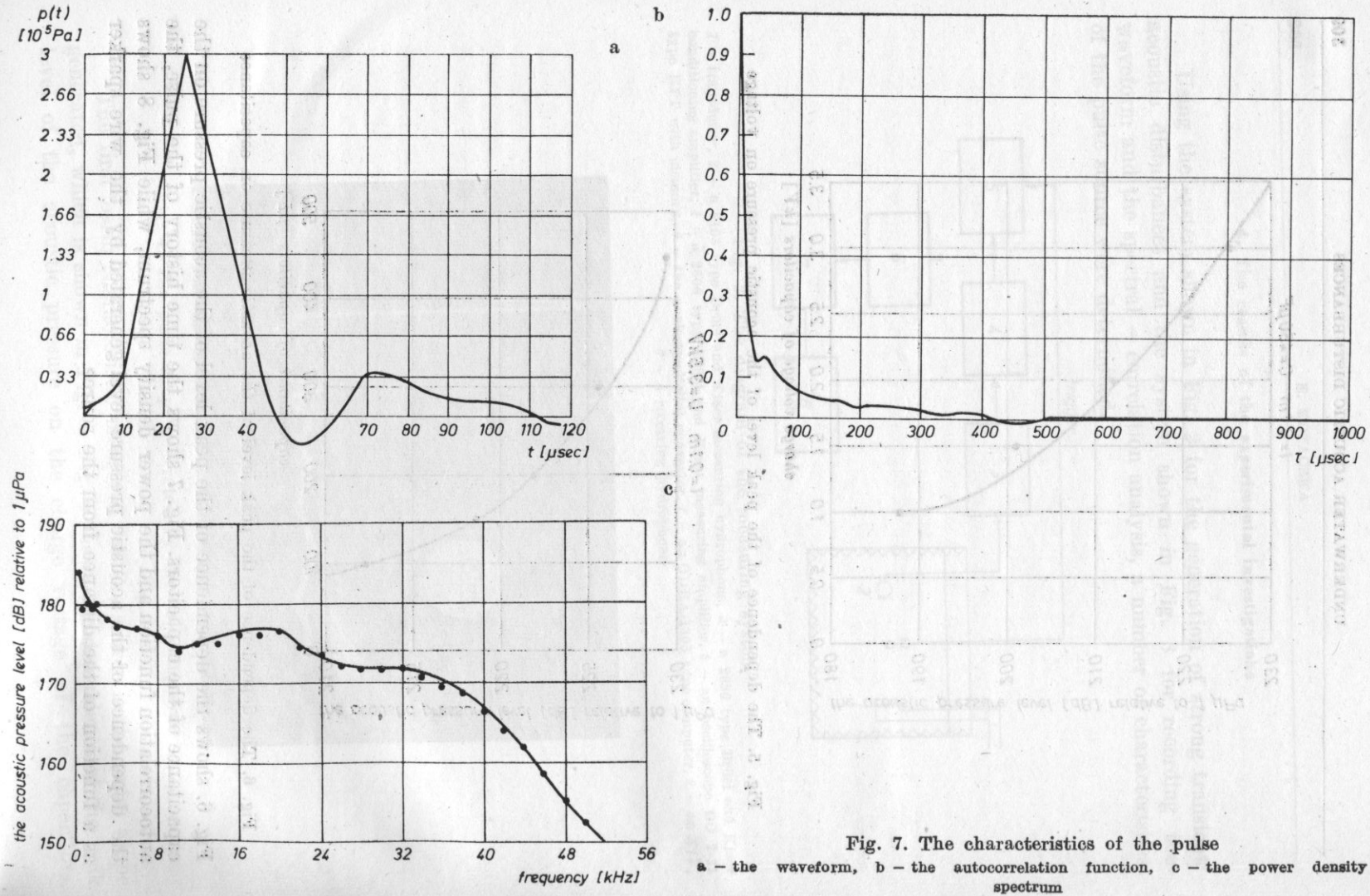

Fig. 7. The characteristics of the pulse
a – the waveform, b – the autocorrelation function, c – the power density spectrum

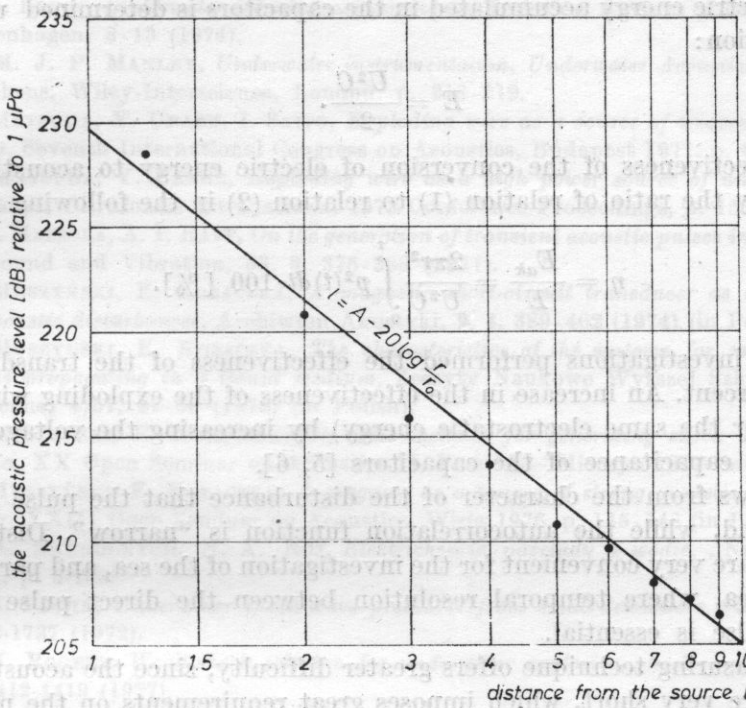

Fig. 8. The dependence of the acoustic pressure level on distance

5. Discussion of the experimental results

The experimental investigations performed gave the characteristics of the acoustic pressure level as a function of voltage and capacitance. The dependence of the acoustic pressure level on voltage is linear. The acoustic pressure level depends on the square root of capacitance, and is in agreement with the dependencies given in [5].

The effectiveness of the conversion of electrical energy to acoustic energy for the exploding wire is higher than that of the sparker type transducer [5, 6].

The expression describing the value of the acoustic energy in terms of the time function of the pressure, measured at a distance r from the source, with the assumption of a point source, (which is satisfied for a short distance between the electrodes) has the following form:

$$E_{ak} = \frac{4\pi r^2}{\varrho c} \int_0^{\tau} p^2(t)\, dt, \tag{1}$$

where E_{ak} is the acoustic energy of the pulse, ϱ is the density of the medium, c is the sound velocity, $p(t)$ is the acoustic pressure, and r is the distance from the receiver to the source.

The electric energy accumulated in the capacitors is determined using the known relation:

$$E = \frac{U^2 C}{2}. \tag{2}$$

The effectiveness of the conversion of electric energy to acoustic energy is defined by the ratio of relation (1) to relation (2) in the following form

$$\eta = \frac{E_{ak}}{E} = \frac{2\pi r^2}{U^2 C} \int_0^{\tau} p^2(t)\,dt \cdot 100 \ [\%]. \tag{3}$$

In the investigations performed the effectiveness of the transducer was about 11 percent. An increase in the effectiveness of the exploding wire can be achieved (for the same electrostatic energy) by increasing the voltage and decreasing the capacitance of the capacitors [5, 6].

It follows from the character of the disturbance that the pulse spectrum is broad-band, while the autocorrelation function is "narrow". Disturbances of this type are very convenient for the investigation of the sea, and particularly, a shallow sea, where temporal resolution between the direct pulse and the reflected pulse is essential.

The measuring technique offers greater difficulty, since the acoustic pulses generated are very short, which imposes great requirements on the measuring apparatus, particularly in terms of the width of the transmission band [9].

The drop of acoustic pressure as a function of distance is greater than 20 dB with a tenfold increase in distance.

In conclusion, it should be noted that the impulsive source of acoustic disturbances described can be used in investigations of the acoustics of the sea. It can also be used in small measuring basins on account of the very short duration of the pulse. It is also interesting to note its possible use in the investigation of the structure of the sea bottom, using the production of a side wave.

The sparker has a relatively simple design and performance principle. The optimum effectiveness of the sparker is achieved with dimensions of the copper wire such that its length ranges from $(5\text{-}10)\cdot 10^{-2}$ m and diameter $(0.2\text{-}0.3)\cdot 10^{-3}$ m. Care should also be exercised to ensure that the resistance at the point where the wire connects with the electrodes should be as low as possible. The shape of electrodes does not play an essential role in terms of its effectiveness, but is essential in terms of the barrier in the propagation path of the acoustic pulse.

References

[1] A. B. Arons, *Underwater explosion shock wave parameters at large distances from the charge*, J. Acoust. Soc. Am. 26, 343-345 (1954).

[2] R. H. Cole, *Underwater explosions*, Princeton University Press, New Jersey, Princeton, 1948, p. 28-45, 114-126.

[3] P. A. LEVIN, *Underwater impulse measurements*, Technical Review, 4, Brüel and Kjaer, Copenhagen, 3-13 (1974).

[4] D. M. J. P. MANLEY, *Underwater instrumentation, Underwater Acoustics*, ed. R. W. B. Stephens, Wiley-Interscience, London, p. 218-219.

[5] M. MATSUDA, Y. URABE, I. SAITO, *Exploding wire as a source of underwater sound impulse*, Seventh International Congress on Acoustics, Budapest 1971, p. 613-616.

[6] M. MATSUDA, Y. URABE, *Exploding wire as a high power source of underwater sound impulses*, Ultrasonics International 1973 Conference Proceedings, p. 155-158.

[7] C. J. MAZZOLA, A. I. RAFF, *On the generation of transient acoustic pulses in water*, Journal of Sound and Vibration, **53**, 3, 375-388 (1977).

[8] A. MUSZYŃSKI, E. KOZACZKA, *A magnetic short-circuit transducer as a strong source of acoustic disturbances*, Archiwum Akustyki, **9**, 4, 389-402 (1974) (in Polish).

[9] A. MUSZYŃSKI, E. KOZACZKA, *The characteristics of the systems for measuring shock waves propagating in a liquid medium*, Zeszyty Naukowe Wyższej Szkoły Marynarki Wojennej 4/51, 47-58 (1976) (in Polish).

[10] A. MUSZYŃSKI, E. KOZACZKA, *On some methods for generating shock waves in liquid media*, XX Open Seminar on Acoustics II, Poznań – Mierzyn 1973 (in Polish).

[11] A. MUSZYŃSKI, E. KOZACZKA, *A magneto as a source of strong acoustic disturbances in water*, XXIII Open Seminar on Acoustics, Wisła 1976, p. 145-146 (in Polish).

[12] K. A. NAUGOLNYCH, N. A. ROJ, *Elektricheskie pazriady w wodie*, „Nauka", Moskwa 1971, p. 3-153.

[13] L. B. POCHE, *Underwater shock-wave pressures from small detonators* , JASA, **51**, 5 (2), 1733-1737 (1972).

[14] P. H. ROGERS, *Weak-shock solution for underwater explosive shock waves*, JASA, **62**, 6, 1412-1419 (1977).

Received on April 30, 1979; revised version on April 21, 1980.

ARCHIVES OF ACOUSTICS
5, 4, 315-336 (1980)

EXPERIMENTAL DETERMINATION AND PRACTICAL APPLICATION OF THE FOUR-POLE PARAMETERS OF STRUCTURE-BORNE SOUND ISOLATORS

G. MELTZER, R. MELZIG-THIEL

Zentralinstitut für Arbeitschutz DDR (8020 Dresden, Gerhart-Hauptmann-Strasse)

Theoretical fundamentals are derived for measuring the four-pole parameters of vibration isolators at real loads. Since the dynamic properties of rubber springs depend on the initial load, the vibration force and velocity are measured on the isolator interfaces for a given initial load. Four-pole parameters are determined for rubber springs and steel springs. The frequency characteristics of the parameters, calculated from the measured results, are compared with the theoretical frequency characteristics. Furthermore, approximate relations for the determination of the four-pole parameters are derived, and verified by experiments. Practical application of the four-pole parameters of vibration isolators is illustrated by examples in which calculations are performed for: structure-borne sound wave isolation by longitudinally vibrating continua and the excitation of structure-borne sound by machines.

Nomenclature*

A — cross-sectional area
$\mathfrak{A}_{11}, \mathfrak{A}_{12}, \mathfrak{A}_{21}, \mathfrak{A}_{22}$ — complex four-pole parameters,
E — elastic modulus,
$\mathfrak{F}$ — complex force,
$\mathfrak{F}_0$ — short-circuit force,
$\mathfrak{F}_1, \mathfrak{F}_1'$ — complex forces at the four-pole input,
$\mathfrak{F}_2, \mathfrak{F}_2'$ — complex forces at the four-pole output,
N — number of isolators,
c_L — propagation speed of longitudinal waves,
f — frequency,
f_0 — natural frequency of the one-mass-system (see Fig. 16),
f_1 — first natural continuum frequency of the isolators,
$\mathfrak{h}$ — complex admittance,
$|\mathfrak{h}|, h$ — modulus of admittance,

* In this article all complex quantities are expressed by Gothic letters.

h_D – floor admittance,
h_F – admittance of the test-foundation,
h_I – admittance of isolators,
h_M – machine admittance,
k – wave propagation number,
l – length of a longitudinally vibrating continuum,
m – mass,
n – continuum compliance; spring elasticity in the frequency range without natural continuum frequencies,
v – complex velocity,
$\tilde{v}$ – rms. value of velocity,
v_D – velocity at the place of machine mounting,
v_F – vertical velocity component at the test-foundation,
v_M – velocity of the machine,
v_1, v_1' – complex velocities at the four-pole input,
v_2, v_2' – complex velocities at the four-pole output,
η – loss factor,
λ – wave length,
ϱ – density,
$\omega = 2\pi f$ – angular frequency.

1. Introduction

Every longitudinally vibrating continuum has natural frequencies which depend on its elastic properties and its mass. With a constant cross-section the frequency f_ν, for example, at which acoustic waves are freely transmitted by a structure-borne sound isolator due to natural resonance can be computed from

$$f_\nu = \nu \cdot \frac{1}{2}\sqrt{\frac{1}{nm}} \qquad (\nu = 1, 2, 3, \ldots). \tag{1}$$

It is well-known that such natural continuum frequencies occur also in the rubber and steel springs which are used for structure-borne sound isolation. Therefore, it does not suffice to know the spring compliance when computing e.g. the structure-borne sound of buildings excited at high frequencies by machines with elastic supports. To be able to compute the vibration transmission or isolation when structure-borne sound isolators are coupled with the other vibrating structures (e.g. machine casing, supporting structure) one must know the frequency-dependent four-pole parameters of the continuum and include them in the computation.

In the following we should like to show how to measure the four-pole parameters of structure-borne sound isolators in the acoustic frequency range for real loads. In addition, the practical application of four-pole parameters of springs is explained when computing both the structure-borne sound isolation of a spring with a head mass, and the structure-borne sound excitation at the place of mounting of elastically supported machines.

2. Computation and measurement of the four-pole parameters of structure-borne sound isolators

2.1. Theoretical frequency response of the four-pole parameters of springs. We proceed from the wave equation for the velocity $v(x)$ of a longitudinal vibrating elastic continuum

$$AE\frac{\partial^2 v}{\partial x^2} - \varrho A\frac{\partial^2 v}{\partial t^2} = 0. \tag{2}$$

The connection between the force $F(x,t)$ and the velocity $v(x,t)$ is as follows

$$\frac{\partial F}{\partial t} = -AE\frac{\partial v}{\partial x}. \tag{3}$$

Solving (2) for the case of harmonic excitation, we get the general solution

$$v(x) - C_1\cos hjk(l-x) + C_2\sin hjk(l-x). \tag{4}$$

Considering the boundary conditions and notation according to Fig. 1 we obtain the following four-pole equations which connect the complex input quantities $\mathfrak{F}(0)$, $\mathfrak{v}(0)$ and the output quantities $\mathfrak{F}(l)$, $\mathfrak{v}(l)$:

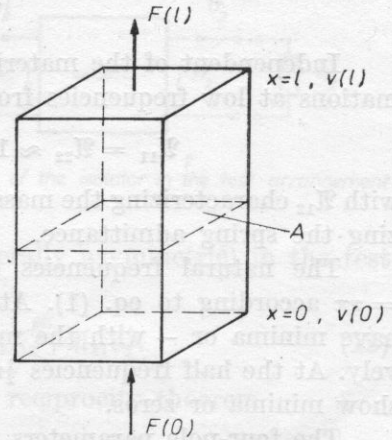

Fig. 1. Derivation of the four-pole parameters of a longitudinally vibrating continuum.

$$\begin{aligned}\mathfrak{F}(0) &= \cos hjkl\cdot\mathfrak{F}(l) + \frac{AEk}{\omega}\sin hjkl\cdot\mathfrak{v}(l),\\ \mathfrak{v}(0) &= \frac{\omega}{AEk}\sin hjkl\cdot\mathfrak{F}(l) + \cos hjkl\cdot\mathfrak{v}(l).\end{aligned} \tag{5}$$

We adopted the form of the four-pole equations with the coefficients $\mathfrak{A}_{ik}$ of the chain matrix which are used in references [2, 5, 6] and [7] and others

to characterize the vibration isolators:

$$\mathfrak{F}(0) = \mathfrak{A}_{11}\mathfrak{F}(l) + \mathfrak{A}_{12}\mathfrak{v}(l), \quad \mathfrak{v}(0) = \mathfrak{A}_{21}\mathfrak{F}(l) + \mathfrak{A}_{22}\mathfrak{v}(l). \tag{6}$$

According to [1] the material damping can be described approximately by a complex wave propagation number

$$\mathfrak{k} = \frac{\omega}{C_L}\left(1 - j\frac{\eta}{2}\right) = k_0\left(1 - j\frac{\eta}{2}\right). \tag{7}$$

The four-pole equations (5) now take the following form:

$$\begin{vmatrix} \mathfrak{F}(0) \\ \mathfrak{v}(0) \end{vmatrix} = \begin{vmatrix} \cos h\left(\frac{\eta}{2} + j\right) k_0 l & \frac{AE_0k_0}{\omega}\left(1 + j\frac{\eta}{2}\right)\sin h\left(\frac{\eta}{2} + j\right)k_0 l \\ \frac{\omega}{AE_0k_0}\left(1 - j\frac{\eta}{2}\right)\sin h\left(\frac{\eta}{2} + j\right)k_0 l & \cos h\left(\frac{\eta}{2} + j\right)k_0 l \end{vmatrix} \begin{vmatrix} \mathfrak{F}(l) \\ \mathfrak{v}(l) \end{vmatrix}. \tag{8}$$

When the damping is very small ($\eta \approx 0$) then the four-pole matrix becomes:

$$(A) = \begin{pmatrix} \cos k_0 l & j\omega m \frac{\sin k_0 l}{k_0 l} \\ j\omega n \frac{\sin k_0 l}{k_0 l} & \cos k_0 l \end{pmatrix}. \tag{9}$$

Independent of the material damping, one obtains the following approximations at low frequencies from equation (8):

$$\mathfrak{A}_{11} = \mathfrak{A}_{22} \approx 1, \quad \mathfrak{A}_{12} \approx j\omega m, \quad \mathfrak{A}_{21} \approx j\omega n, \tag{10}$$

with $\mathfrak{A}_{12}$ characterizing the mass impedance of the continuum and $\mathfrak{A}_{21}$ characterizing the spring admittance.

The natural frequencies of longitudinal vibrating continua are at $k_0 l = \nu\pi$ according to eq. (1). At these frequencies the parameters $\mathfrak{A}_{12}$ and $\mathfrak{A}_{21}$ have minima or – with the material damping disappearing – zeros, respectively. At the half frequencies $\frac{1}{2}\nu f_\nu$ (i.e. $k_0 l = \nu \cdot \pi/2$) the parameters $\mathfrak{A}_{11}$ and $\mathfrak{A}_{22}$ show minima or zeros.

The four-pole parameters were determined for springs with different material damping. The frequency characteristics are plotted in Fig. 6 to 12 for comparison with the measured results and discussed in section 2.4.

2.2. Fundamentals for the measurement of the four-pole parameters of springs. Several proposals for the measurement of the four-pole parameters of vibration isolators have already been described [6-9].

The disadvantage of these methods, however, is that the four-pole parameters of the springs cannot be determined under a real load. For example, the method described in [6, 8] requires two measurements (with the static

load of the spring ≈ 0 N or < 200 N). Thus it is not possible to carry out an exact determination of the load-dependent vibration characteristics, in particular, of rubber springs.

We therefore developed a measuring method permitting measurement of the four-pole parameters of vibration isolators at static loads which correspond to practical cases of isolators. These parameters will be different for different static loads applied in the experiment. This method is necessarily more complicated than the methods described in [6-9] and those used for determining the four-pole parameters of networks in electrical engineering, because the "no-load" case (i.e. when static load is equal to zero) will not be used in the measurements.

In the initial state of the four-pole which is to be measured, the following relations for the input and output quantities will be valid (see Fig. 2):

$$\mathfrak{F}_1 = \mathfrak{A}_{11}\mathfrak{F}_2 + \mathfrak{A}_{12}\mathfrak{v}_2, \quad \mathfrak{v}_1 = \mathfrak{A}_{21}\mathfrak{F}_2 + \mathfrak{A}_{22}\mathfrak{v}_2. \tag{11}$$

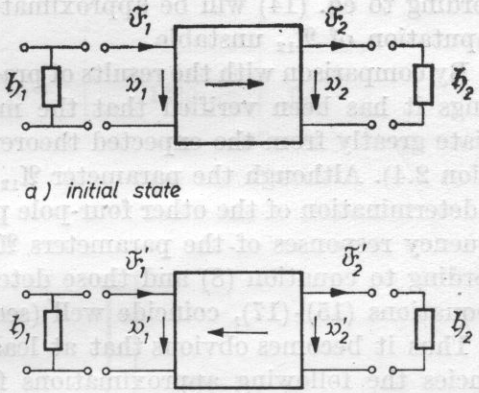

Fig. 2. Derivation of the measuring method for the determination of four-pole parameters of vibration isolators

After reversal of the isolator (which is generally asymmetric) in the test arrangement we obtain

$$\mathfrak{F}_1' = \mathfrak{A}_{22}\mathfrak{F}_2' + \mathfrak{A}_{12}\mathfrak{v}_2', \quad \mathfrak{v}_1' = \mathfrak{A}_{21}\mathfrak{F}_2' + \mathfrak{A}_{11}\mathfrak{v}_2'. \tag{12}$$

We took into consideration that due to the reciprocity theorem

$$\mathfrak{A}_{11}\mathfrak{A}_{22} - \mathfrak{A}_{12}\mathfrak{A}_{21} = 1. \tag{13}$$

The relationships for the determination of the chain matrix parameters follow from equations (11)-(13):

$$\mathfrak{A}_{12} = \frac{\dfrac{\mathfrak{F}_1'}{\mathfrak{F}_2'} - \dfrac{\mathfrak{F}_2}{\mathfrak{F}_1}}{\dfrac{\mathfrak{v}_1}{\mathfrak{F}_1} + \dfrac{\mathfrak{v}_2'}{\mathfrak{F}_2'}} \tag{14}$$

$$\mathfrak{A}_{22} = \frac{\mathfrak{F}_2}{\mathfrak{F}_1} + \frac{\mathfrak{v}_1}{\mathfrak{F}_1}\,\mathfrak{A}_{12}, \tag{15}$$

$$\mathfrak{A}_{11} = \frac{\mathfrak{F}_1}{\mathfrak{F}_2} - \frac{\mathfrak{v}_2}{\mathfrak{F}_2}\,\mathfrak{A}_{12}, \tag{16}$$

$$\mathfrak{A}_{21} = \frac{\mathfrak{v}_1}{\mathfrak{F}_2} - \frac{\mathfrak{v}_2}{\mathfrak{F}_2}\,\mathfrak{A}_{22}. \tag{17}$$

If a vibration isolator behaves approximately like an ideal spring in a given frequency range (i.e. no natural continuum frequencies occur), then the input and output forces are nearly equal: $\mathfrak{F}_1 \approx \mathfrak{F}_2$. In addition $\mathfrak{F}_1 = \mathfrak{F}_1'$ and $\mathfrak{F}_2 = \mathfrak{F}_2'$ is valid for symmetric isolators. Thus it follows that outside the natural continuum frequencies the numbers in the numerator of the expression for $\mathfrak{A}_{12}$ according to eq. (14) will be approximately equal, which makes the numerical computation of $\mathfrak{A}_{12}$ unstable.

By comparison with the results of practical investigations of steel and rubber springs it has been verified that the measured results of the parameter $\mathfrak{A}_{12}$ deviate greatly from the expected theoretical frequency characteristic (see also section 2.4). Although the parameter $\mathfrak{A}_{12}$ is included in equations (15)-(17) for the determination of the other four-pole parameters, it has been shown that the frequency responses of the parameters $\mathfrak{A}_{11}$, $\mathfrak{A}_{22}$ and $\mathfrak{A}_{21}$ which were computed according to equation (8) and those determined from measurements according to equations (15)-(17), coincide well (section 2.4).

Thus it becomes obvious that at least outside the natural continuum frequencies the following approximations for symmetrical springs are possible:

$$\mathfrak{A}_{11} = \frac{\mathfrak{F}_1}{\mathfrak{F}_2} = \mathfrak{A}_{22}, \tag{18}$$

$$\mathfrak{A}_{21} = \frac{\mathfrak{v}_1}{\mathfrak{F}_2} - \frac{\mathfrak{v}_2}{\mathfrak{F}_2}\,\frac{\mathfrak{F}_1}{\mathfrak{F}_2}. \tag{19}$$

The justification of relationships (18) and (19) is discussed in section 2.4.

2.3. Measurement of the four-pole parameters of different springs. The test objects for the measurement of the four-pole parameters are summarised in Table 1.

Figures 3 and 4 show the test arrangement. An electrodynamic exciter serves as a vibration source. The static load was measured with the help of a KWH 200 type semiconducting force transducer (manufacturer: VEB Robotron Messelektronik Dresden). To measure the exciting forces and velocities according to Fig. 3, we used quartz load-cells and piezoelectric pick-ups. The mechanical measuring chain was installed in a sectional steel frame so as to apply any static load up to 1 kN with the help of a regulating screw.

Table 1. Test objects for the determination of the four-pole parameters

Spring type	Mass [kg]	Compliance [$s^2 \cdot kg^{-1}$]	First natural continuum frequency computed from eq. (1) [Hz]	Loss factor
Steel spring (No. 25 spring from P50/125 Type Vibration Isolator of VEB Schwingungsisolatorenbau Radebeul)	0.08	$7.1 \cdot 10^{-5}$	210	10^{-4}
Prismatic rubber spring ($27 \times 27 \times 63$ mm^3)	0.560	$3 \cdot 10^{-6}$	1220	0.1

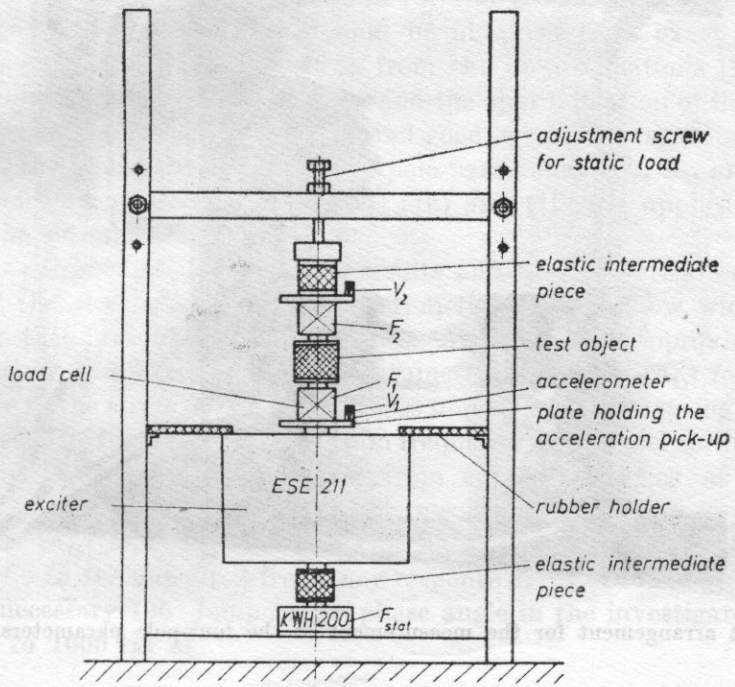

Fig. 3. Test arrangement for the determination of the four-pole parameters of vibration isolators

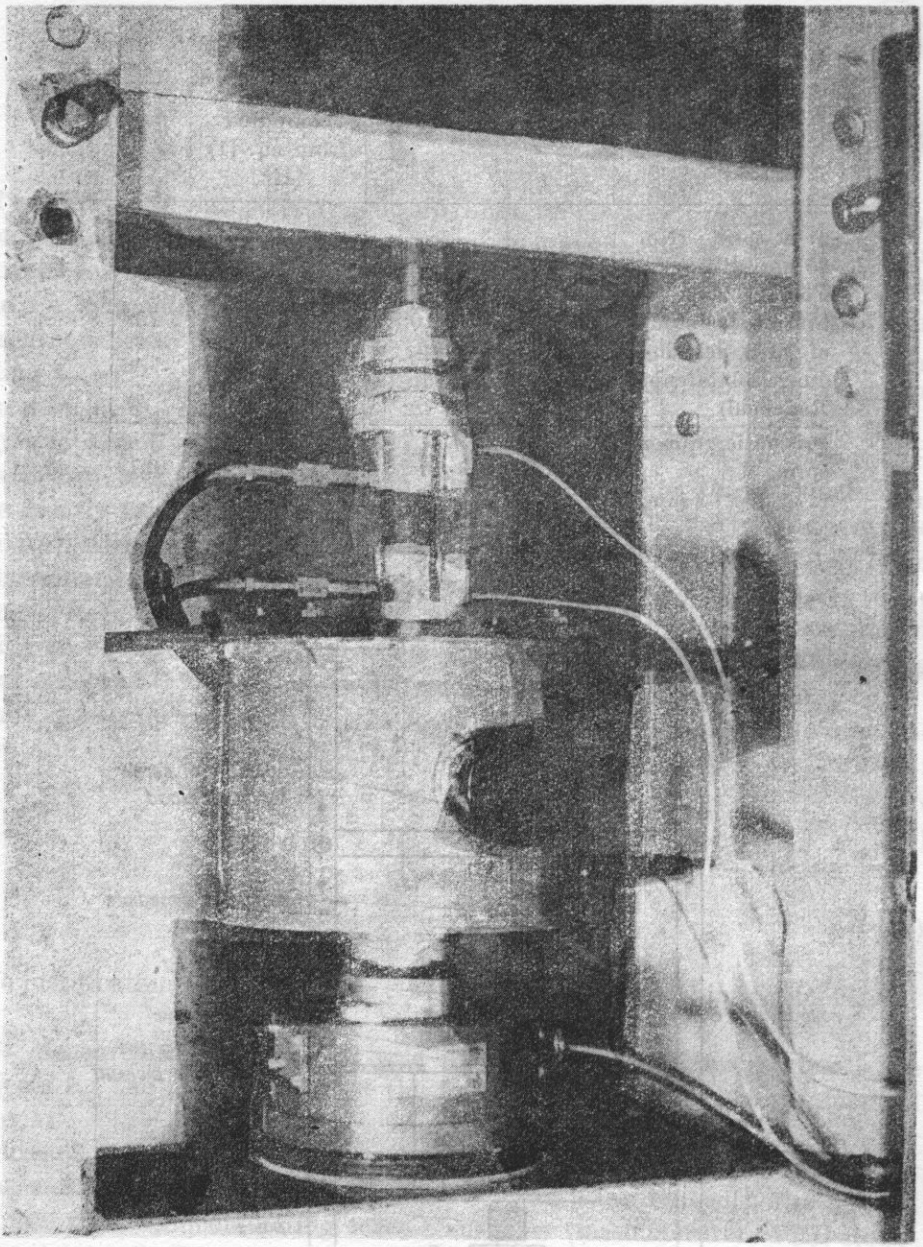

Fig. 4. Test arrangement for the measurement of the four-pole parameters of springs

It must be mentioned that it was not possible to measure the forces immediately at the boundary surfaces of the investigated springs, because additional masses (such as pressure plates, vibration pick-ups) were brought in between the electromechanical transducers of the load-cells and the test object. Considering Fig. 5 the measured forces F_{1m} and F_{2m} were corrected by in-phase substraction and addition of the mass forces. The measurement of the phase — angles was made by use of an RFT phase-detector.

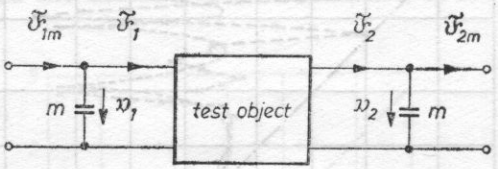

Fig. 5. Correction of the measured forces in the determination of the four-pole parameters of vibration isolators

$$\mathfrak{F}_1 = \mathfrak{F}_{1m} - j\omega v_1 m$$

$$\mathfrak{F}_2 = \mathfrak{F}_{2m} + j\omega v_2 m$$

2.4. Comparison of the four-pole parameters of different spring types determined in the experiments and with those found by computation. Figures 6 to 8 show the comparison between the four-pole parameters of the steel spring which were computed according to equation (9) and those obtained from measurement. The measurement results could be obtained from exact relationships in equations (14) to (17) as well as from the approximations (18) and (19). When comparing the exact calculation and the approximation of the parameters determined by the measurements, we find good agreement regarding the moduli as well as the phase angles of the four-pole parameters $\mathfrak{A}_{11}$, $\mathfrak{A}_{22}$ and $\mathfrak{A}_{21}$. Thus, it has been shown that approximations (18) and (19) are applicable not only outside the resonance frequencies.

The experimental measurement results and the theoretical computational results of the steel spring four-pole parameters do not show wide deviations regarding their essential characteristics. According to approximations (10) the frequency characteristics of the parameters $|\mathfrak{A}_{12}|$ and $|\mathfrak{A}_{21}|$ for $f < 100$ Hz come close to the straight lines of the mass impedance of the spring or the spring admittance. The first natural continuum frequency of the steel spring ($m = 80$ g, $n = 7.1 \cdot 10^{-5}\ \mathrm{s^2 \cdot kg^{-1}}$) as determined from equation (1) lies at $f_1 = 210$Hz. The first and second minimum of the measured frequency response of the parameters $|\mathfrak{A}_{11}|$ and $|\mathfrak{A}_{22}|$ lie — as can be expected from equation (9) — at $\frac{1}{2}f_1$ and $\frac{3}{2}f_1$. In the measured frequency response of $|\mathfrak{A}_{21}|$ evident minima appear with the necessary 180° jump in the phase angle in the investigated frequency range up to 1000 Hz at

$$f = \frac{\nu}{2}\sqrt{\frac{1}{mn}} \qquad (\nu = 1, 2, 3).$$

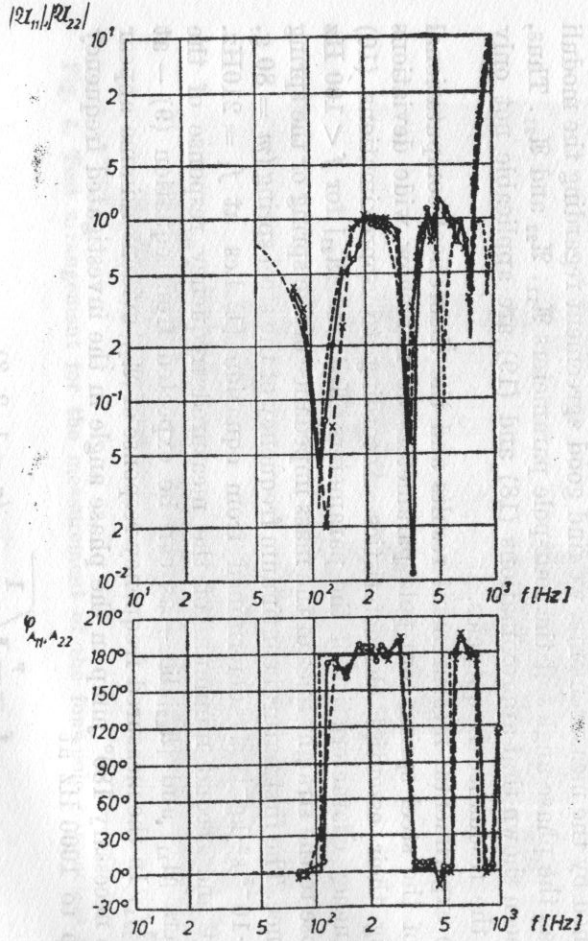

Fig. 6. Four-pole parameters $\mathfrak{A}_{11}$ and $\mathfrak{A}_{22}$ of a No. 25 steel spring

– – – theoretical curve using eq. (9), ×– – –× computed from measured data using eq. (16), ○——○ approximation using eq. (18)

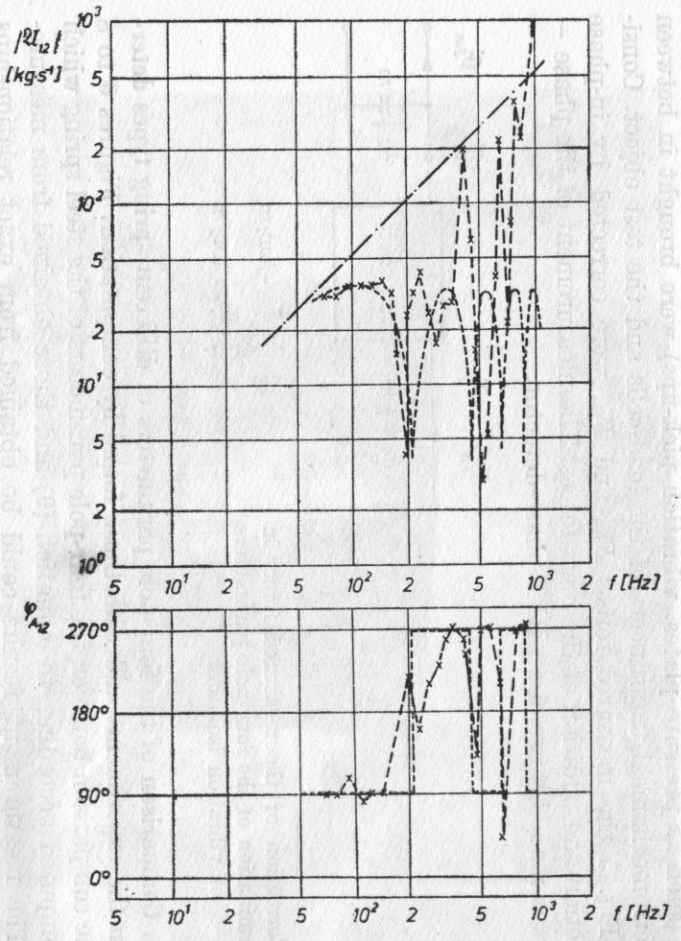

Fig. 7. Four-pole parameter $\mathfrak{A}_{12}$ of a No. 25 steel spring

– – – theoretical curve using eq. (9), ×– – –× computed from measured data using eq. (14), –·– mass impedance of the spring mass (m = 80 g)

To interpret the increase of maxima in the frequency response of $|\mathfrak{A}_{21}|$ we computed the theoretical response for different loss factors according to equation (8). The results were plotted in Fig. 9 to be compared with the measured frequency response of $|\mathfrak{A}_{21}|$. One finds that the increase in maxima of $|\mathfrak{A}_{21}|$ can be explained by a higher loss factor. At the same time the question is left open as to why there are still evident minima between the increasing maxima in the curve determined from measured results which do not appear in the theoretical results. Probably a damping law is concerned, which is unknown as yet, and which should be considered in the theoretical determination of the four-pole parameters of steel springs.

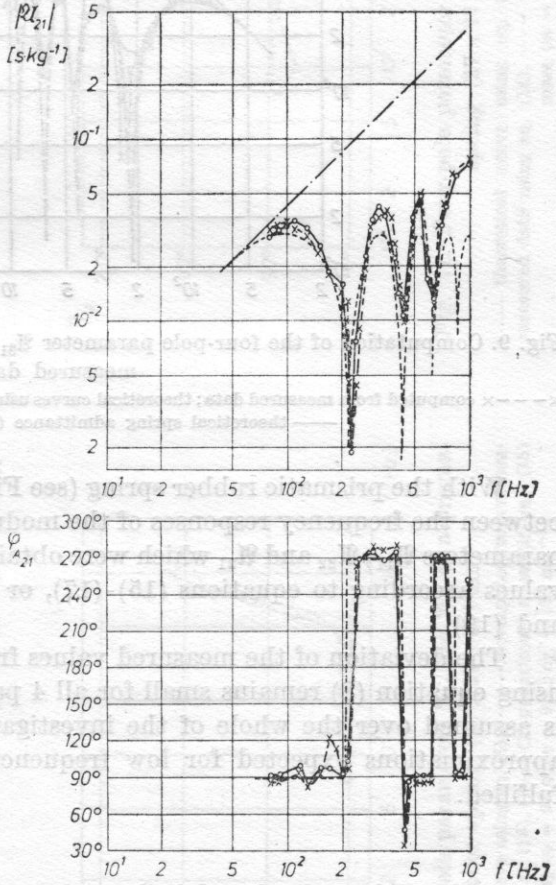

Fig. 8. Four-pole parameter $\mathfrak{A}_{21}$ of a No. 25 steel spring
– – – theoretical curve using eq. (9), ×– – –× computed from measured data using eq. (17), O——O approximation using eq. (19), –·– theoretical spring admittance ($n = 7.1 \cdot 10^{-5}$ s^2·kg^{-1})

The parameter $|\mathfrak{A}_{12}|$ in which one expects the same frequency response as in $|\mathfrak{A}_{21}|$ according to equation (9) shows only allusively a regularity in the position of the minima. The reason for this difference between the computed and the measured values lies in the difficulties occurring in the determination of $|\mathfrak{A}_{12}|$ from the measured values as has been mentioned already in section 2.2.

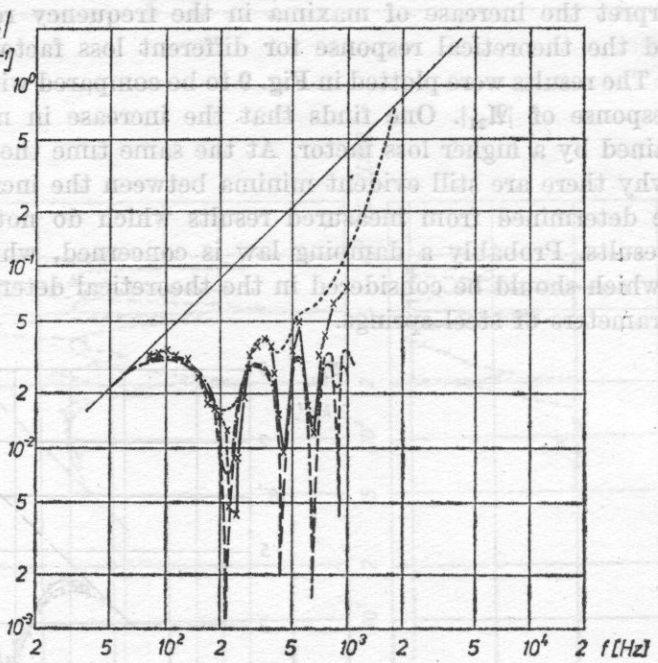

Fig. 9. Computation of the four-pole parameter $\mathfrak{A}_{21}$ of a No. 25 steel spring from theory and measured data

×– – –× computed from measured data; theoretical curves using eq. (8), – – – $\eta = 0.01$, –·– $\eta = 0.1$, ------ $\eta = 0.3$, —— theoretical spring admittance ($n = 7.1 \cdot 10^{-5}$ s^2·kg^{-1})

With the prismatic rubber spring (see Fig. 10 to 12) there is good agreement between the frequency responses of the moduli and phase angles of the four-pole parameters $\mathfrak{A}_{11}$, $\mathfrak{A}_{22}$ and $\mathfrak{A}_{21}$ which were obtained both exactly from the measured values according to equations (15)-(17), or approximately from equations (18) and (19).

The deviation of the measured values from the theoretical values computed using equation (8) remains small for all 4 parameters if a loss factor of $\eta = 0.1$ is assumed over the whole of the investigated frequency range. Obviously, the approximations expected for low frequencies according to equation (10) are fulfilled.

3. Examples of the application of the four-pole parameters of structure-borne sound isolators

3.1. Computation of the structure-borne sound isolation of a longitudinally vibrating continuum with an attached head mass. As a measure of the structure-borne sound isolation the ratio of the velocities v_1 and v_2 at the input or output of a vibration isolator which is installed in a spring — mass — system (see Fig. 13) will be considered. This velocity ratio characterizes the effect of a struc-

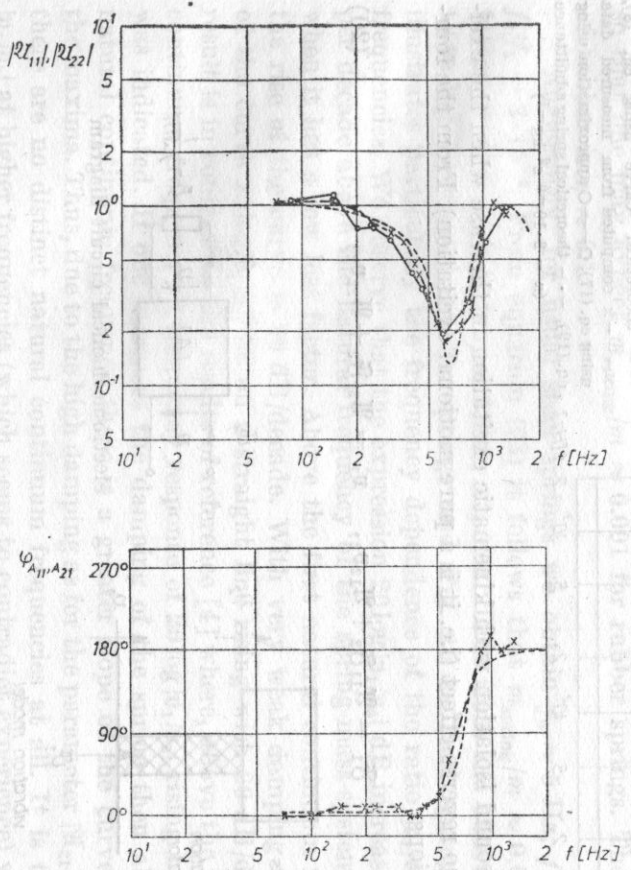

Fig. 10. Four-pole parameters $\mathfrak{A}_{11}$ and $\mathfrak{A}_{22}$ of a prismatic rubber spring $(27 \times 27 \times 63)$ mm³

------ theoretical curve using eq. (8), ×– – –× computed from measured data using eq. (16), O——O approximation using eq. (18) (l = 6.3 cm; m = 56 g; η = 0.1; c_L = 165 ms^{-1})

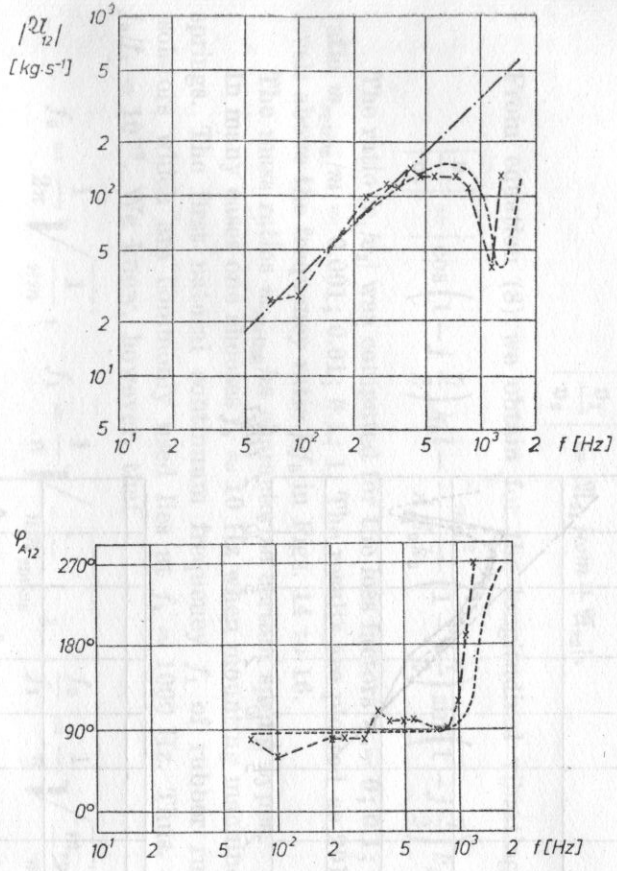

Fig. 11. Four-pole parameter $\mathfrak{A}_{12}$ of a prismatic rubber spring $(27 \times 27 \times 63)$ mm³

------ theoretical curve using eq. (8), ×– – –× computed from measured data using eq. (14), –·– mass impedance of the spring mass (m = 56 g)

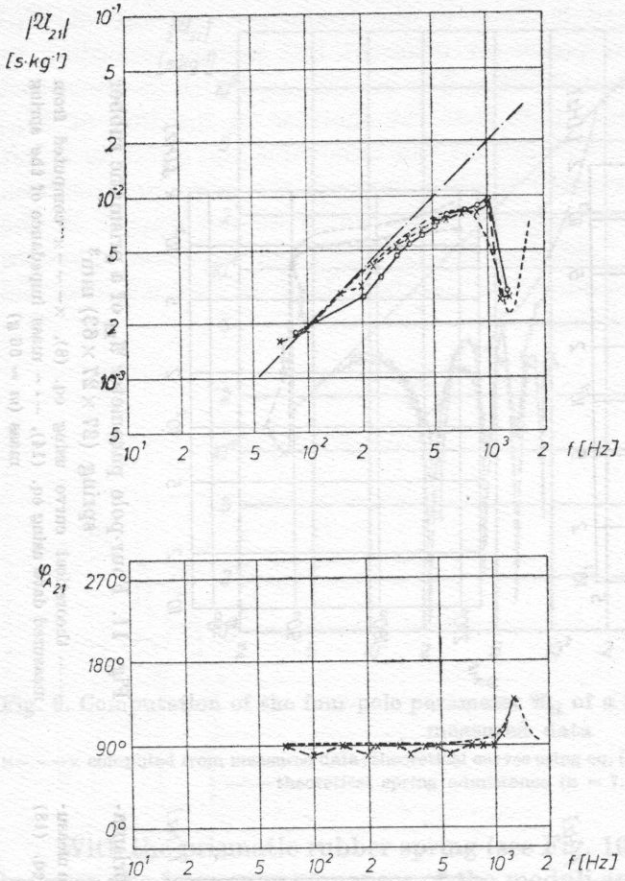

Fig. 12. Four-pole parameter $\mathfrak{A}_{21}$ of a prismatic rubber spring

------ theoretical curve using eq. (8), ×– – –× computed from measured data using eq. (17), O——O approximation using eq. (19), – · – theoretical spring admittance ($n = 3 \cdot 10^{-6}$ s^2·kg^{-1})

ture-borne sound isolation with kinematic excitation in the case when the excitation has no reverse effect (i.e. it is a pure motional excitation). From the four-pole equations

$$\mathfrak{F}_1 = \mathfrak{A}_{11}\mathfrak{F}_2 + \mathfrak{A}_{12}\mathfrak{v}_2, \qquad \mathfrak{v}_1 = \mathfrak{A}_{21}\mathfrak{F}_2 + \mathfrak{A}_{22}\mathfrak{v}_2, \tag{20}$$

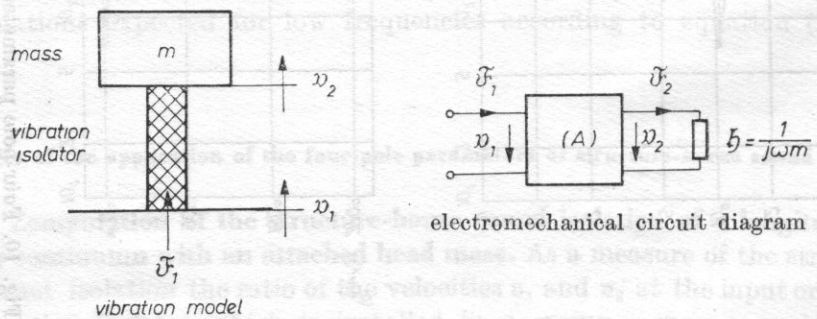

Fig. 13. Characterization of the structure-borne sound damping of vibration isolators

and the condition $\mathfrak{F}_2 = j\omega m \mathfrak{v}_2$ to be read from the circuit diagram (see. Fig. 13) one obtains as the modulus of the velocity ratio:

$$\left|\frac{\mathfrak{v}_1}{\mathfrak{v}_2}\right| = |\mathfrak{A}_{21} j\omega m + \mathfrak{A}_{22}|. \tag{21}$$

From equation (8) we obtain for the longitudinal vibrating continuum

$$\left|\frac{\mathfrak{v}_1}{\mathfrak{v}_2}\right| = \left|\cos\left(1-j\frac{\eta}{2}\right)k_0 l - \frac{m\omega^2}{AE_0 k_0}\left(1-j\frac{\eta}{2}\right)\sin\left(1-j\frac{\eta}{2}\right)k_0 l\right|. \tag{22}$$

The ratio $|\mathfrak{v}_1/\mathfrak{v}_2|$ was computed for the loss factors $\eta = 0;\ 0.1;\ 0.3$ with the ratio $m_{\text{spring}}/m = 0.001;\ 0.01;\ 0.1;\ 1$. The results are plotted as $20\log|\mathfrak{v}_1/\mathfrak{v}_2|$ dB levels above the frequency ratio f/f_0 in Figs. 14 to 16.

The mass ratios m_{spring}/m characterize certain spring types.

In many cases one chooses $f_0 \approx 10$ Hz when mounting machines on rubber springs. The first natural continuum frequency f_1 of rubber rubber spring isolators which are commonly used lies at $f_1 \approx 1000$ Hz. Thus, one obtains $f_0/f_1 = 10^{-2}$. We know, however, that

$$f_0 = \frac{1}{2\pi}\sqrt{\frac{1}{nm}}, \quad f_1 = \frac{1}{\pi}\sqrt{\frac{1}{nm_{\text{spring}}}}, \quad \frac{f_0}{f_1} = \frac{1}{\pi}\sqrt{\frac{m_{\text{spring}}}{m}},$$
$$\frac{m_{\text{spring}}}{m} \approx 10\cdot\left(\frac{f_0}{f_1}\right)^2, \tag{23}$$

so that one may expect $m_{\text{spring}}/m \approx 0.001$ for rubber springs. The loss factor of rubber is $\eta \approx 0.1$.

Analogously, for usual steel springs we obtain $f_0 \approx 5$ Hz, $f_1 \approx 150$ Hz, $f_0/f_1 = 3\cdot 10^{-2}$. From equation (23) it follows that $m_{\text{spring}}/m \approx 0.01$. The loss factor of steel springs is $\eta \approx 0.001, \ldots, 0.01$. Thus from the above considerations Fig. 14 refers to rubber springs and Fig. 15 to steel springs. Fig. 16 illustrates particularly the frequency dependence of the ratio $|\mathfrak{v}_1/\mathfrak{v}_2|$ at higher frequencies. We observe that the expression $20\log|\mathfrak{v}_1/\mathfrak{v}_2|$ dB increases by 40 dB per decade above the natural frequency of the spring-mass-system considered when it has a low loss factor. Above the first natural continuum frequency f_1 the rise of the curve is 80 dB/decade. With very weak damping the maxima of the curve $20\log|\mathfrak{v}_1/\mathfrak{v}_2|$ lie on a straight line rising with 20 dB/decade. This result is in contrast to the results of reference [4] where, above the first natural continuum frequency, a frequency response of $20\log|\mathfrak{v}_1/\mathfrak{v}_2|$ rising by 80/decade was indicated. If one increases the damping of the spring then above second natural continuum frequency there is a greater slope of the curve connecting the maxima. Thus, due to the high damping as for the parameter $|\mathfrak{A}_{21}|$ in Fig. 9 — there are no distinct natural continuum frequencies at all. It is this slope of $|\mathfrak{v}_1/\mathfrak{v}_2|$ at higher frequencies (which seems to contradict experience) which causes us to be interested in the following question: Can a strongly damped steel

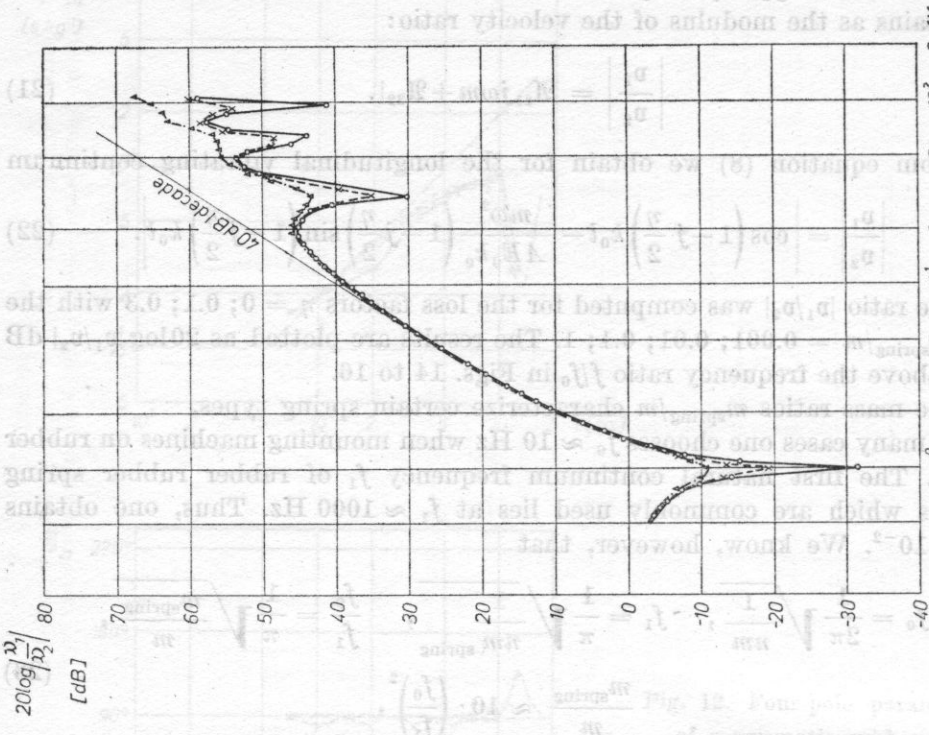

Fig. 15. Velocity ratio level $|v_1/v_2|$ for $m_{spring}/m = 0.01$
○——○ $\eta = 0$, × – – – × $\eta = 0.1$, △–·–△ $\eta = 0.3$

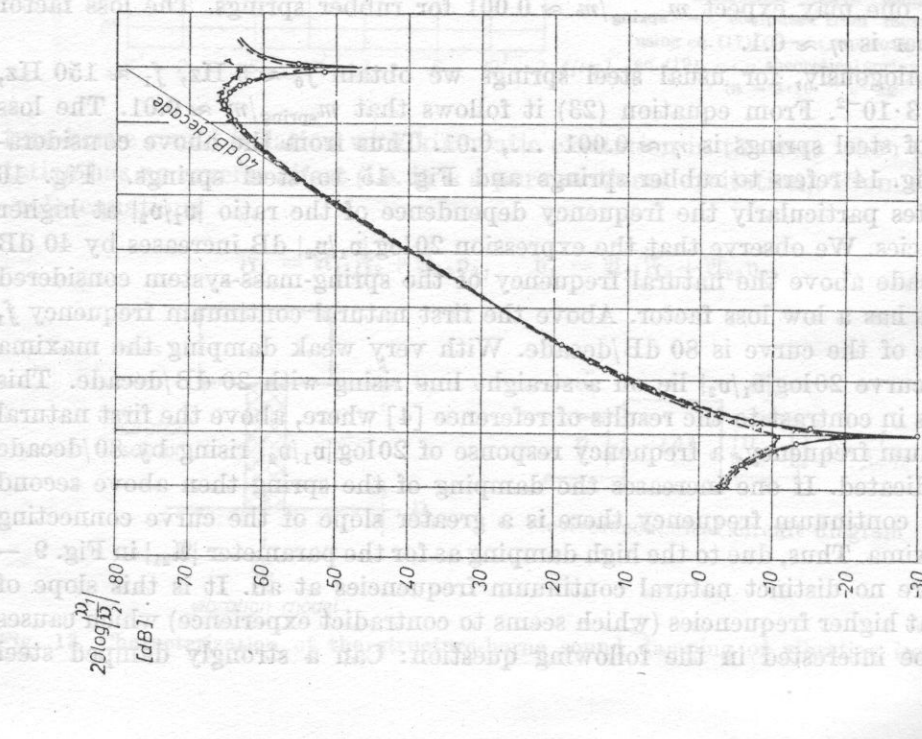

Fig. 14. Velocity ratio level $|v_1/v_2|$ for $m_{spring}/m = 0.001$
○——○ $\eta = 0$, × – – – × $\eta = 0.1$, △–·–△ $\eta = 0.3$

spring be more appropriate for structure-borne sound isolation than a rubber spring? Considering the available results this can be the case only if the $20\log|v_1/v_2|$ curve of the strongly damped steel spring will, due to its steeper

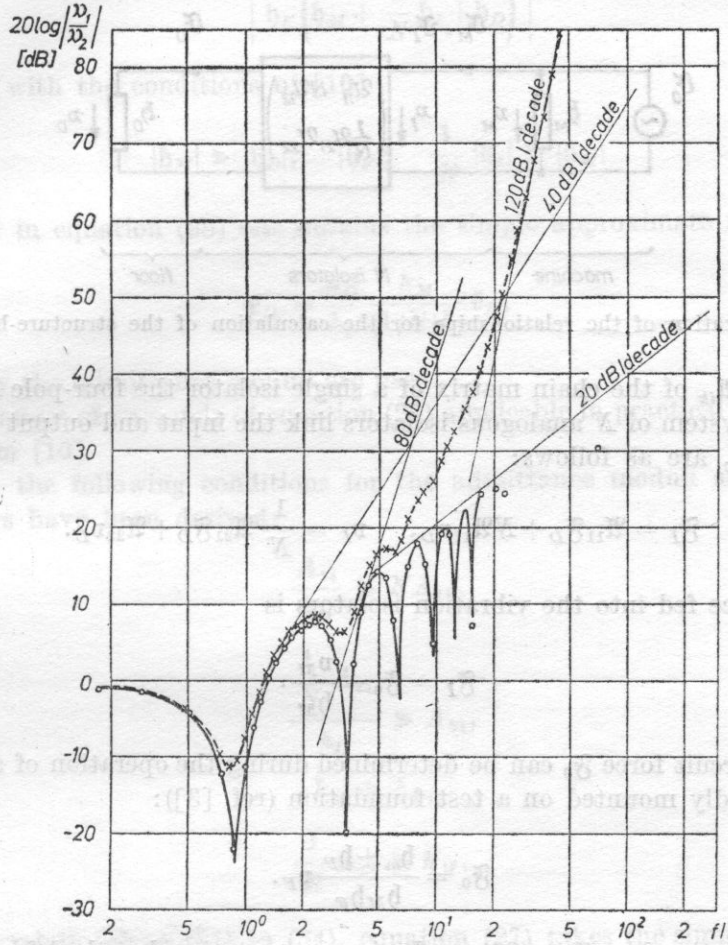

Fig. 16. Velocity ratio level $|v_1/v_2|$ for $m_{spring}/m = 1$
○——○ $\eta = 0$, ×– – –× $\eta = 0.3$

slope, intersect the curve of the rubber spring rising by 40 dB/decade above the second natural continuum frequency.

It can be seen from Fig. 15 that this circumstance will arise in the frequency range of interest (i.e. up to 1000 Hz) only if the steel spring isolators will have a loss factor $\eta \geqslant 0.3$ and if $m_{spring}/m \to 1$. This is realizable only by "series--connected lumped-parameter systems" containing additive damping elements or otherwise damped springs.

3.2. Computation of the structure-borne sound excitation at the place of mounting of elastically supported machines. The general case of machine mounting on isolators with natural continuum frequencies can be characterized by the electromechanical circuit diagram shown in Fig. 17. Including the complex

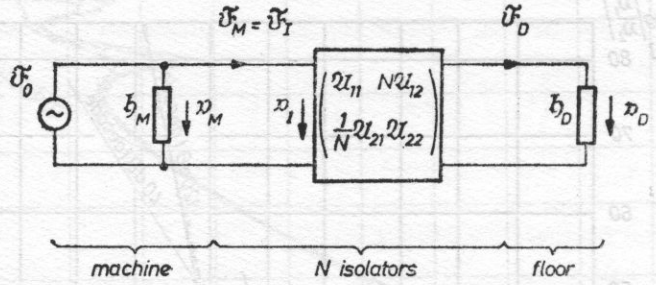

Fig. 17. Derivation of the relationships for the calculation of the structure-borne sound

coefficients $\mathfrak{A}_{ik}$ of the chain matrix of a single isolator the four-pole equations, which in a system of N analogous isolators link the input and output quantities (see Fig. 17), are as follows:

$$\mathfrak{F}_I = \mathfrak{A}_{11}\mathfrak{F}_D + N\mathfrak{A}_{12}\mathfrak{v}_D, \qquad \mathfrak{v}_I = \frac{1}{N}\mathfrak{A}_{21}\mathfrak{F}_D + \mathfrak{A}_{22}\mathfrak{v}_D. \tag{24}$$

The force fed into the vibration isolators is

$$\mathfrak{F}_I = \mathfrak{F}_0 - \frac{\mathfrak{v}_M}{\mathfrak{h}_M}. \tag{25}$$

The short-circuit force $\mathfrak{F}_0$ can be determined during the operation of a machine which is rigidly mounted on a test foundation (ref. [3]):

$$\mathfrak{F}_0 = \frac{\mathfrak{h}_m + \mathfrak{h}_F}{\mathfrak{h}_M \mathfrak{h}_F}\mathfrak{v}_F. \tag{26}$$

From relationships (24) - (26) we obtain a computational method for (multiplication) determining the rms. value of the velocity $\tilde{v}_D$ at the place of mounting of an elastically supported machine when the effective velocity $\tilde{v}_F$ (which is produced by the machine rigidly mounted on a test foundation) is known

$$\tilde{v}_D = \left| \frac{\mathfrak{h}_F + \mathfrak{h}_M}{\mathfrak{h}_F \mathfrak{h}_M \left[\left(\frac{\mathfrak{A}_{11}}{\mathfrak{h}_D} + N\mathfrak{A}_{12} \right) + \frac{1}{\mathfrak{h}_M} \left(\frac{1}{N}\frac{\mathfrak{A}_{21}}{\mathfrak{h}_D} + \mathfrak{A}_{22} \right) \right]} \right| \tilde{v}_F. \tag{27}$$

Assuming that the natural continuum frequency of the applied isolators does not lie within the frequency range up to 1000 Hz which is of interest, we can introduce the four-pole parameters of an ideal spring according to equation

(10) into eq. (27). It then becomes

$$\tilde{v}_D = \left| \frac{\mathfrak{h}_D(\mathfrak{h}_F + \mathfrak{h}_M)}{\mathfrak{h}_F\left(\mathfrak{h}_M + \frac{1}{N}\mathfrak{h}_I + \mathfrak{h}_D\right)} \right| \tilde{v}_F. \tag{28}$$

Now, with the conditions of [10]

$$|\mathfrak{h}_M| \gg |\mathfrak{h}_D|, \quad |\mathfrak{h}_F|; \quad \frac{1}{N}|\mathfrak{h}_I| \gg |\mathfrak{h}_M| \tag{29}$$

considered in equation (28) one obtains the simple approximate relationship:

$$\tilde{v}_D = \frac{h_D}{h_F}\frac{h_M}{(1/N)h_I}\tilde{v}_F, \tag{30}$$

where only the admittance moduli are used.

The ranges of operands of equation (27) applicable in practical cases can be taken from [10].

Thus, the following conditions for the admittance moduli and four-pole parameters have been derived:

$$\frac{A_{11}}{h_D} \gg NA_{12}, \tag{31}$$

$$\frac{\frac{1}{N}A_{21}}{h_D} \gg A_{22}, \tag{32}$$

$$h_M \gg h_F, \tag{33}$$

$$\frac{1}{N}A_{21} \gg h_M. \tag{34}$$

With relationships (31) to (34), equation (27) takes the simple form

$$\tilde{v}_D = \frac{h_D h_M}{h_F \frac{1}{N}A_{21}}\tilde{v}_F. \tag{35}$$

Here, $\mathfrak{A}_{21}$ proves to be the most important parameter for the computation of the structure-borne sound excitation. The four-pole parameter $|\mathfrak{A}_{21}|$ rather than the isolator admittance h_I is set in eq. (35) which makes a difference to equation (30).

Fig. 18 shows the comparison of the results computed from equations (27), (28), (30) and (35) with the measured results relating to the mounting of a machine model on No. 25 steel springs (electrodynamic exciter on steel

mass, see ref. [10]). For a quantity characterizing the difference between computation and measurement we used the level difference ΔL_v between the computed and the measured velocity level at the place of mounting:

$$\Delta L_v = 20 \log \frac{\tilde{v}_{D\,\mathrm{comp.}}}{\tilde{v}_{D\,\mathrm{measur.}}} \quad [\mathrm{dB}]. \tag{36}$$

One can see that by using the isolator admittance in equations (28) and (30) there is considerable deviation between computation and measurement at $f > 100$ Hz. However, the application of the four-pole parameters from equation (27) or the parameter A_{21} from equation (35) characterizes the effect of the natural continuum frequencies of the steel springs much better. The results of Fig. 8 can be used to show this. The modulus of the four-pole parameter $\mathfrak{A}_{21}$ for $f > 100$ Hz clearly remains below the theoretical admittance of the No. 25 steel spring. This means that the springs used seem to be considerably harder due to the natural continuum frequencies than is indicated by the spring constant. The increasing difference between $|\mathfrak{h}_I|$ and $|\mathfrak{A}_{21}|$ in Fig. 8 corresponds to the difference between the measurement and the computation according to equations (28) and (30) which increases with frequency (see Fig. 18).

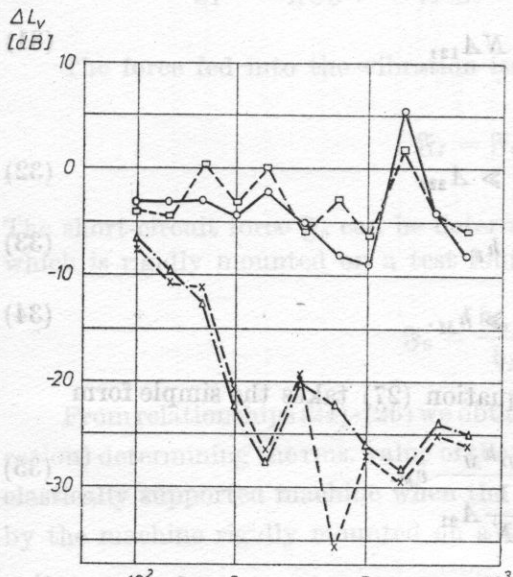

Fig. 18. Differences between the computed and measured velocity levels for the elastic mounting of a machine model on steel springs

○——○ computation with four-pole parameters using eq. (27), ×– – –× complex computation using eq. (28), △–·–△ approximation with h_I using eq. (35), □– – –□ approximation with $\mathfrak{A}_{21}$ using eq. (35)

The fact that the structure-borne sound excitation can be much better calculated by substituting A_{21} for h_I in equation (30) leads us to the conclusion that the compliance n of steel spring can be corrected above the first natural continuum frequency. Evidently, $h_I \approx A_{21}$, and with $h_I = \omega n$ for the steel

spring compliance (see eq. (9)) it follows that

$$n = \frac{1}{\omega} A_{21} \approx n_0 \frac{\sin k_0 l}{k_0 l} \tag{37}$$

(n_0 = steel spring compliance below the first natural continuum frequency).

On average, the compliance decreases with frequency and has additional minima at the natural continuum frequencies.

Experiments have shown that with rubber springs, due to the smaller influence of the natural continuum frequencies in the frequency range up to 1000 Hz, one can compute the structure-borne excitation from equation (30) and dispense with the four-pole parameters.

References

[1] L. Cremer, M. Heckl, *Körperschall*, Springer Verlag, Berlin – Heidelberg – New York 1967.

[2] J. J. Kljukin, *O kriterijach wibroizoljacii i sootnoszenijach mieżdu nimi*, Akusticzeskij Żurnał, **5**, 747-750 (1975).

[3] R. Melzig-Thiel, G. Meltzer, *Voraussetzungen und Ergebnisse bei der Berechnung der Körperschall-anregung von Gebäuden durch Maschinen*, Maschinenbautechnik **26**, 7, 306-310 (1977); **26**, 8, 371-374 (1977).

[4] E. Müller, G. Thien, G. Deutschbein, *Körperschalldämmung – Arbeitsfort-schrittsbericht, Referat auf der Informationstagung der FVV in Graz am 24.10.74*, Frankfurt/Main: Eigenverlag Daimler-Benz AG 1974, Schriftenreihe des Hrsg., Heft R 260.

[5] J. S. Snowdon, *Mechanical four-pole parameters and their application*, Journal of Sound and Vibration, **15**, 3, 307-324 (1971).

[6] J. Stenička, *Complex acoustical parameters of vibrating transmission through rubber insulators and their applications in experimental research*, Sammelband der 2. Nationalen Konferenz für Akustik, Varna 1975, Vortrag No. 3.

[7] P. Urban, *Theorie a metody mereni prenosu vibraci mechanickymi dily*, Studie CSAV, Praha; Academia 1973.

[8] P. Urban, *Untersuchungsmethoden der Schallausbreitung*, Proc. 7th ICA Congress, Budapest 1972, 19 N 7.

[9] J. Veit, *Bestimmung der Schallübertragungsdämpfung von Kompensatoren durch Messung ihrer Vierpolparameter Tagungsberichte, Der 5.* Tagung der Deutschen Arbeitsgemeinschaft für Akustik, DAGA 76 Heidelberg: o.V. 1976, 675-678.

[10] R. Melzig-Thiel, *Beiträge zur theoretischen und experimentallen Begründung eines Verfahrens für die Berechnung, Der Körperschallanregung von Gebäuden durch Maschinen*, Diss. A, Technische Universität Dresden, 1979.

Received on May 28, 1979; revised version on May 6, 1980.

ARCHIVES OF ACOUSTICS
5, 4, 337-346 (1980)

THE INFLUENCE OF THE ELECTRIC FIELD ON SURFACE WAVE PROPAGATION IN A PIEZOELECTRIC—SEMICONDUCTOR SYSTEM

Z. CEROWSKI, A. OPILSKI

Institute of Physics, Silesian Technical University
(44-100 Gliwice, ul. B. Krzywoustego 2)

The present paper describes the influence of a transverse electric field on surface wave propagation in a piezoelectric—semiconductor system, with consideration of surface states. The calculations show that a transverse electric field causes a change in the value of the attenuation coefficient and propagation velocity and can be used to control the magnitude of the attenuation.

1. Introduction

A surface Rayleigh wave with two displacement components causes longitudinal and transverse components of the acoustoelectric field to occur in a piezoelectric medium. The longitudinal acoustoelectrical field has been investigated in a number of papers [1-3]. Many aspects of the acoustoelectric transverse effect can be studied. Papers [4-7] report on the investigations of the acoustoelectric transverse effect, which determined the influence of various parameters on the electromotive force of the acoustoelectric transverse effect. The amplification of the wave can be controlled by the application of a variable electric field causing a transverse drift of the current carriers [8-10].

In a piezoelectric—semiconductor system without acoustic contact the electric field penetrates into the semiconductor to the depth of the screening radius [11]. At this depth the influence of the surface states is greatest. Thus account of the surface states [3] should be taken in consideration of the behaviour of acoustoelectronic phenomena.

This paper discusses the influence of a dc transverse electric field on Rayleigh surface wave propagation with consideration of the surface states.

2. The basic equations

In a piezoelectric–semiconductor system (Fig. 1) the wave propagating on the surface of the piezoelectric is described by the following equations

$$\varrho \frac{\partial^2 U_i}{\partial^2 t^2} = \frac{\partial T_{ik}}{\partial x_k}, \qquad T_{ik} = c_{iklm} U_{lm} - e_{jik} E_j^{(1)},$$
$$D_n^{(1)} = e_{nlm} U_{lm} - \varepsilon_{jm} E_j^{(1)}, \qquad \frac{\partial D_n^{(1)}}{\partial x_n} = 0, \tag{1}$$

where U_i are the displacement components, T_{ik} are the components of the strain tensor, U_{lm} are the components of the deformation tensor, $E_j^{(1)}$ are the components of the vector of the electric field in the piezoelectric, $D_n^{(1)}$ are the components of the vector of electric induction in the piezoelectric, c_{iklm} are the components of the tensor of the elastic constants, e_{ijk} are the components of the tensor of the piezoelectric constants, ε_{jm} are the components of the tensor of the dielectric permittivity, and ϱ is the density of the piezoelectric.

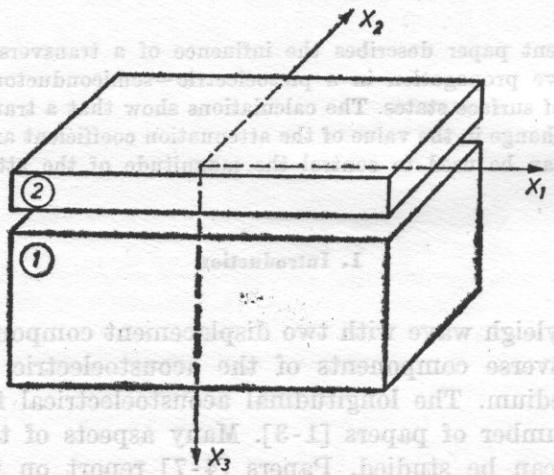

Fig. 1. The piezoelectric–semiconductor system in which a surface Rayleigh wave propagates

1 – piezoelectric, *2* – semiconductor, X_1 – the propagation direction of the wave, X_3 – the direction perpendicular to the propagation plane of the wave

In the piezoelectric, the electric field coupled with the surface wave, and the electric currents that it causes are described by the equations

$$\frac{\partial D_n}{\partial x_n} = -qn, \qquad j_k = \sigma_{ik} E_i^{(2)} + qD_{ik} \frac{\partial n}{\partial x_k},$$
$$\frac{\partial j_k}{\partial x_k} = q \frac{\partial n}{\partial t}, \tag{2}$$

where $D_n^{(2)}$ are the components of the vector of electric induction in the piezoelectric, n is the variation of the bulk density of the carriers caused by the wave, j_k are the components of the current, $E_i^{(2)}$ are the components of the vector of the electric field in the piezoelectric, σ_{ik} are the components of the tensor of electric conductivity, D_{ik} are the components of the tensor of the diffusion coefficient, and q is the charge of the carriers.

Assuming that the piezoelectric crystal is hexagonal and that the wave propagates in the plane (001) in the direction [100]; and after an isotropic approximation of the elastic, piezoelectric and electric constants [1, 3], i.e. introducing

$$c_{11}-c_{44}=c_{13}+c_{44}, \quad c_{33}=c_{11}, \quad c_{44}=\mu', \quad c_{13}=\lambda,$$

$$e_{31}=e_{15}=e, \quad e_{33}=-2e, \quad \varepsilon_{11}=\varepsilon_{22}=\varepsilon_{33}=\varepsilon,$$

equations (1) will take the following form

$$\begin{aligned} \varrho U_{1,tt} &= (\lambda+\mu')(U_{1,1}+U_{3,3})_{,1}+\mu'\,\Delta U_1+2e\varphi^{(1)}_{,13}\,, \\ \varrho U_{3,tt} &= (\lambda+\mu')(U_{1,1}+U_{3,3})_{,3}+\mu'\,\Delta U_3+e\varphi^{(1)}_{11}-2e\varphi^{(1)}_{,33}\,, \\ e(U_{1,13}+U_{3,11}-2U_{3,33})&-\varepsilon_0\varepsilon_1\,\Delta\varphi^{(1)}=0. \end{aligned} \tag{3}$$

Equations (2), after taking into account the external longitudinal electric field E_1 and the transverse field E_3 will be expressed in the following way

$$\operatorname{div}D^{(2)}=\varepsilon_0\varepsilon_2\,\Delta\varphi^{(2)}=-qn, \quad qn_{,t}=-\sigma\Delta\varphi^{(2)}+q\mu E_1 n_{,1}+q\mu E_3 n_{,3}+qD\Delta n. \tag{4}$$

Introducing the acoustic potentials as in [3] and considering that all the variable quantities in the piezoelectric depend on the coordinates and time as

$$\exp[i(kx_1-\omega t)+k\beta_n x_3],$$

where k is the wave number, ω is the angular frequency of the wave and β_n is the coefficient of penetration of the wave into the medium; from calculation by the method of successive approximations and considering that the value of the electromechanical coupling coefficient $\eta=e^2/\varepsilon_0\varepsilon_1\varrho a_2^2$ (a_2 is the propagation velocity of the transverse wave) is low, equations (3) give the coefficients of penetration of the wave, β_1, β_2, β_3 and the relations between the amplitudes Ψ, Φ, $\varphi^{(1)}$. Thus the solutions will have the form [3]

$$\begin{aligned} \Psi &= \sum_{n=1}^{3} A_n e[i(kx_1-\omega t)+k\beta_n x_3], \\ \Phi &= \sum_{n=1}^{3} B_n e^{[i(kx_1-\omega t)+k\beta_n x_3]}=\sum_{n=1}^{3} a_n A_n e^{[i(kx_1)-\omega t)+k\beta_n x_3]}, \\ \varphi^{(1)} &= \sum_{n=1}^{3} C_n e^{[i(kx_1-\omega t)+k\beta_n x_3]}=\sum_{n=1}^{3} \gamma_n A_n e^{[i(kx_1-\omega t)+k\beta_n x_3]}. \end{aligned} \tag{5}$$

3. The boundary conditions

The boundary conditions for the assumed piezoelectric – semiconductor system are the following:

– the elastic strains become zero

$$T_{3i} = 0, \quad i = 1, 2;$$

– the tangential components of the electric field are continuous

$$\varphi_{,1}^{(1)} = \varphi_{,1}^{(2)};$$

– the normal components of the vector of the electric induction are discontinuous

$$D_3^{(1)} - D_3^{(2)} = -qn_s,$$

where n_s is the variation in the surface density of the carriers in the conduction band,

$$D_3^{(1)} = -\varepsilon_0\varepsilon_1\varphi_{,3}^{(1)} + e(U_{1,1} - 2U_{3,3}), \qquad D_3^{(2)} = -\varepsilon_0\varepsilon_2\varphi_{,3}^{(2)}.$$

Considering that

$$n = F\exp[i(kx_1 - \omega t) - \Omega k x_3] \tag{6}$$

and thus from Poisson's equation

$$\varphi^{(2)} = (C_4 e^{-kx_3} + C_5 e^{-k\Omega x_3}) e^{i(kx_1 - \omega t)}. \tag{7}$$

Then considering that the equation of continuity for the layer at the surface has the form

$$qn_{s,3t} = -\sigma\varphi_{,11} + q\mu E_1 n_{s,13} + q\mu E_3 n_{s,33} + qDn_{s,113} - qn_{t,3t} \tag{8}$$

one obtains the boundary conditions in the form

$$\sum_{n=1}^{3} A_n[(\beta_n^2 - 1 + 2m)\alpha_n - 2im\beta_n - 2m\eta\gamma_n] = 0,$$

$$\sum_{n=1}^{3} A_n[2i\beta_n\alpha_n + 1 + \beta_n^2 + i\eta\gamma_n] = 0,$$

$$\sum_{n=1}^{3}\left\{\left[\left(C_n\beta_n + \frac{\varepsilon_2}{\varepsilon_1}(C_4 + \Omega C_5) - \frac{\varepsilon_2}{\varepsilon_1}\frac{C_n}{i\omega\tau_M\Omega\left(\gamma + \varkappa + i\Omega\dfrac{\mu k E_3}{\omega} + i\dfrac{\omega}{\omega_D}\right)}\right)\right]\gamma_n + \right.$$

$$\left. + [(1 + 2\beta_n^2)\alpha_n - 3i\beta_n]C_n\right\} = 0, \tag{9}$$

where Ω is the coefficient of penetration into the semiconductor [12], $n_t = \varkappa n_s$ is the surface density of the carriers in traps,

$$\varkappa = \tau_2(1+i\omega\tau_2)/\tau_1(1+\omega^2\tau_2^2)$$

is the occupation coefficient for the surface states [3],

$$\tau_1 = [C_n(N_t - n_{t0})]^{-1}$$

is the lifetime of the carriers in the conduction band,

$$\tau_2 = [C_n(n_{s0}+n_1)]^{-1}$$

is the lifetime of the carriers in the traps, C_n is the coefficient of capture of the carriers by the traps, N_t is the surface density of the traps, n_{to} is the filling density of the traps if no wave propagates, n_{so} is the surface density of the carriers in the conduction band in the equilibrium state, n_1 is the density of the carriers thermally ejected from the traps, F, C_4, C_5 are determined from the equation of continuity for the layer at the surface (8), Poisson's equation and the continuity of the tangential components of the electric field,

$$F = -\frac{\varepsilon_0\varepsilon_2 k^2 \sum_{n=1}^{3} C_n}{i\omega\tau_M q\left(\gamma+\varkappa+i\Omega\dfrac{\mu k E_3}{\omega}+i\dfrac{\omega}{\omega_D}\right)},$$

$$C_4 = \left[1-\frac{1}{i\omega\tau_M\left(\gamma+\varkappa+i\Omega\dfrac{\mu k E_3}{\omega}+i\dfrac{\omega}{\omega_D}\right)(1-\Omega^2)}\right]\sum_{n=1}^{3} C_n, \tag{10}$$

$$C_5 = \frac{1}{i\omega\tau_M\left(\gamma+\varkappa+i\Omega\dfrac{\mu k E_3}{\omega}+i\dfrac{\omega}{\omega_D}\right)(1-\Omega^2)}\sum_{n=1}^{3} C_n,$$

a_n, γ_n are the relations between A_n, B_n and C_n,

$$\tau_M = \omega_c = \sigma/\varepsilon_0\varepsilon_2$$

is the Maxwell frequency,

$$\gamma = 1+\mu k E_1/\omega$$

is the drift parameter and $\omega_D = v^2/D$ is the diffusion frequency.

4. The solution of the problem and conclusions

In order to determine the variation of the propagation velocity and of the attenuation coefficient, the determinant of the boundary conditions (9) $W(k)$ should be equated to zero and k should then be found from this equation.

Since $k = k_0 + k_1$, where k_1 results from the consideration of the piezoelectric effect, the surface states, the longitudinal and transverse electric fields, and thus $k_1 < k_0$, $W(k) = 0$ can be expanded into a series with respect to k_1. By inserting the expressions for C_4 and C_5 into the third boundary condition (9) we obtain

$$\sum_{n=1}^{3} C_n \left\{ \left[\beta_n + \frac{\varepsilon_2}{\varepsilon_1} - \frac{\varepsilon_2}{\varepsilon_1} \frac{2\Omega+1}{i\omega\tau_M \left(\gamma + \varkappa + i\Omega \frac{\mu k E_3}{\omega} + i\frac{\omega}{\omega t} \right) \Omega(1+\Omega)} \right] \gamma_n + \right.$$

$$\left. + (1+2\beta_n^2)\alpha_n - 3i\beta_n \right\} = 0, \qquad (11)$$

or in an approximate, but much more convenient form,

$$\sum_{n=1}^{3} C_n \left\{ \left[\beta_n + \frac{\varepsilon_2}{\varepsilon_1} - \frac{\varepsilon_2}{\varepsilon_1} \frac{p}{i\omega\tau_M \Omega \left(\gamma + \varkappa + i\Omega \frac{\mu k E_3}{\omega} + i\frac{\omega}{\omega_D} \right)} \right] \gamma_n + \right.$$

$$\left. + (1+2\beta_n^2)\alpha_n - 3i\beta_n \right\} = 0; \qquad (11a)$$

where $p = 1$ for $\Omega \ll 1$, $p = 3/2$ for $\Omega = 1$ and $p = 2$ for $\Omega \gg 1$.

Considering that $\Omega = \Omega_1 + i\Omega_2$ and analyzing the case $\Omega_2 \ll \Omega_1$ after the calculation of the variation of the propagation velocity and the attenuation coefficient we obtain the following expressions

$$\frac{\Delta v}{v} = \frac{\eta\omega\tau_M N_1}{M} \times$$

$$\times \frac{\omega\tau_M \left(1+\frac{\varepsilon_2}{\varepsilon_1}\right)(\gamma+a)^2 + \left(b + \Omega_1 \frac{\mu k E_3}{\omega} + \frac{\omega}{\omega_D}\right)\left[\left(1+\frac{\varepsilon_2}{\varepsilon_1}\right)\left(b+\Omega_1\frac{\mu k E_3}{\omega}\right)\omega\tau_M + \frac{p}{\Omega_1}\frac{\varepsilon_2}{\varepsilon_1}\right]}{\left(1+\frac{\varepsilon_2}{\varepsilon_1}\right)^2 (\gamma+a)^2\omega^2\tau_M^2 + \left[\left(1+\frac{\varepsilon_2}{\varepsilon_1}\right)(b+\Omega_1)\frac{\mu k E_3}{\omega} + \frac{\omega}{\omega_D}\right]\omega\tau_M + \frac{p}{\Omega_1}\frac{\varepsilon_2}{\varepsilon_1}\Omega_1}$$

$$a = -\frac{\eta\omega\tau_M N_1}{M} \times \qquad (12)$$

$$\times \frac{p\frac{\varepsilon_2}{\varepsilon_1}(\gamma+a)}{\left\{\left(1-\frac{\varepsilon_2}{\varepsilon_1}\right)^2(\gamma+a)^2\omega^2\tau_M^2 + \left[\left(1+\frac{\varepsilon_2}{\varepsilon_1}\right)\left(b+\Omega_1\frac{\mu k E_3}{\omega}+\frac{\omega}{\omega_D}\right)\omega\tau_M + \frac{p}{\Omega_1}\frac{\varepsilon_2}{\varepsilon_1}\right]^2\right\}\Omega_1},$$

where $a+ib = \varkappa$,

$$M = \frac{\partial N_2}{\partial \beta_n}\left(\frac{\partial \beta_n}{\partial k}\right) k = k_0,$$

$$N_1 = 3\beta_2\left[(\beta_1^2-1+2m)\frac{a_1}{2im}\,2m\beta_1-1-\beta_1^2+4m\beta_1\frac{a}{2im}-\right.$$

$$\left.-(1+\beta_2+\beta_2^2)\left[(\beta_1^2-1+2m)\frac{a}{2im}-3\beta_1\right]\right],$$

$$N_2 = (1+\beta_2^2)[(\beta_1^2-1+2m)\frac{a}{2im}-2m\beta_1+\beta_2\left(1+\beta_1^2-4m\beta_1\frac{a}{2im}\right).$$

The above expressions show that the values of the attenuation coefficient and the velocity depend on the longitudinal and transverse electric fields and on the parameters characterizing the surface states. The change in the sign of the attenuation coefficient, i.e. the change from attenuation to amplification can thus only be caused by a longitudinal field. The transverse field only changes the value of the attenuation coefficient and the velocity.

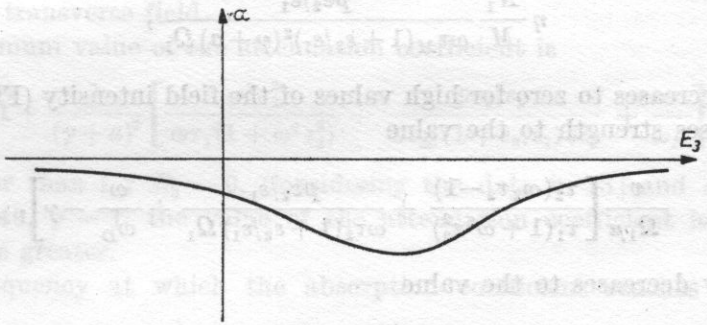

Fig. 2. The dependence of the attenuation coefficient on the transverse electric field E_3

The transverse field, depending on its direction of application, imposes an inflow or outflow of the energy carriers to the surface on which the wave propagates. In other words it causes a change in the conduction near this surface, and thus has an effect similar to that of illumination in the case of a photosemiconductor.

If the transverse field causes an outflow of the charge carriers from the surface, then as its value increases, the attenuation decreases, tending to zero for high values of the field intensity (Fig. 2). With increasing field strength the velocity increases to the value $\eta(N_1/M)(1+\varepsilon_2/\varepsilon_1)^{-1}$ (Fig. 3).

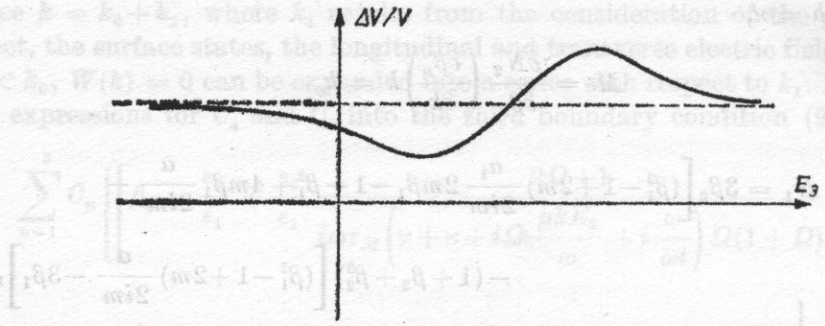

Fig. 3. The dependence of the relative change in the wave propagation velocity, on the transverse electric field E_3

If the transverse field causes an inflow of the charge carriers to the surface, then increasing the field strength to:

$$\frac{v}{\Omega_1\mu}\left[\frac{\omega\tau_2^2}{\tau_1(1+\omega^2\tau_M^2)}+\frac{p\varepsilon_2/\varepsilon_1}{\omega\tau_M(1+\varepsilon_2/\varepsilon_1)\,\Omega_1}+\frac{\omega}{\omega_D}\right]$$

the attenuation increases to the value

$$\eta\frac{N_1}{M}\,\frac{p\varepsilon_2/\varepsilon_1}{\omega\tau_M(1+\varepsilon_2/\varepsilon_1)^2(\gamma+a)\,\Omega_1},$$

and then decreases to zero for high values of the field intensity (Fig. 2). As the field increases strength to the value

$$\frac{v}{\Omega_1\mu}\left[\frac{\tau_2(\omega_2\tau_2-1)}{\tau_1(1+\omega^2\tau_2^2)}+\frac{p\varepsilon_2/\varepsilon_1}{\omega\tau_2(1+\varepsilon_2/\varepsilon_1)\,\Omega_1}+\frac{\omega}{\omega_D}-\gamma\right],$$

the velocity decreases to the value

$$\eta\frac{N_1}{M}\,\frac{2(\gamma+a)\left(1+\dfrac{\varepsilon_2}{\varepsilon_1}\right)\omega\tau_M-\dfrac{p}{\Omega_1}\dfrac{\varepsilon_2}{\varepsilon_1}}{2(\gamma+a)(1+\varepsilon_2/\varepsilon_1)^2\omega\tau_M},$$

and then increases, taking the value $\eta(N_1/M)(1+\varepsilon_2/\varepsilon_1)^{-1}$ for a field strength of

$$\frac{v}{\Omega_1\mu}\left[\frac{\omega\tau_2^2}{\tau_1(1+\omega^2\tau_2^2)}+\frac{p\varepsilon_2/\varepsilon_1}{\omega\tau_M(1+\varepsilon_2/\varepsilon_1)\,\Omega_1}+\frac{\omega}{\omega_D}\right],$$

increasing again to the value

$$\eta\frac{N_1}{M}\,\frac{2(\gamma+a)\left(1+\dfrac{\varepsilon_2}{\varepsilon_1}\right)\omega\tau_M+\dfrac{p}{\Omega_1}\dfrac{\varepsilon_2}{\varepsilon_1}}{2(\gamma+a)(1+\varepsilon_2/\varepsilon_1)\,\omega\tau_M}$$

at a field strength of

$$\frac{v_1}{\Omega_1 \mu}\left[\frac{\tau_2(1+\omega\tau_2)}{\tau_1(1+\omega^2\tau_2^2)}+\frac{p\varepsilon_2/\varepsilon_1}{\omega\tau_M(1+\varepsilon_2/\varepsilon_1)\,\Omega_1}+\frac{\omega}{\omega_D}+\gamma\right],$$

and with further increase in the field strength, the velocity variation decreases tending to the value $\eta(N_1/M)(1+\varepsilon_2/\varepsilon_1)^{-1}$ for high field intensities (Fig. 3).

These considerations lead to the conclusion that the value of the transverse field for which the variation of propagation velocity has an extremum and the attenuation its greatest value may be calculated using the parameters characterizing the semiconductor, i.e. the lifetime of the carriers in the conduction band τ_1 and the lifetime of the carriers in the traps τ_2. The behaviour of the attenuation coefficient with respect to the transverse field applied which was obtained in the present investigation was the same as in the experimental paper [9].

For the transverse field leading the charge carriers to the surface on which the wave propagates when its value is in the range

$$0 < E_3 < 2\frac{v}{\Omega_1 \mu}\left[\frac{\omega^2\tau_2^2}{\omega\tau_1(1+\omega^2\tau_2^2)}+\frac{p\varepsilon_2/\varepsilon_1}{\omega\tau_M(1+\varepsilon_2/\varepsilon_1)\,\Omega_1}+\frac{\omega}{\omega_D}\right],$$

the attenuation coefficient is greater, while in other ranges it is smaller than without the transverse field.

A maximum value of the attenuation coefficient is

$$1+\frac{1}{(\gamma+a)^2}\left[\frac{\omega^2\tau_2^2}{\omega\tau_1(1+\omega^2\tau_2^2)}+\frac{p\varepsilon_2/\varepsilon_1}{\omega\tau_M(1+\varepsilon_2/\varepsilon_1)\,\Omega_1}+\frac{\omega}{\omega_D}\right]$$

times greater than for $E_3 = 0$. Considering the data in [3] and $\omega\tau_M \approx 1$, $\varepsilon_2 = 10$, $\varepsilon_1 = 40$, $\gamma = 1$, the value of the attenuation coefficient is between 1 and 10 times greater.

The frequency at which the absorption coefficient reaches its highest value is

$$\omega_m = \frac{1}{\tau_M}\frac{p\varepsilon_2/\varepsilon_1}{\left(1+\frac{\varepsilon_2}{\varepsilon_1}\right)\left\{(\gamma+a)^2+\left[\frac{\omega^2\tau_2^2}{\omega\tau_1(1+\omega^2\tau_2^2)}+\frac{\omega}{\omega_D}+\Omega_1\frac{\mu k E_3}{\omega}\right]^2\right\}^{1/2}}.$$

If the transverse field leads the charge carriers and is

$$0 < E_3 < 2\frac{v}{\Omega_1 \mu}\left[\frac{\omega^2\tau_2^2}{\omega\tau_1(1+\omega^2\tau_2^2)}+\frac{\omega}{\omega_D}\right],$$

then the frequency at which the maximum absorption occurs is higher, while for other values and in the directions of E_3, it is lower than without the transverse field.

It follows from the above considerations that since with a transverse field one can change the value of the electronic attenuation (amplification), it has

a similar influence as a change in the illumination of the semiconductor. Affecting concentration variation by illumination requires photosensitive semiconductors and the possibility of illuminating them, which is not always possible. It is thus more convenient to cause changes in concentration by changes in the transverse electric field. It is significant for the determination of the value of the critical field. Measurements always provide the total attenuation coefficient, with consideration of the losses resulting from reasons other than electronic attenuation. The value of the critical field depends only on the propagation velocity and mobility, while the value of the attenuation coefficient also depends on the concentration of the carriers, which can be changed using illumination or, as was shown above, by a transverse field. By changing the concentration of the carriers we obtain various dependencies of the attenuation coefficient on the drift parameter, which will cross at a point where the parameter is zero.

References

[1] S. KALISKI, *Direct amplification of ultra- and hypersonic surface waves in the cristals of the wurtzite group*, Biul. WAT, **XVII**, 4, 3-25 (1978) (in Polish).

[2] J. W. GULAJEW et. al., *Ku teorii elektronnogo pogłosznia i usilenia powierhnostnych woln w piezokristallah*, Fiz. Twierd. Tieła, **12**, 9, 2595-2601 (1970).

[3] A. OPILSKI, *The influence of the surface states on the propagation of the ultra- and hypersonic surface waves in semiconductors*, Zeszyty Naukowe Politechniki Śląskiej, Matematyka–Fizyka, **27** (1975).

[4] A. M. KMITA, A. W. NIEDWIEDŹ, *Popiericznyj akusto-elektriczeskij efekt w słoistoj strukturie $LiNbO_3$–Si*, Żur. Eksp. Teoret. Fiz., **14**, 455-458 (1971).

[5] A. M. KMITA, A. W. NIEDWIEDŹ, *Akustoelektriczeskij efekt w słoistoj strukturie piezoelektrik–poluprowodnik*, Fiz. Twierd. Tieła, **14**, 9, 2646-2655 (1972).

[6] J. GULAEV et al., *Papierocznyj akustoelektroczeskij efekt nowogo tipa wyzywajemyj powierchnostnoj akusticzeskoj wołnoj w poluprowodnikie*, Żur. Eksp. Teoret. Fiz., **21**, 6, 353-355 (1975).

[7] J. W. GULAJEW et al., *Isledowanije nieliniejnych akustoelekriczeskich efektow i akustoprowodimost' w słoistoj strukturie* $LiNbO_3$–Si, Fiz. Tv. Tela, **17**, 12, 3505-3515 (1975).

[8] J. W. GULAJEW, W. W. DENISENKO, *Teoria usilenija powierhnostnyh zwukowyh woln popiericznym elektriczeskim tokom w piezoelektriczeskih poluprowodnikah*, Fiz. Tw. Tieła, **16**, 6, 1746-1751 (1974).

[9] A. M. KMITA, A. W. NIEDWIED, W. N. FEDOREC, *Wlijanije popiericznogo drejfa elektronow na pogłoszczenije powierhnostnyh akusticzeskih woln w* CdS, Fiz. Tw. Tieła, **18**, 12, 3610-3614 (1976).

[10] J. W. GULAJEW et al., *Wlijanije popiericznogo drejfa nositielej zariada na akustoelektronnoje wzaimodiejstwije w słoistoj strukturie piezoelektrik–poluprowodnik*, Fiz. Tw. Tieła, **11**, 1, 22-28 (1977).

[11] A. OPILSKI, *On the posibility of am investigation of semiconductor surface properties using ultrasonic surface waves*, Arch. Acoustics, **1**, 1, 29 (1976).

[12] Z. CEROWSKI, *The electrical field produced by an acoustic surface wave in a piezoelectric–semiconductor system*, Arch. Acoustics, **6**, 1 (1981).

Received on August 9, 1979; revised version on March 4, 1980.

ARCHIVES OF ACOUSTICS
5, 4, 347-362 (1980)

THE INVESTIGATION OF THE STABILIZATION OF THE STRUCTURE OF AQUEOUS SOLUTIONS OF HEXAMETHYLPHOSPHORTRIAMIDE USING AN ACOUSTIC METHOD

PIOTR MIECZNIK

Acoustics Department, Uniwersytet Adama Mickiewicza
(60-769 Poznań, ul. Matejki 48/49)

Measurements of the density and of ultrasonic velocity at a frequency of 15 MHz in aqueous solutions of hexamethylphosphortriamide (HMPT) over the temperature range 283.15-323.15 K for the whole concentration range are reported. On the basis of the quantities measured, the adiabatic compressibility, the deviation of the molar volume of the solution from the additive volume, the partial molar volumes and partial molar compressibilities of the components have been calculated.

The sharp extremes of the ultrasonic velocity, the adiabatic compressibility, the excess compressibility and the partial molar volumes occurring in the range of low concentrations of HMPT (0.04(323.15 K)-0.07(283.15 K) molar fraction) can be attributed to the stabilization of the structure of water in the solution in consequence of the growth of clathrate structures of composition $8X \cdot 136\ H_2O$. The variations of the dependence of the partial molar compressibilities of the components on the concentration indicate a strong intramolecular interaction between the components in a solution, and in particular, over the range of low HMPT concentrations.

1. Introduction

Many papers [4, 8-10] have reported investigations of the phenomenon of the stabilization of water by dissolving molecules of non-electrolytes in it. This phenomenon lies in a decrease of the thermal agitation of the molecules and the formation of intromolecular bonds in the water, while non-electrolyte additives act on the mutual ordering of the water molecules in the same way as a decrease in temperature. The efficiency of the additives in stabilizing the structure of the water and the mechanism of their action is conditioned by the structure of the molecules of the non-electrolytes. The stabilization of the structure can be observed in the region of relatively low concentrations of the non-aqueous component: $x_2 < 0.3$ molar fraction.

The phenomenon of structure stabilization, which occurs in the solution as a result of mutual intermolecular interaction, gives rise to extrema in many physical quantities as functions of concentration.

A characteristic feature of the aqueous solutions of non-electrolytes is, among other things, the occurrence of a maximum in the ultrasonic velocity and a minimum in the adiabatic compressibility as functions of concentration. The non-electrolytes, which show this type of behaviour in their aqueous solutions, include amines (ethyldiamine and benzoamine [11], acetic acid and dioxane [1]). A maximum in the propagation velocity of ultrasonic waves has also been observed in aqueous solutions of tetrahydrofran, 1,4-dioxane and *t*-butyl alcohol over the concentration range 0.03 - 0.08 mole fraction [2]. The position of the maximum is attributed to the formation of structures composed of stable threedimensional clathrate compounds of 17 hydrates, i.e. $8X \cdot 136H_2O$ (X is a non-electrolyte molecule).

CHEKALIN and SHAKHPARONOV [5], on the basis of the results of the measurements of the ultrasonic velocity and of radiospectroscopic investigations, showed that the dissolving of non-electrolyte molecules in water is accompanied by a change in the composition of the hydrogen bonds between the water molecules. The clathrate compounds form themselves in a similar way to the clathrate compounds in the hydrates of ice. In the voids of these compounds there are molecules of the nonelectrolyte. This causes a decrease in the compressibility, an increase in the viscosity, and in the ultrasonic velocity etc.

However, the occurrence of a maximum in the ultrasonic velocity in solutions is not always attributed to the formation of spatial structures. The maxima that occur in the ultrasonic velocity at a concentration of approximately 0.2 molar fraction in aqueous solutions of N-methylformamide, N,N-dimethylformamide and N,N-dimethylacetamide were attributed by KAWAIZUMI, OHNO and MIYAHARA [13] to the formation in the solution of unbounded compounds, with the position of the maximum velocity showing the type of these compounds.

The present paper attempts, on the basis of the results of the measurements of the ultrasonic velocity in, and the density of the medium, to determine the type of structure stabilization that occurs in aqueous solutions of hexamethylphosphortriamide (HMPT), a compound belonging to the group of weakly associated liquids.

2. The properties of hexamethylphosphortriamide ($[N(CH_3)_2]_3PO$) and its aqueous solutions

The hexamethyltriamide of orthophosphoric acid (HMPT) is a liquid of unstable structure [14]. The structure of the liquid HMPT is characterized by a small association (there is free rotation of the molecules, and HMPT has a relatively low packing coefficient $\psi = 0.51$). However, the possibility of the existence of associates with very short lifetimes cannot be excluded. The cha-

racter of the association is different from the association occurring in water. The packing of molecules in the liquid is not dense, and its character changes relatively easily with temperature ($-d\ln\varrho/dT = 8.82 \cdot 10^{-4}$ deg^{-1}, where ϱ is the density and T is the temperature).

On the basis of measurements of dielectric relaxation [7] and the proton spin – lattice relaxation [14], the following conclusions were drawn in relation to the structural changes occurring with the solution of HMPT molecules in water:

– the methyl HMPT groups exist in the voids of the structure of the water without noticeably reconstructing it;

– with concentrations of HMPT up to 0.1 molar fraction, the structure of the water is relatively weakly affected, and the process of its destruction increases with a concentration of 0.5 molar fraction;

– water weakly affects the HMPT structure;

– for small amounts of solute, the HMPT molecules, which form hydrogen bonds with the water through the oxygen beside the phosphorus, do not destroy the lattice of hydrogen bonds; in

– the stability of the structure of the solution over a concentration range of 0-0.15 molar fraction of HMPT is much greater than that for pure water.

The results of the investigation of the properties of the HMPT water solutions reported in [7, 14] do not, however, give an unambiguous answer to the question of the character of the intermolecular interactions, particularly for low concentration of HMPT. It is therefore useful to conduct additional investigations using the methods of molecular acoustics.

3. The method of investigation

The measurements of the ultrasonic velocity in aqueous solutions of hexamethylphosphartriamide were performed with a pulse – phase interferometer at a frequency of 15 MHz. The measurement error did not exceed 0.1%. The medium investigated was thermostabilized with a precision of 0.05 K, while the temperature measurements were performed using copper – constantan thermocouple connected with a digital voltmeter, permitting the temperature to be read with a precision of 0.025 K. The measurements of density were performed by the pycnometric method with a precision of 0.02%. The p.f. brand HMPT of West German production and double distilled water were used in the investigations.

The ultrasonic velocity and the density of the medium. The experimental results of the measurements of the density of the medium and of the ultrasonic velocity in aqueous solutions of HMPT as functions of concentration and temperature are shown in Table 1, while. Fig. 1 shows the temperature dependence of the ultrasonic velocity for individual concentrations. It follows from these

Table 1. The measured results of the ultrasonic velocity and density in aqueous solutions of hexamethylphosphortriamide

x_2 [molar fraction]	t [K]									
	283.15		293.15		303.15		313.15		323.15	
	ϱ $\left[\frac{10^3\,kg}{m^3}\right]$	v $[m \cdot s^{-1}]$	ϱ $\left[\frac{10^3\,kg}{m^3}\right]$	v $[m \cdot s^{-1}]$	ϱ $\left[\frac{10^3\,kg}{m^3}\right]$	v $[m \cdot s^{-1}]$	ϱ $\left[\frac{10^3\,kg}{m^3}\right]$	v $[m \cdot s^{-1}]$	ϱ $\left[\frac{10^3\,kg}{m^3}\right]$	v $[m \cdot s^{-1}]$
0.000	0.9997	1448	0.9982	1483	0.9957	1510	0.9922	1529	0.9881	1542
0.005	1.0038	1490	1.0020	1520	0.9992	1540	0.9954	1555	0.9910	1566
0.020	1.0165	1608	1.0133	1611	1.0095	1612	1.0050	1611	0.9999	1604
0.050	1.0383	1714	1.0326	1692	1.0261	1670	1.0194	1646	1.0127	1619
0.100	1.0559	1707	1.0479	1675	1.0398	1642	1.0314	1606	1.0230	1566
0.125	1.0589	1686	1.0504	1650	1.0420	1616	1.0335	1580	1.0248	1545
0.150	1.0606	1662	1.0521	1627	1.0431	1592	1.0342	1557	1.0253	1520
0.200	1.0605	1618	1.0515	1581	1.0426	1547	1.0334	1511	1.0244	1471
0.275	1.0574	1566	1.0485	1531	1.0394	1495	1.0304	1459	1.0213	1424
0.492	1.0490	1476	1.0400	1440	1.0310	1405	1.0220	1369	1.0130	1331
0.691	1.0430	1433	1.0342	1390	1.0255	1357	1.0169	1320	1.0082	1290
1.000	1.0365	1385	1.0282	1350	1.0201	1312	1.0120	1274	1.0038	1242

dependencies that for concentration $x_2 = 0.005$ molar fraction (curve *2*) the character of the change is similar to that for water, while for a concentration of 0.02 molar fraction (curve *3*) the velocity is, over a certain temperature range, independent of temperature. For concentrations above 0.02 molar fraction, the character of the variation is analogous to that for pure water, which indicates a destruction of the previous structure of water (i.e. the hydrogen bonds between the water molecules have changed their distribution).

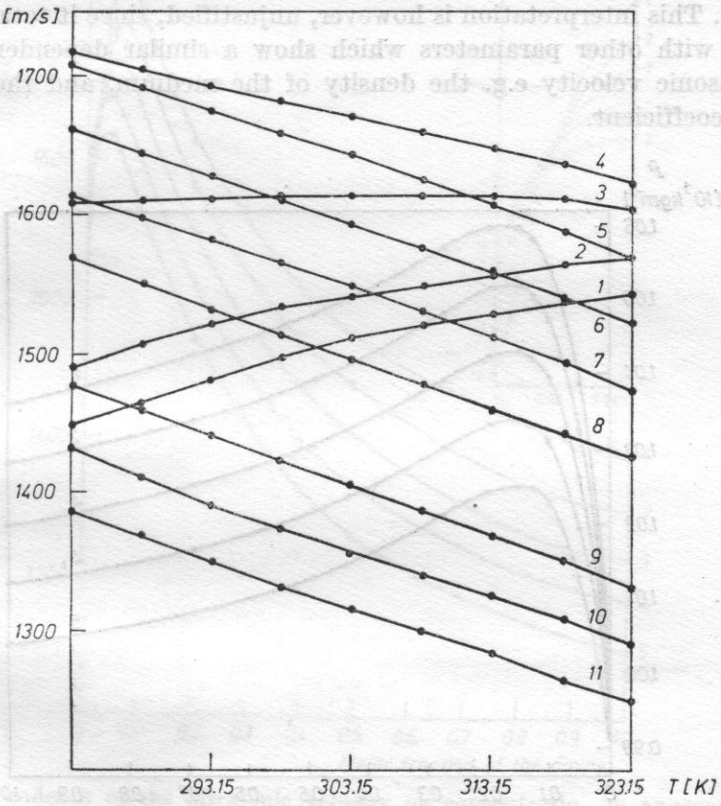

Fig. 1. The dependence of the ultrasonic velocity on temperature in aqueous solutions of HMPT

curves *1-11* corespond to concentrations of 0.000, 0.005, 0.020, 0.050, 0.100, 0.150, 0.200, 0.275, 0.492, 0.691, 1.000 molar fraction of amide

Figs. 2 and 3 show respectively the concentration dependencies of the density of the medium and the ultrasonic velocity. For both the density of the medium and ultrasonic velocity a maximum occurs at a well defined compositions of the solution. (The maximum density occurs for $x_2 \cong 0.15$ molar fraction; while a sharp maximum in the velocity occurs over the concentration range 0.04 (323.15 K)-0.07 (283.15 K) molar fraction of amide.) With an increase in the temperature this maximum thus shifts towards lower concentrations of HMPT, as for aqueous solutions of alcohols [16]. The point of intersection of

the two curves of the velocity at the different temperatures occurs for a concentration $x_2 = 0.021$ molar fraction; and the velocity does not depend on temperature (in the temperature range 283.15-313.15 K).

The phenomenon of the intersection of the curves of the ultrasonic velocity as a function of concentration, can be observed in many aqueous solutions of non-electrolytes [6, 16]. ENDO [6] interprets the occurrence of this phenomenon as the formation in the solution of clathrate compounds, with the concentration corresponding to the intersection of the curves indicating their composition. This interpretation is however, unjustified, since it totally neglects comparison with other parameters which show a similar dependence to that of the ultrasonic velocity e.g. the density of the medium, and the ultrasonic absorption coefficient.

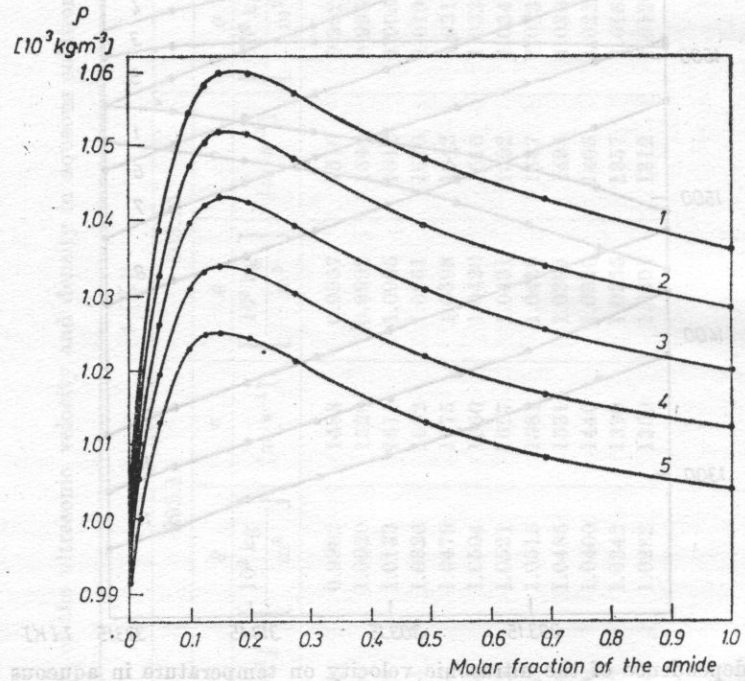

Fig. 2. The concentration dependence of the density in aqueous solutions of HMPT
curves *1-5* correspond to temperatures of 283.15, 293.15, 303.15, 313.15, 323.15 K

Adiabatic compressibility and the excess compressibility of solutions. On the basis of the measured values of the ultrasonic velocity in, and the density of the medium, the adiabatic compressibility of the solutions β_s was calculated. Two facts should be noted in the analysis of the concentration dependence of β_s shown in Fig. 4; the occurrence of the minimum; and the point of the intersection of the curves, which is independent of time. The former corresponds with the occurrence of the maxima in the ultrasonic velocity and in the density;

while the latter, corresponds with the occurrence of the intersection of the curves of ultrasonic velocity at different temperatures. The minimum in the adiabatic compressibility in aqueous solutions of HMPT (Fig. 4) occurs over the same concentration range as the maximum velocity (Fig. 3).

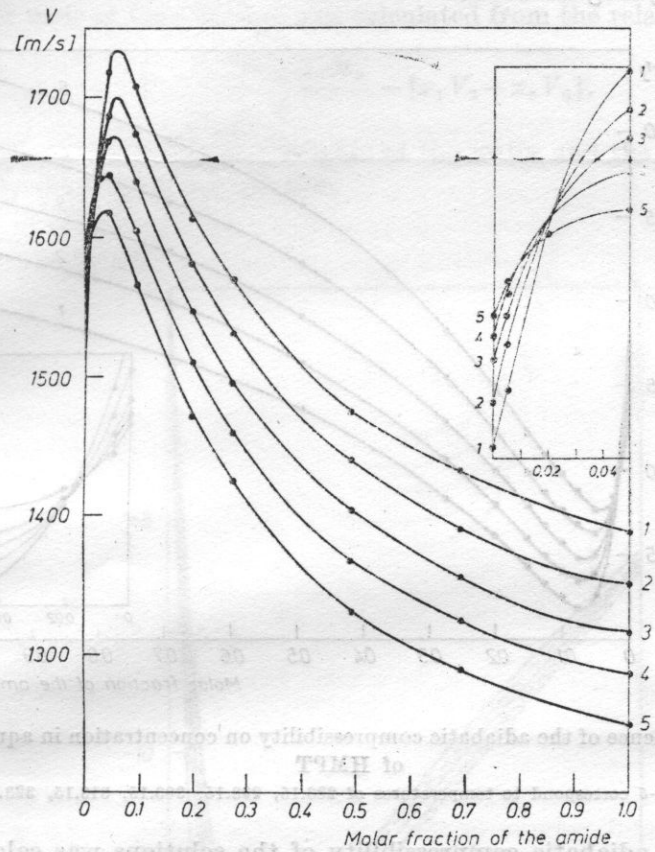

Fig. 3. The dependence of the ultrasonic velocity on concentratio in aqueous solutions of HMPT

curves *1-5* correspond to temperatures of 283.15, 293.15, 303.15, 313.15, 323.15 K

The sharp extrema of the adiabatic compressibility and the ultrasonic velocity occurring over the concentration ranges of 0.04 (323.15 K)-0.07 (283.15 K) molar fraction indicate that the greatest structural stability is achieved over this concentration range. It is thus most likely that the clathrate compounds $8X \cdot 136H_2O$ will form in the solution, where the molecules of HMPT enter the voids of the hexadecahedra formed by the water molecules. The formation of the clathrate compounds causes a decrease in the adiabatic compressibility and an increase in the ultrasonic velocity in the solution, which proceeds until the voids are totally filled. Further increase in the compressibility is conditioned by the occurrence in the solution of additional molecules of amide,

which do not enter the voids of the clathrate compounds. The destruction of the clathrate compounds is indicated by the occurrence for $x_2 \cong 0.15$ molar fraction of a maximum in the density of the medium, where the structure is most densely packed, and for which the water molecules are linked to the amide molecules by hydrogene bonds.

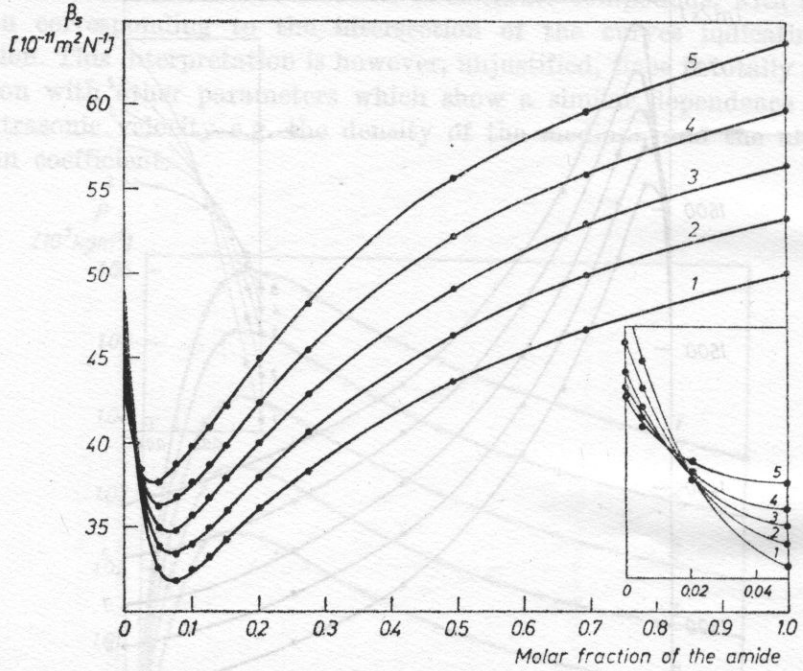

Fig. 4. The dependence of the adiabatic compressibility on concentration in aqueous solutions of HMPT

curves *1-5* correspond to temperatures of 283.15, 293.15, 303.15, 313.15, 323.15 K

The excess adiabatic compressibility of the solutions was calculated from relation

$$\beta_s^D = \beta_s - \frac{1}{V}[x_1 V_1 \beta_{s,1} + x_2 V_2 \beta_{s,2}], \tag{1}$$

where x_1, x_2 are the molar fractions of water and amide respectively; $V = x_1 V_1 + x_2 V_2$ is the volume of a mole of the solution calculated in an additive manner; V_1, V_2 are the molar volumes of water and amide, respectively; $\beta_{s,1}$, $\beta_{s,2}$ respectively, the adiabatic compressibilities of the water and the amide.

It follows from the results shown in Fig. 5 that the values of β_s^D are always negative, i.e. the β_s are lower than those of the compressibility calculated in an additive manner. The solution of HMPT in water causes a decrease in the excess compressibility of the solution to a particular concentration

(0.07(283.15 K)-0.125(323.15 K) molar fraction, beyond which further addition of the amide causes an increase.

The additional molar volume of the solutions and the partial molar volumes of the components in the solution. The change in the volume of the solution prepared, per mole of the solution, was calculated from the relation

$$\Delta V = \frac{x_1 M_1 + x_2 M_2}{\varrho} - [x_1 V_1 + x_2 V_2], \qquad (2)$$

where M_1, M_2 are the molecular weights of the water and the amide, respectively; ϱ is the density of the solution.

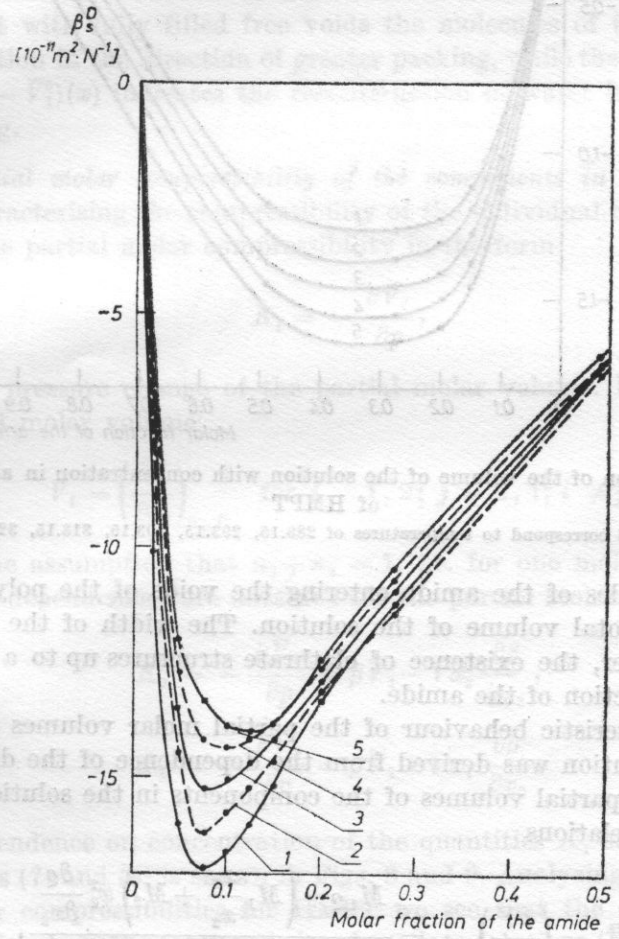

Fig. 5. The dependence of the excess adiabatic compressibility on concentration in aqueous solutions of HMPT

curves *1-5* correspond to temperatures of 283.15, 293.15, 303.15, 313.15, 323.15 K

The deviation of the volume of the solution from the simple additive volume as a function of concentration is shown in Fig. 6. A decrease in the

volume of the solution, which takes its extreme value over the concentration range 0.2-0.5 molar fraction, can be observed for the whole concentration range. A decrease in the molar volume of the solution accompanying the solution of the amide in water also confirms the formation of the clathrate structures,

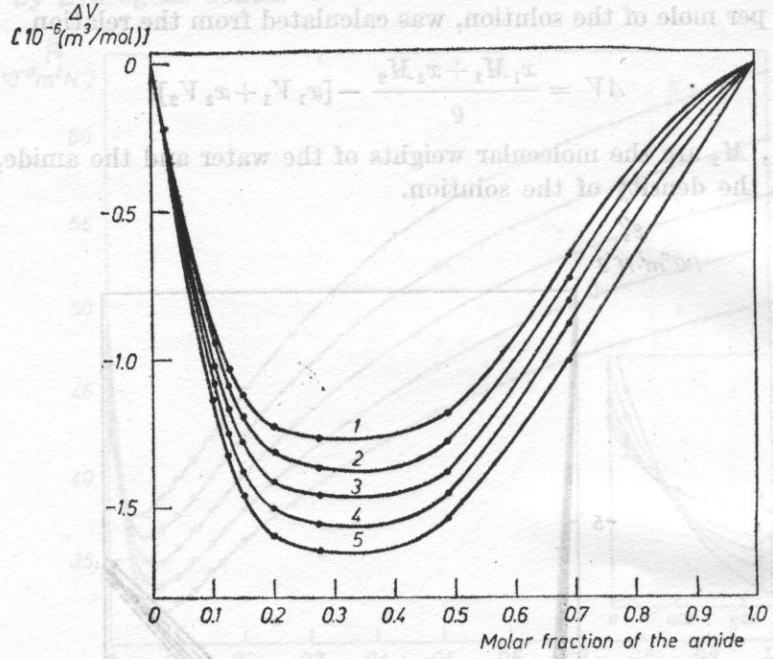

Fig. 6. The variation of the volume of the solution with concentration in aqueous solutions of HMPT

curves *1-5* correspond to temperatures of 283.15, 293.15, 303.15, 313.15, 323.15 K

with the molecules of the amide entering the voids of the polyhedrons, thus decreasing the total volume of the solution. The width of the minimum ΔV suggests, however, the existence of clathrate structures up to a concentration of 0.5 molar fraction of the amide.

The characteristic behaviour of the partial molar volumes of the components in the solution was derived from the dependence of the density on concentration. The partial volumes of the components in the solution were calculated from the relations

$$\overline{V}_1 = \left(\frac{\partial V}{\partial n_1}\right)_{n_2,T} = \frac{M_1\varrho + \left(M_1\frac{x_1}{x_2} + M_2\right)x_2^2\frac{\partial\varrho}{\partial x_2}}{\varrho^2}, \tag{3}$$

$$\overline{V}_2 = \left(\frac{\partial V}{\partial n_2}\right)_{n_1,T} = \frac{M_2 - \left(M_1 + \frac{x_2}{x_1}M_2\right)x_1^2\frac{\partial\varrho}{\partial x_2}}{\varrho^2}, \tag{4}$$

while Fig. 7 shows the dependence on concentration of the difference of the molar volumes of the components in the solution (V_1 and V_2) and the molar volumes for an infinite dilution ($\overline{V}_1^0$ and $\overline{V}_2$). It follows from the curves that a decrease in the molar volume of the amide occurs in the solution, reaching its extreme value for $x_2 \cong 0.05$ molar fraction, beyond which it rapidly increases up to a concentration of 0.2 molar fraction. Contrary to the behaviour of the molar volume of HMPT in the solution, an increase in the molar volume occurs at a concentration of 0.05 molar fraction.

The character of the curves for the aqueous solutions of HMPT shown in Fig. 7 is analogous to that of the aqueous solutions of alcohols [15] and amines [12]. The sharp minimum of the function $(\overline{V}_2 - \overline{V}_2^0)(x)$ for $x_2 = 0.05$ molar fraction confirms the existence of the clathrate structures in the solution and indicates that with fully filled free voids the molecules of the amide change their distribution in the direction of greater packing, while the maximum of the function $(\overline{V}_1 - \overline{V}_1^0)(x)$ indicates the reconstruction of water in the direction of lower packing.

The partial molar compressibility of the components in the solution. The quantity characterizing the compressibility of the individual components in the solution is the partial molar compressibility in the form

$$K_i = -\frac{\partial \overline{V}_i}{\partial p}, \tag{5}$$

which is the pressure change of the partial molar volume. By differentiation of the partial molar volume

$$\overline{V}_i = \left(\frac{\partial V}{\partial n_i}\right)_{n_j,T} \quad \text{for } i = 1,2;\ j = 2,1;\ i \neq j, \tag{6}$$

and under the assumption that $n_1 + n_2 = 1$, i.e. for one mole of the solution, the following dependencies are obtained for the partial molar compressibilities:

$$K_1 = -\frac{\partial \overline{V}_1}{\partial p} \equiv \beta \overline{V}_1 - V x_2 \frac{\partial \beta}{\partial x_2}, \tag{7}$$

$$K_2 = -\frac{\partial \overline{V}_2}{\partial p} = \beta \overline{V}_2 + V x_1 \frac{\partial \beta}{\partial x_2}. \tag{8}$$

The dependence on concentration of the quantities K_1 and K_2 determined from relations (7) and (8) is shown in Figs. 8 and 9. Analyzing the curve for the partial molar compressibilities for HMPT we see that the compressibility of an amide molecule in the solution is low for dilute solutions (Fig. 9), with a subsequent increase up to an concentration of 0.075 molar fraction. There is a characteristic point of inflexion at a concentration of 0.05 molar fraction, beyond which the increase in K_2 is very rapid. Contrary to the behaviour of the adiabatic

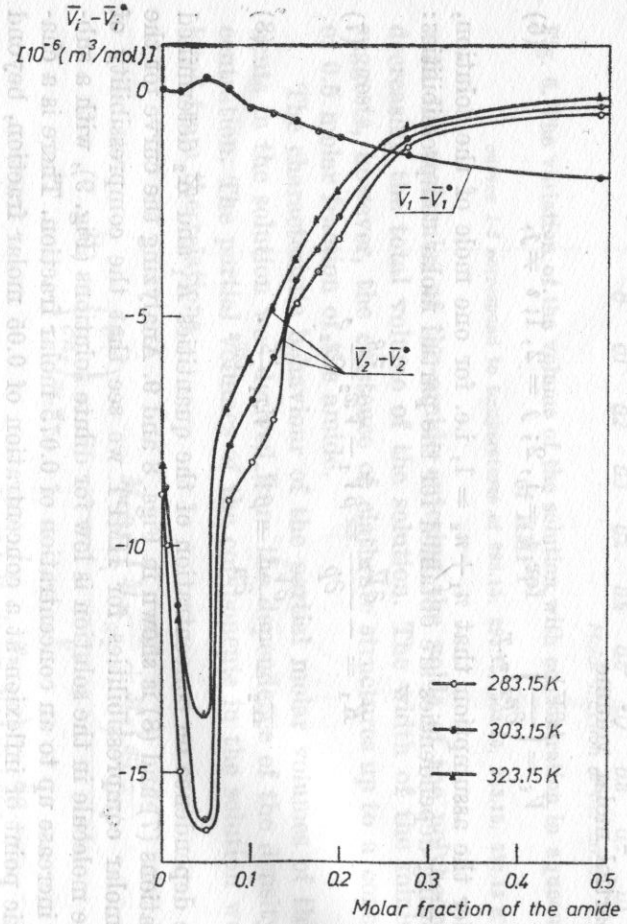

Fig. 7. The variation of the partial molar volumes $(\bar{V}_1 - \bar{V}_1^0)$ of the water and $(\bar{V}_2 - \bar{V}_2^0)$ of the amide as functions of concentration in aqueous solution of HMPT

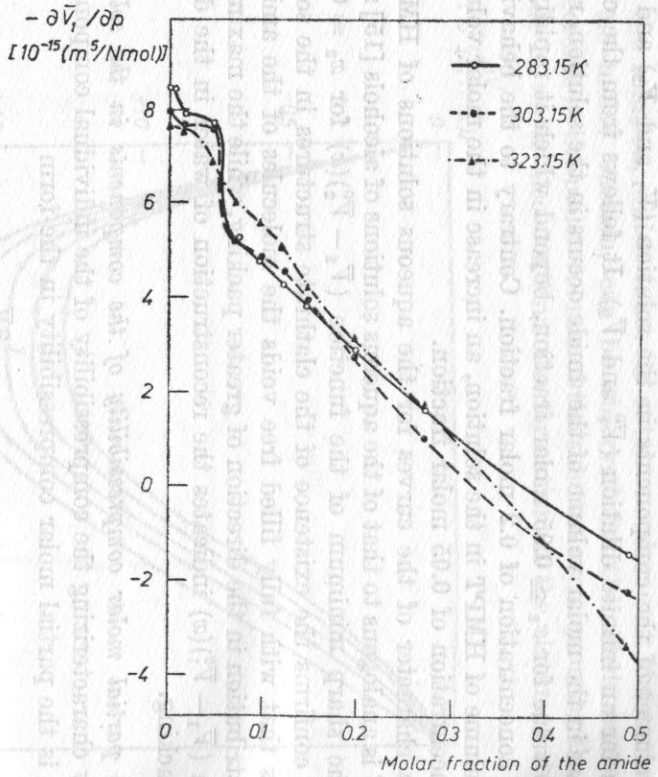

Fig. 8. The variation of the partial adiabatic compressibility of water with concentration in aqueous solutions of HMPT

compressibility of the amide in the solution, the partial molar compressibility of the water, K_1, decreases with increasing concentration of the amide (Fig. 8). Up to a concentration of 0.05 molar fraction, K_1 is almost independent of concentration, and subsequently decreases rapidly up to a concentration of 0.075

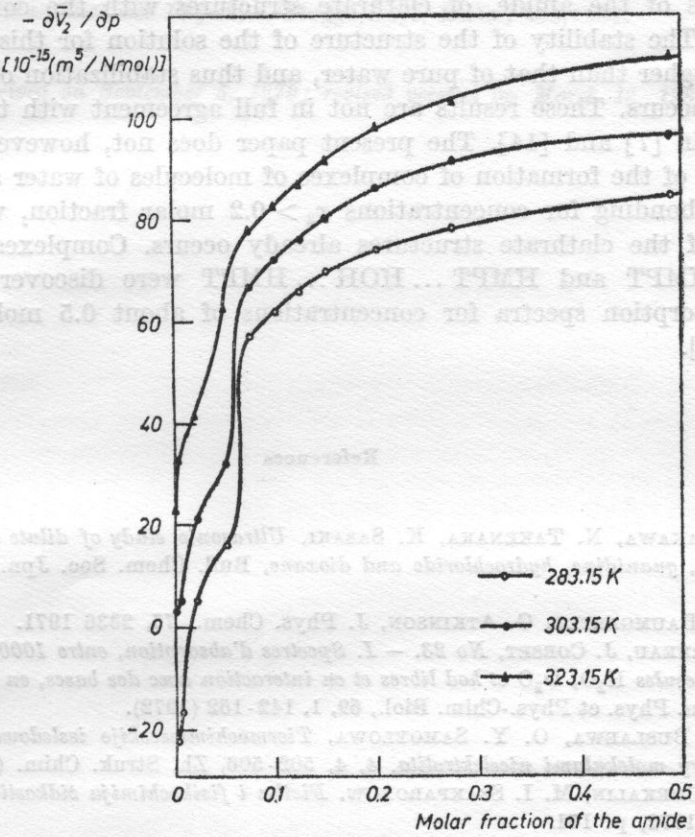

Fig. 9. The variation of the partial adiabatic compressibility of the amide with concentration in aqueous solutions of HMPT

molar fraction. The decrease in the compressibility of water for $x_2 \cong 0.02$ is caused by the lower compressibility of the clathrate structures, while the stability of K_1 over the range 0.02-0.05 molar fraction indicates that the molecules of HMPT enter the voids formed by the clathrate structure of water. The occurrence of additional amide molecules, which do not enter the voids of the clathrate compounds caused an increase in K_2 and a decrease in the compressibility of the water, K_1. The relationship of $K_1(x)$ and $K_2(x)$ indicates a strong intermolecular interaction between the components in the solution, particularly over the lower range of concentrations.

5. Final conclusions

Ultrasonic and volumetric investigations of the structure of aqueous solutions of hexamethylphosphortriamide indicate the occurrence, at low concentrations of the amide, of clathrate structures with the composition $8X \cdot 136H_2O$. The stability of the structure of the solution for this concentration is much higher than that of pure water, and thus stabilization of the structure of water occurs. These results are not in full agreement with the conclusions proposed in [7] and [14]. The present paper does not, however, exclude the possibility of the formation of complexes of molecules of water and HMPT by hydrogen bonding for concentrations $x_2 > 0.2$ molar fraction, where the destruction of the clathrate structures already occurs. Complexes of the types HOH ... HMPT and HMPT ... HOH ... HMPT were discovered in the infrared absorption spectra for concentrations of about 0.5 molar fraction of HMPT [3].

References

[1] K. Arakawa, N. Takenaka, K. Sasaki, *Ultrasonic study of dilute aqueous solutions of urea, guanidine, hydrochloride and dioxane*, Bull. Chem. Soc. Jpn., **43**, 3, 636-641 (1970).

[2] E. K. Baumgarter, G. Atkinson, J. Phys. Chem., **75**, 2336 1971.

[3] A. Burneau, J. Corset, *No 23. — I. Spectres d'absorption, entre 1000 et 11 000 cm^{-1}, des molecules H_2O, D_2O et hod libres et en interaction avec des bases, en solutions diluces*, J. Chem. Phys. et Phys.-Chim. Biol., **69**, 1, 142-152 (1972).

[4] M. N. Buslaewa, O. Y. Samoylowa, *Tiermochimiczeskije issledowanija stabilizacii struktury molekułami nieelektrolita*, **4**, 4, 502-506, Zh. Struk. Chim. (1963).

[5] N. V. Chekalin, M. I. Szakparonow, *Fizika i fizikochimija żidkostiej*, Wyp. 1, Izd. MGU, 1972, p. 151.

[6] H. Endo, D. Nomoto, *The ultrasonic velocity and the absorption of aqueous t-butyl alcohol solutions in relation to the structures of water and solutions*, Bull. Chem. Soc. Jpn., **46**, 3004-3007 (1973).

[7] V. S. Goncharov, P. S. Jastremskii et al., *Stabilizacia struktury wody molekułami gieksamietilfosfortriamida*, Zh. Fiz. Chim., **LI**, 4, 789-792 (1977).

[8] P. S. Jastremskii, *K woprosu o stabilizacii struktury wodnyh rostworow*, Ż. Struk. Chim., **4**, 2, 179-183 (1963).

[9] P. S. Jastremskii, O. Y. Samoylow, *Stabilizacia struktury wodnyh rastworow molekułami nieelektrolita i dielektriczeskaja pronitsajemost'*, Ż. Struk. Chim., **4**, 6, 844-849 (1963).

[10] V. I. Jaszkichew, O. Y. Samoyłow, *O wlijani molekuł nieelektrolita na strukturu wodnyh rastworow*, Ż. Struk. Chim., **3**, 2, 211 (1962).

[11] M. V. Kaulgud, K. J. Patil, *Ultrasonic velocity in aqueous solutions of amines*, Acustica, **28**, 2, 130-131 (1973).

[12] M. V. Kaulgud, K. J. Patil, *Volumetric and isentropic compressibility behaviour of aqueous amine solutions*, J. Phys. Chem., **80**, 2, 138-143 (1976).

[13] F. KAWAIZUMI, M. OHNO, Y. MIYAHARA, *Ultrasonic and volumetric investigation of aqueous solutions of amides*, Bull. Chem. Soc. Jpn., **50**, 9, 2229-2233 (1977).
[14] Y. M. KESSLER, et al., *Swojstwa i struktura smiesiej wody s giegsamietilfosfortriamidom*, Ż. Struk. Chim., **16**., 5, 797-807 (1975).
[15] K. NAKANISHI, *Partial molar volumes of butyl alcohols and of related compound in aqueous solutions*, Bull. Chem. Soc. Jpn., **33**, 6, 793-797 (1960).
[16] D. SETTE, *Handbuch der Physik*, s. Flugge/XI/1, Berlin, 355/1961.

Received on September 5, 1979; revised version on March 12, 1980

ARCHIVES OF ACOUSTICS
5, 4, 363-368 (1980)

THERMODYNAMIC PARAMETERS OF AN ULTRASOUND RELAXATION PROCESS IN 2-NITROBUTANOL-1

ADAM JUSZKIEWICZ, ZOFIA BARTYNOWSKA-MEUS

Institute of Chemistry, Jagiellonian University
(30-060 Kraków, ul. Karasia 3)

Measurements of the velocity and absorption coefficient of ultrasound were carried out in 2-nitrobutanol-1 with respect to the frequency of the sound and the temperature. The relaxation process can be accounted for in terms of a rotation about the C–C bond. The relaxation parameters for the observed process have been determined.

1. Introduction

Disubstituted butane derivatives are very interesting for ultrasonic investigations because within this group of compounds the existence of relaxation effects connected with a restricted rotation about the C–C bond can be expected. As a result of this restricted rotation process, molecules of different conformational forms are present in the environment.

Investigation of the absorption frequency spectrum and the ultrasound velocity enables us to observe such effects and to determine the kinetic and thermodynamic parameters of the ultrasonic relaxation process.

The aim of this work was the investigation of the relaxation effects in 2-nitrobutanol-1, a representative of the β-nitroalcohols which have not previously been examined with acoustic methods.

The investigated substance was also of interest because its two polar groups $-OH$ and $-NO_2$ can form an intermolecular hydrogen bond, which constitutes an additional factor stabilizing one of conformational forms.

In our previous paper [1] results of measurements of the ultrasonic velocity and absorption coefficients for 2-nitrobutanol-1 have been presented. However, the frequency range was too narrow to permit a full description of the examined phenomenon.

The present studies, carried out over widened frequency and temperature ranges allow us to determine all the characteristic parameters of the ultrasonic relaxation process connected with the rotation of the 2-nitrobutanol-1 molecule about the C–C bound.

The measurements were made over the temperature range −55 to +80°C with an high frequency apparatus US-4, which has been described previously [2], and with an ultrasound spectrometer CSU-250 over frequency range 2.5-57 MHz. The ultrasound velocity in the same temperature range was determined with a modified pulsephase interferometer UI-14, over the frequency range 2.5-15 MHz.

2. Experimental part

As the ultrasonic attenuation of the investigated substance is of the order of 10^{-13}, it was necessary to make the measurements using very thin liquid films, of the order 100 μm. In order to achieve adequate accuracy in measuring this distance we used a modified Abbe cathetometer, made by Carl Zeiss Jena, which measured the distance to an accuracy of ±0,5 μm.

Accurate measurement of the temperature in the experimental vessel was achieved by using a compensating method and a resistance thermometer. The resistance thermometer was made of platinum and gave an accuracy of ±0.01°C, it has a very stable characteristic curve over long periods of use. For the investigations, 2-nitrobutanol-1 produced by the firm Fluka AG of Switzerland was used. The initial experiments were carried out over the temperature range 0° to 80°C. They showed a slight decrease in the ultrasonic attenuation with increasing temperature [1]. The results of these measurements showed the necessity of extending the investigated temperature range below 0°C. Absorption coefficients were measured for the following frequencies: 2.5, 5, 7.5, 10.0, 12.5, 13.4, 15.1, 17.9, 21.1, 35.9, 44.2 and 57.3 MHz over the temperature range −55 to +10°C. The velocity of ultrasound was determined for frequencies of 2.5, 5, 7.5, 10, 12.5 and 15 MHz. Within the investigated frequency range, dispersion of the velocity was not observed.

3. Discussion

The analysis of the curves of α/f^2 versus $\log f$ (Fig. 1) leads us to conclude that in 2-nitrobutanol-1, in these ranges of frequency and temperature, we can observe relaxation processes associated with conformational rearrangements of this compound. It may be described by the equation [3]

$$\alpha/f^2 = \frac{A}{1+(f/f_c)^2} + B, \tag{1}$$

where A and B are constants, and f_c is the specific relaxation frequency.

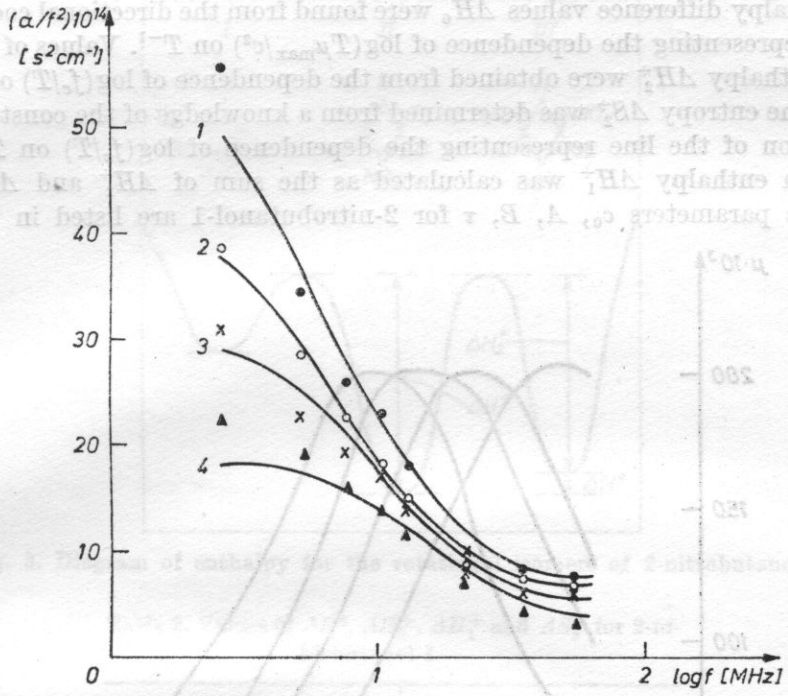

Fig. 1. The plot of α/f^2 vs. log$f$
1 – –50.0°C; *2* – –47.5°C; *3* – –45.0°C; *4* – –42.5°C

A coefficient of relaxation absorption per wave-length, μ, was calculated from equation

$$\mu = (\alpha/f^2 - B)c_0 f, \tag{2}$$

where c_0 is the velocity of sound at low frequencies and B is the limiting of α/f^2 for high frequencies (Table 1).

The values of μ are shown in Fig. 2. The relaxation terms (Table 1) were calculated from:

$$\tau = (2\pi f_c)^{-1}. \tag{3}$$

Table 1. Thermodynamic parameters A, B, τ and velocity c_0 for 2-nitrobutanol-1

T [°C]	A [10^{17} s^2·cm^{-1}]	B [10^{17} s^2·cm^{-1}]	c_0 [m/s]	$\tau \times 10^{-8}$ [s^{-1}]
–50.0	84 865	7000	1674	5.31
–47.5	35 057	6500	1668	2.27
–45.0	25 307	5000	1660	1.59
–42.5	15 448	3180	1652	0.96
–40.0	14 388	2500	1646	0.88
–37.5	12 256	1500	1638	0.76
–35.0	8570	500	1632	0.72

Enthalpy difference values ΔH_0 were found from the directional coefficients of lines representing the dependence of $\log(T\mu_{max}/c^2)$ on T^{-1}. Values of the activation enthalpy ΔH_2^+ were obtained from the dependence of $\log(f_c/T)$ on temperature. The entropy ΔS_2^+ was determined from a knowledge of the constant term in equation of the line representing the dependence of $\log(f_c/T)$ on T^{-1}. The activation enthalpy ΔH_1^+ was calculated as the sum of ΔH_2^+ and ΔH_0. The ultrasonic parameters c_0, A, B, τ for 2-nitrobutanol-1 are listed in Table 1.

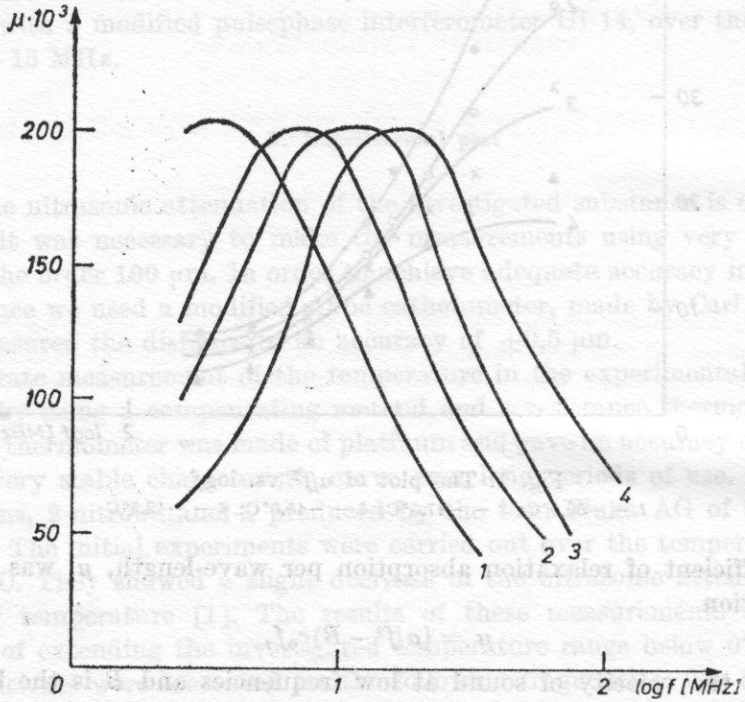

Fig. 2. The plot of μ vs. $\log f$
1 – −50°C; *2* – −47.5°C; *3* – −45.0°C; *4* – −42.5°C

The relaxation process which we observed in our sample is related to the rotation of the molecules around the C–C bond. Theoretically three different conformations are possible for 2-nitrobutanol-1 and are shown schematically in Fig. 3. Owing to the presence of NO_2, C_2H_5 and OH groups in the molecule of 2-nitrobutanol-1, the conformers have different energy levels. Of the three considered here the first seems to be the least stable (i.e. it has the highest energy level) because of the steric hindrance caused by the NO_2, C_2H_5 and OH groups. The second and third conformers have much lower energy levels, but the second will be probably the more preferred as the two polar groups, NO_2 and OH, may form hydrogen bonds [4, 5].

The values of activation enthalpy ΔH_2^+, ΔH_1^+, the enthalpy difference ΔH^0, and the entropy of activation ΔS_2^+ are collected in Table 2.

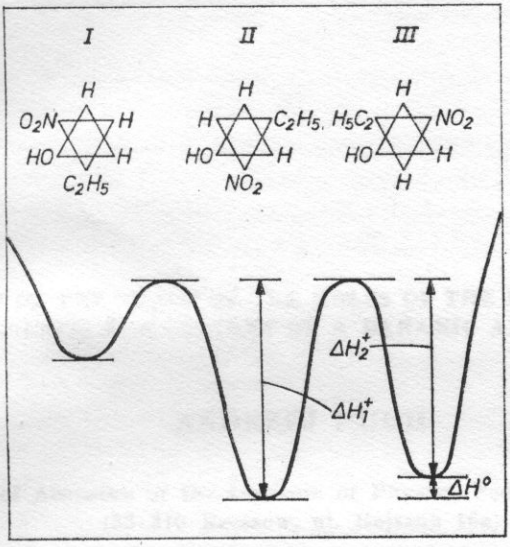

Fig. 3. Diagram of enthalpy for the rotational isomers of 2-nitrobutanol-1

Table 2. Values of ΔH^0, ΔH_2^+, ΔH_1^+ and ΔS_2^+ for 2-nitrobutanol-1

ΔH_0 [kcal/mol]	ΔH_2^+ [kcal/mol]	ΔH_1^+ [kcal/mol]	ΔS_2^+ [cal/mol]
1.05	15.22	16.27	−44.12

The high value of the activation enthalpy ΔH_2^+ indicates that the form II is present in a significant majority.

Mechnical energy introduced into our system by acoustic waves id absorbed in order to overcome the energy barrier involved in the transformation between the second and third conformers.

References

[1] B. Zapiór, A. Juszkiewicz, Z. Bartynowska, *Investigation of the relaxation processes in 2-nitrobutanol-1 using acoustic methods*, Zeszyty Naukowe UJ, Prace Chem., **21**, 191 (1976).

[2] A. Juszkiewicz, *A set of apparatus for measuring the coefficient of absorption of ultrasounds at frequencies of 10-60 MHz, over a temperature range −60 to +200°C*, Zeszyty Naukowe UJ, Prace Chem., **21**, 257 (1976).

[3] J. Lamb, *Physical Acoustics*, vol. II, part *A*, 1965, pp. 203.

[4] T. Urbański, *On aliphatic nitrocompounds XXVI hydrogen bonds in nitroalcols and infra-red absorption spectra*, Roczniki Chemii, **31**, 37 (1957).

[5] H. Całus, H. Jankowska, T. Urbański, *Hydrogen bonds and dipole moments of nitroalcs*, Chemistry and Industry, **10**, 41 (1959).

Received on December 1, 1979: revised version on May 19, 1980.

ARCHIVES OF ACOUSTICS
5, 4, 369-380 (1980)

THE EFFECT OF THE SHAPE OF THE HOLES OF THE ROTOR AND STATOR ON THE ACOUSTIC PARAMETERS OF A DYNAMIC AXIAL GENERATOR

ANDRZEJ PUCH

Department of Acoustics of the Institute of Physics, Pedagogical University
(35-310 Rzeszów, ul. Rejtana 16a)

The paper presents the results of investigations concerning choice of the optimal shape (from the viewpoint of acoustical efficiency) of the holes of the rotor and stator of a dynamic axial generator, the horn and pressure chamber of which are common to all the stator channels.

Compared to the sound power and the efficiency for a generator operating with the rotor preferred hitherto a doubling of the values of the parameters was achieved for a generator which has an approximate rectangular function for the time-dependence of the active surface area of the inlet holes of stator channels.

1. Introduction

ALLEN and WATTERS [2, 3], MILNE [6] and WYRZYKOWSKI [12] have dealt in their papers with the effect of the shape of the rotor and the stator on the acoustic parameters of an axial generator.

Allen and Watters have undertaken an attempt to develop a dynamic generator producing a sinusoidal wave. Hitherto the work by both of these authors has been purely experimental. The investigations involved the hole systems (arrangement) of the rotor and the stator of the axial generator.

Milne and Wyrzykowski have theoretically considered the effect of the shape of the holes of the rotor and stator on the acoustic parameters of a dynamic generator. The latter author provided a solution to this problem for a dynamic axial generator, the stator of which is formed by the inlet holes of the catenoidal horns, with the acoustic impedance of the pressure chamber being negligibly small compared to the impedance of the horn inlet. He has confined his considerations to the frequency range, in which the impedance of the horn

inlet can be regarded as independent of the frequency. The paper by Milne is concerned with a particular case of these considerations.

A different version of the design of a dynamic axial generator considered by Wyrzykowski was in practice [4]. However, it is the most feasible to use several horns, so that the optimal working range of these generators is confined to comparatively low frequencies.

At higher frequencies, of the order of kHz, dynamic axial generators of a different design were used [1]. They are provided with a separate stator with channels which at one end fit into a common horn with an annular cross-section, while at the other end they lead into a common pressure chamber. The pressure chamber of such a generator does not usually contain any sound-absorbing elements.

The paper is the second one dealing with a dynamic axial generator of the above-mentioned design.

In the first paper [9] a theoretical model of the generator was presented. The model showed agreement with experiment over the range of frequencies for which it is possible to propagate exclusively plane waves in the acoustic system of the generator, and for air pressure excess in the pressure chamber, small compared to the ambient pressure.

In this paper the results of investigations aimed at increasing the acoustic efficiency of the generator are presented. The stimulus for the work was the suggestion by JONES [4] and WYRZYKOWSKI [13] that dynamic generators producing a rectangular wave can have twice the acoustic efficiency of those producing a wave which has a sinusoidal variation in time.

2. Criteria for the choice of hole shape

The author has previously shown [9] that while operating a dynamic axial generator with a catenoidal horn common to all the stator channels, it is not possible to create a state in which the acoustic impedance of the inlet hole of the stator channel is real and independent of the frequency. For this reason it is not possible to apply the analysis of Wyrzykowski [12] to the above-mentioned design of a dynamic axial generator. The necessity has thus arisen of carrying out investigations aimed at the determination of the optimum shape of the holes of the rotor and stator of this design of a dynamic axial generator (Fig. 1) for maximizing the acoustical efficiency.

The following criteria for the choice of the shape of these holes have been adopted:

— the dependence of the active field of the inlet hole surface of the stator channel on the time, $S(t)$, should as closely as possible, approximate a rectangular function with a duty factor (being the ratio of the pulse duration of the function $S(t)$ to its period) equal to 0.5;

– the shape of the holes of the rotor and stator should be as simple as possible in design.

A necessary condition for meeting the first of these criteria is an acceptance of the equality of the times for which the inlet holes of the stator channels are fully opened and fully closed by the rotor. Initially it can be said that the time of opening (or closing) of the inlet holes of the stator channels by the rotor should be sufficiently small compared to the time the holes are fully open (or closed). The problem of the definition of an acceptable value for the ratio of these two times still remains. A reduction in the ratio leads to a reduction in the number of holes which can be arranged on the circumference of the stator channel thus increasing the mismatch of the impedance of the horn inlet to the wave impedance of the stator channel [9]. Finally, instead of increasing the sound power and efficiency of the generator we could have diminished the values of these quantities.

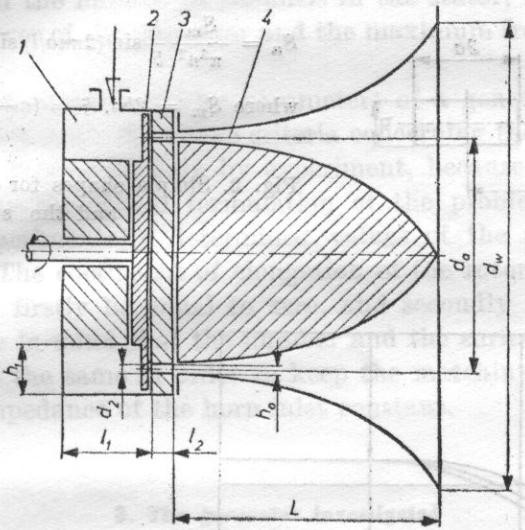

Fig. 1. Diagram of the acoustic system of a dynamic axial generator with horn and pressure chamber common to all the stator channels
1 – pressure chamber, *2* – rotor, *3* – stator, *4* – horn

Taking into consideration the second of the above criteria we can on the basis of paper [12] define, for the rotor and stator shapes shown in Fig. 2, the curve of variation of the ratio φ_1 (the amplitude of the first harmonic of the function $S(t)$ to the maximum values S_m of this function) with the coefficient of elongation, of these holes. The coefficient of elongation is defined as the ratio of the time the inlet hole of the stator channel is fully open (or closed), to the time of opening or closing of the hole by the revolving rotor of the generator.

The results obtained are presented in Fig. 3. From the figure one can conclude that if it is assumed that the times of the inlet holes of the stator channels being fully open and fully closed by the rotor are equal, for $\xi > 0.5$ the

Coefficients of expansion of the function $S(t)$ into a Fourier series:

a)

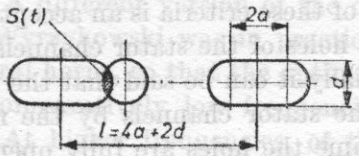

$$S_n = \frac{2S_m}{\pi^2 n^2}\frac{l}{d}\left[I_1(2\pi nd/l)\sin(2\pi na/l) + S_1(2\pi nd/l)\times\right.$$
$$\left.\times\cos(2\pi na/l)\right],$$

where $S_m = \pi d^2/4$, $\xi = 2a/d$

b)

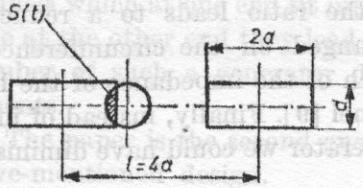

$$S_n = \frac{4S_m}{\pi^2 n^2}\frac{l}{d}I_1(\pi nd/l)\sin(2\pi na/l),$$

where $S_m \pi d^2/4$, $\xi = (2a-d)/d$; $I_1(z)$ and $S_1(z)$ are Bessel and Struve functions of the first order, respectively

c)

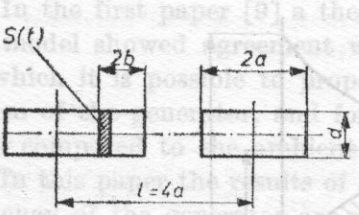

$$S_n = \frac{S_m}{\pi^2 n^2}\frac{l}{b}\sin(2\pi na/l)\sin(2\pi nb/l),$$

where $S_m = 2bd$, $\xi = (a-b)/b$, $n = 0,1,2,\ldots$

Fig. 2. Simple shapes for the holes of the rotor and the stator

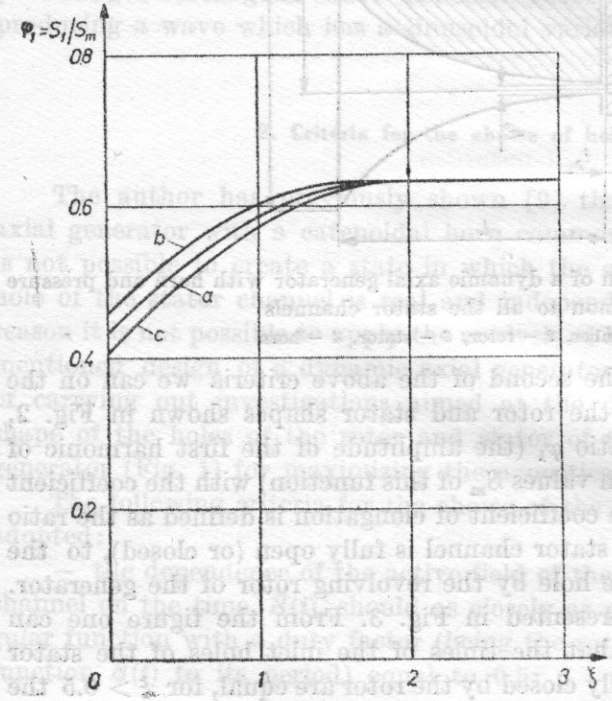

Fig. 3. The dependence of the ratio of the first harmonic of the function $S(t)$ to the maximum value S_m of this function, on the coefficient of elongation ξ for holes shaped as in Fig. 2

shape of these holes is not really essential. The value φ_1 is then constantly greater than 0.5. On the other hand if $\xi > 2$, the value of φ_1 is constant and equal to 0.63, being independent of both the shape of holes of the rotor and stator, and the value of the coefficient of elongation. From the above discussion two conclusions can be drawn:

– in approximating the time variations of the active area of the inlet hole of the stator channel by a rectangular function, the shape of the holes of the rotor and the stator is of little practical importance. Thus a shape should be chosen that is simple to realize in practice, e.g. the one shown in Fig. 2a,

– if possible, it is advisable to admit a value for the coefficient of elongation of these holes as near as possible to two.

The use of holes in the rotor and stator of the generator, for which the coefficient of elongation has a value greater than unity brings about a considerable decrease in the number of channels in the stator, and thus diminishes both the sound power of the generator and the maximum frequency of the wave it produces.

The evaluation of the acoustic parameters of a generator, the rotor and stator holes of which meet the above criteria concerning the shape of the holes, can at present be performed only by experiment, because of basic difficulties encountered in the theoretical formulation of the problem. This paper will thus compare experimentally determined values of the acoustic parameters of the generator. The coefficient of elongation of the rotor and stator holes in the generator will firstly be equal to zero, and secondly very close to unity. It should be borne in mind that the number and the surface area of the stator channel should be the same in order to keep the matching conditions of these channels to the impedance of the horn inlet constant.

3. The generator investigated

The investigations involved the dynamic axial generator [8-10] the design of which is shown schematically in Fig. 1. The generator has a catenoidal horn common to all the stator channels with an annular cross-section. The pressure chamber is also common to all these channels and does not contain any sound-absorbing elements. The generator stator has 50 channels of circular cross-section, which are arranged evenly on the circumference of a circle, 100 mm in diameter. The generator is equipped with replaceable rotors with holes shaped as shown in Fig. 4. Both rotors satisfy the requirement of having the holes of the stator channel open and shut for equal times. The coefficient of elongation, ξ for the first of the rotors (Fig. 4a), which approximates by rectangular function time variations of the active surface area of the inlet hole of the stator channel, is equal to unity, while for the second classical one (Fig. 4b) it is equal to zero.

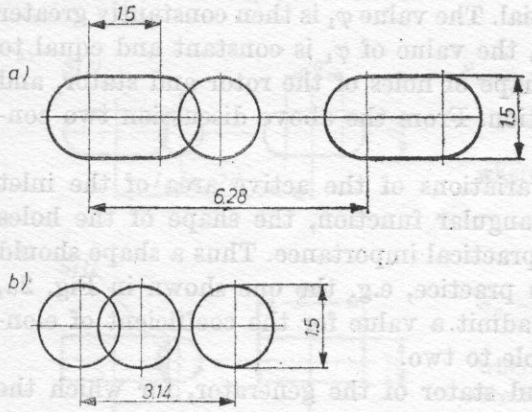

Fig. 4. The shapes and geometrical dimensions of the holes of the rotor and stator of the dynamic axial generator tested experimentally

4. Coefficient of acoustic efficiency

The preferred mostly used measure of acoustic efficiency of a dynamic generator is the ratio of the sound power radiated by the generator to the power required for the compression of the air mass taken by the generator from the ambient to the supply pressure [1-4, 8, 9, 11]. It is called the mechanical-acoustical coefficient of the generator efficiency (the acoustic efficiency), and expresses the effectiveness of the process of transforming the energy of compressed air into acoustic energy. Accordingly, for the determination of the acoustic efficiency one has to know the sound power radiated by the generator, and the power used to supply the generator with compressed air.

5. The method for determining the sound power

The direct determination of the total sound power N_a of the generator can be dispensed with on the basis of the experimentally defined distribution of the amplitude of the acoustic pressure in the far field at a constant distance from the horn outlet of the generator. Its value involves the sound power of the harmonic components of the wave radiated by the generator, and also the noise caused by turbulent air flow through some of the elements of the acoustic system of the generator. A selective method was used to single out from the complete signal produced by the generator the necessary components. On the basis of the measurements made it was found that the sound power of the higher harmonics produced by the generator is negligibly small compared to the sound power of the fundamental. For this reason in the following text of the paper the results of the measurement of the sound power of the generator are presented, since although they were obtained for the first harmonic, they can be regarded as representative of the total sound power contained in the discrete

components of the wave produced by the generator. The measurements of the acoustic power of the generator were made using the measuring method and apparatus as given in [9].

6. The method for determining the supply power

The power used to supply the generator with compressed air is equal to the power necessary for the compression of the air mass taken per time unit by the generator, from the ambient pressure P_0 to the supply pressure $P_1 = P_0 + P_G$. The determination of its value requires the calculation of the compression work of compressing a unit mass of air in a polytropic process of a particular type, and of the mass air flow to the generator [7]

$$N_s = L_t M_0. \tag{1}$$

The work performed in compressing a unit mass of air is defined as the amount of work done in a comparable compressor equal to the technical work in an isentropic compression

$$L_t = \frac{\varkappa}{\varkappa - 1} RT_1 \left[1 - \left(\frac{P_0}{P_1}\right)^{(\varkappa-1)/\varkappa}\right], \tag{2}$$

where P_1 and T_1 are correspondingly the pressure and temperature of the air in the pressure chamber of the generator, P_0 is the atmospheric pressure, R is the gas constant for air, and $\varkappa$ is the isentropic exponent. The air temperature in the pressure chamber of the generator is measured by means of a thermocouple and compensator (expansion pipe joint), and the excess pressure is measured by a manometer.

The value of the mass air flow M_0 supplying the generator was determined by means of a measuring pipeline equipped with a quadrant orifice plate [5]. The diagram of the compressed air installation supplying individual systems of the generator is shown in Fig. 5. Air is forced by an electrically driven two-stage piston compressor S (output 0.08 m³/s, at a delivery pressure of $8 \cdot 10^5$ N/m²) to an equalizing tank Z with a volume of 5 m³, whence, via the oil separator O, it is fed to

(I) the acoustic system of the generator via a pressure regulator R_G and a regulating valve Z_G which permit precise regulation of the pressure of the air in the pressure chamber and also via the measuring pipeline RP which permits determination of the value of the mass air flow supplying the generator,

(II) the microturbine via a pressure regulator R_T and a regulating valve Z_T which permit precise regulation of the angular velocity of the generator rotor, and thus also of the frequency of the wave produced,

(III) the air bearings via a stop valve Z_L.

The control of the supply parameters of the generator is performed by a set of manometers.

In the measurements performed, the maximum relative error, with which it was possible to determine the value of the supply power of the generator did not exceed 15 %.

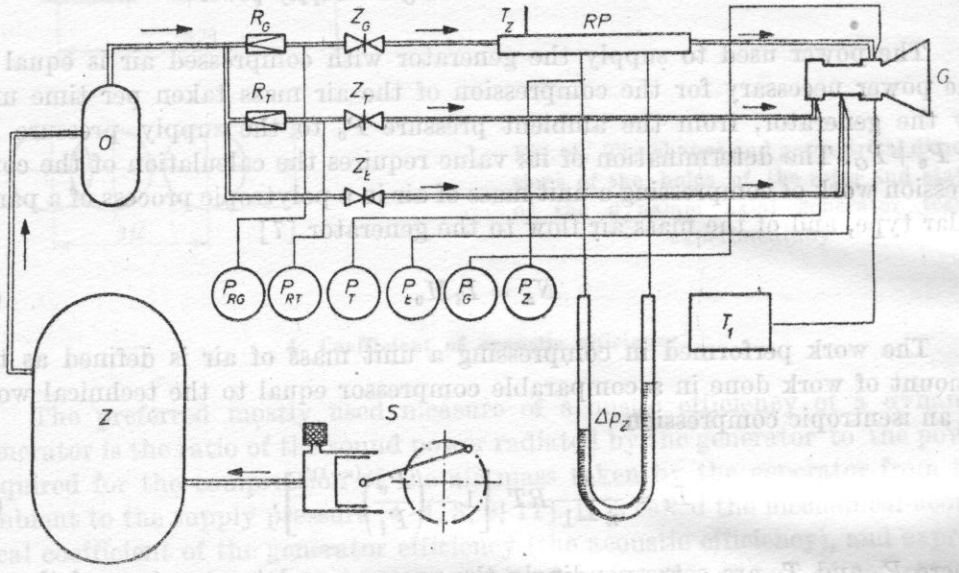

Fig. 5. Diagram of the compressed air unit supplying the generator

Thus, the maximum relative error, with which it was possible to determin the value of the acoustic efficiency of the generator did not exceed 43.1 %.

7. Discussion of the results of the measurements and conclusions

It follows from the dependence of the sound power on the frequency of the generator wave presented (in Fig. 6) that, irrespective of the type of rotor with which the generator is actually operating, the sound power decreases above 4000 Hz, and also below about 2000 Hz. From the analysis of a theoretical model of the generator [9] it can be concluded that the decrease of sound power below 2000 Hz is related to the limiting frequency of the horn while that occuring above a frequency of 4000 Hz is caused by the resonance properties of the pressure chamber of the generator. The maximum sound power occurs at those frequencies for which the impedance of the horn inlet is matched to the wave impedance of the stator channel.

It follows from Fig. 7a that with increasing pressure in the pressure chamber of the generator, there occurs an increase in the sound power produced. At higher pressures an increasingly larger fraction of the energy of the compressed

air is transformed into the sound power of the noise induced by turbulence in the acoustic system of the generator, which evidently must be realized at the expense of sound power in the harmonic components. This causes a decrease in the sound power of the generator for high values of the air pressure in its pressure chamber.

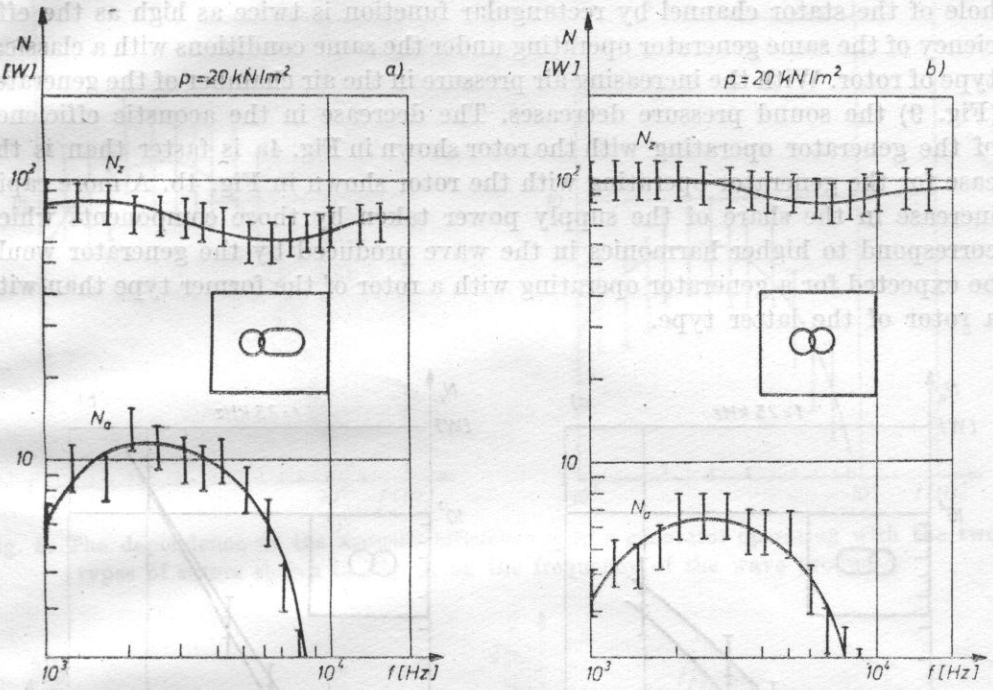

Fig. 6. The dependence of the sound power N_a and the supply power N_z of a generator operating with the two types of rotors shown in Fig. 4, on frequency of the wave produced

It follows from the dependence of the sound power of the generator on the frequency of the wave produced (Fig. 6), and of the excess pressure of the air in the pressure chamber (Fig. 7a) that the sound power of a generator operating with its rotor behaviour approximating the time variations of the active surface area of the inlet hole of the stator channel by a rectangular function (Fig. 4a), is twice as high as the power of a similar generator operating under the same conditions with a classical type of rotor (Fig. 4b).

The supply power of the generator (Fig. 6) shows a local minimum at a frequency of about 8000 Hz. It follows from an analysis of a theoretical model of the generator [9] that such minima occur at the resonance frequencies of the stator channel. The minimum observed in the experiment is for the first of these. With an increase in the air pressure in the pressure chamber of the generator (Fig. 7b), the supply power increased very rapidly. From the dependence of the supply power of the generator on the frequency of the wave produced (Fig. 6), and on the pressure of the air in its pressure chamber (Fig. 7b), it fol-

lows that the value of the supply power of a generator operating under given conditions is practically independent of the type of rotor.

From the considerations presented hitherto, and also from Fig. 8 it can be concluded that the acoustic efficiency of a generator operating with a rotor behaviour approximating time variations of the active surface area of the inlet hole of the stator channel by rectangular function is twice as high as the efficiency of the same generator operating under the same conditions with a classical type of rotor. With the increasing air pressure in the air chamber of the generator (Fig. 9) the sound pressure decreases. The decrease in the acoustic efficiency of the generator operating with the rotor shown in Fig. 4a is faster than is the case for the generator operating with the rotor shown in Fig. 4b. A more rapid increase in the share of the supply power taken by those components which correspond to higher harmonics in the wave produced by the generator would be expected for a generator operating with a rotor of the former type than with a rotor of the latter type.

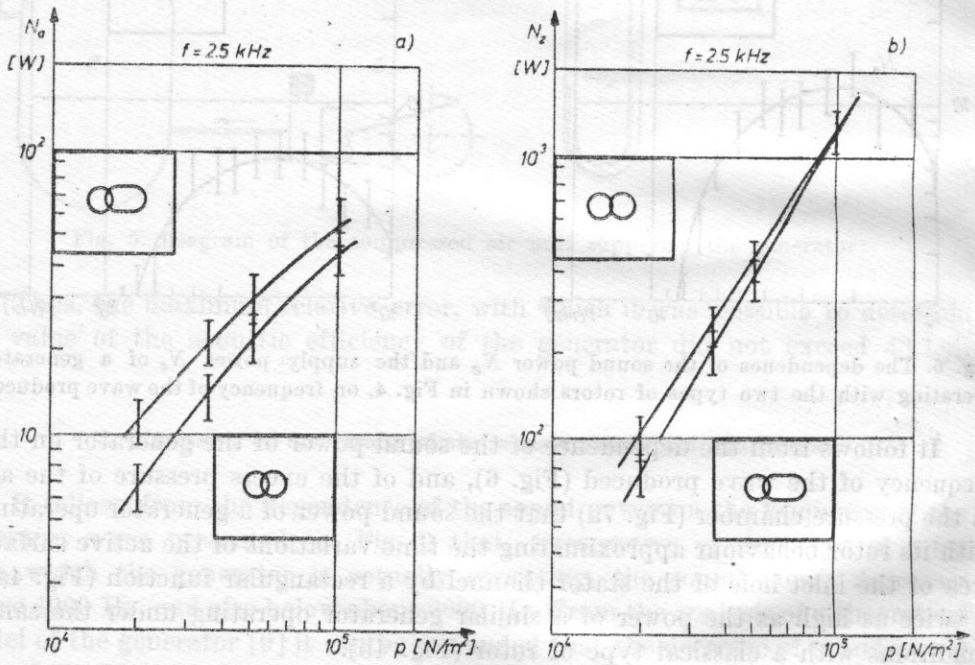

Fig. 7. The dependence of the sound power N_a of a generator operating with the two types of rotors shown in Fig. 4, on the excess air pressure P in its pressure chamber

The maximum value of the acoustic efficiency of a generator with an excess air pressure in its pressure chamber of $0.2 \cdot 10^5$ N/m², and operating with a rotor giving approximately a rectangular function of time variations of the active surface area of the inlet hole the stator channel was (18 ± 8) %. The sound power produced was (12 ± 3) W. Increasing the excess air pressure

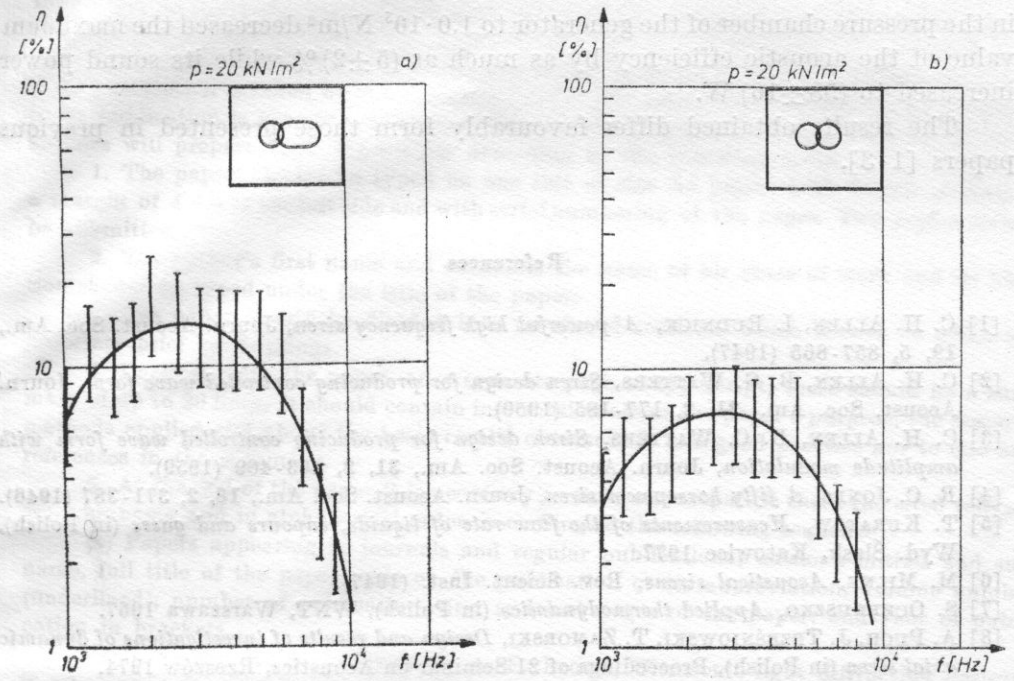

Fig. 8. The dependence of the acoustic efficiency η of a generator operating with the two types of rotors shown in Fig. 4, on the frequency of the wave produced

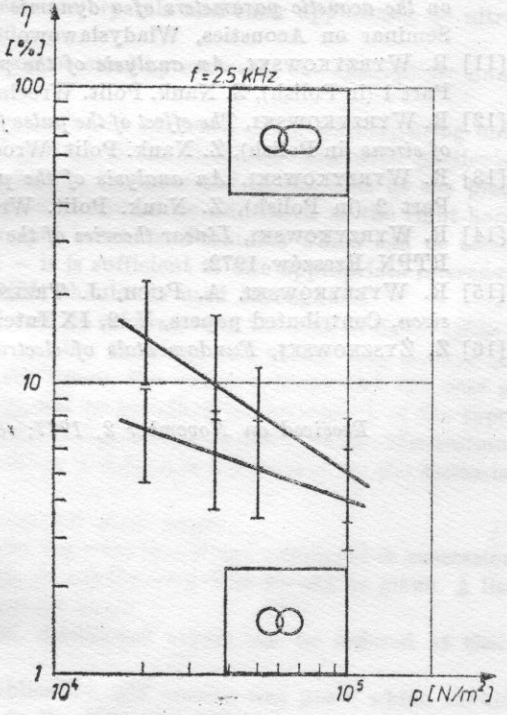

Fig. 9. The dependence of the acoustic efficiency η of a generator operating with the two types of rotors shown in Fig. 4, on the excess air pressure P in its pressure chamber

in the pressure chamber of the generator to $1.0 \cdot 10^5$ N/m^2 decreased the maximum value of the acoustic efficiency by as much as (5 ± 2)% while its sound power increased to (58 ± 16) W.

The results obtained differ favourably form those presented in previous papers [1-3].

References

[1] C. H. ALLEN, I. RUDNICK, *A powerful high frequency siren*, Journ. Acoust. Soc. Am., **19**, 5, 857-865 (1947).

[2] C. H. ALLEN, B. G. WATTERS, *Siren design for producing controlled wave form*, Journ. Acoust. Soc. Am., **31**, 2, 177-185 (1959).

[3] C. H. ALLEN, B. C. WATTERS, *Siren design for producing controlled wave form with amplitude modulation*, Journ. Acoust. Soc. Am., **31**, 2, 463-469 (1959).

[4] R. C. JONES, *A fifty horsepower siren*, Journ. Acoust. Soc. Am., **18**, 2, 371-387 (1946).

[5] T. KURATOW, *Measurements of the flow rate of liquids, vapours and gases* (in Polish), Wyd. Śląsk, Katowice 1977.

[6] M. MILNE, *Acoustical sirens*, Rev. Scient. Inst. (1947).

[7] S. OCHĘDUSZKO, *Applied thermodynamics* (in Polish), WNT, Warszawa 1967.

[8] A. PUCH, J. TRZEŚNIOWSKI, T. ZAMORSKI, *Design and results of investigations of dynamic axial siren* (in Polish), Proceedings of 21 Seminar on Acoustics, Rzeszów 1974.

[9] A. PUCH, *Generalized model of an axial dynamic generator*, Archives of Acoustics, **13**, 1, 17-34 (1978).

[10] A. PUCH, R. WYRZYKOWSKI, *The effect of the shape of the holes of the rotor and stator on the acoustic parameters of a dynamic generator* (in Polish), Proceedings of 24 Open Seminar on Acoustics, Władysławowo 1977.

[11] R. WYRZYKOWSKI, *An analysis of the possibility of increasing the efficiency of sirens*, Part 1 (in Polish), Z. Nauk. Polit. Wrocławskiej, Fizyka, III, **48**, 71-93 (1961).

[12] R. WYRZYKOWSKI, *The effect of the pulse form on the wave form and the working conditions of sirens* (in Polish), Z. Nauk. Polit. Wrocławskiej, Fizyka, V, **75**, 5-60 (1964).

[13] R. WYRZYKOWSKI, *An analysis of the possibility of increasing the efficiency of sirens*, Part 2 (in Polish), Z. Nauk. Polit. Wrocławskiej, Fizyka, VIII, **107**, 51-63 (1965).

[14] R. WYRZYKOWSKI, *Linear theories of the acoustic field of gas medium* (in Polish), WSP-RTPN Rzeszów 1972.

[15] R. WYRZYKOWSKI, A. PUCH, J. TRZEŚNIOWSKI, T. ZAMORSKI, *High-duty acoustical siren*, Contributed papers, V. 2, IX International Congress on Acoustics, Madrid 1977.

[16] Z. ŻYSZKOWSKI, *Fundamentals of electroacoustics* (in Polish), WNT, Warszawa 1953.

Received on November 2, 1977; revised version on June 13, 1980